LUND UNIVERSITY

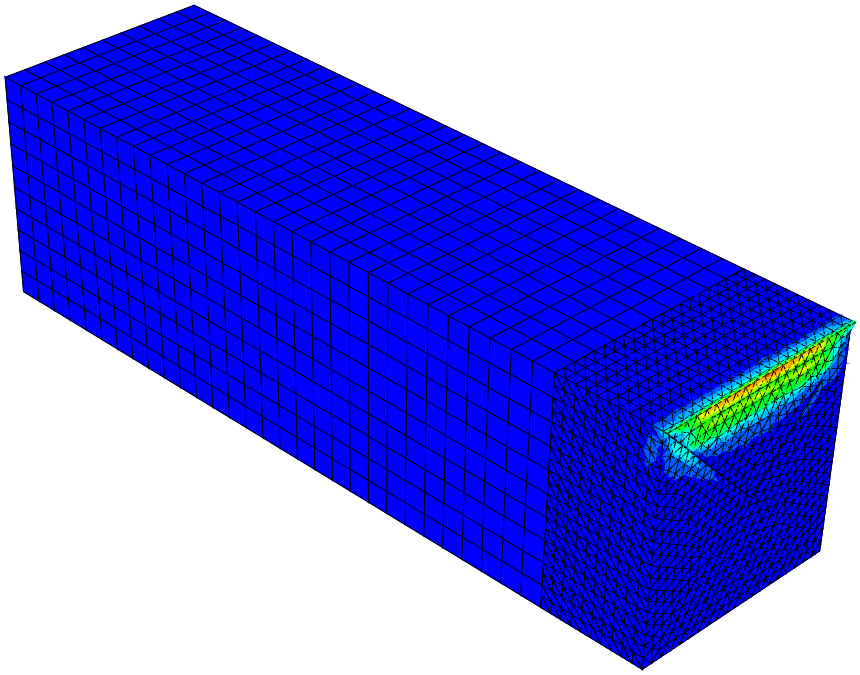

FRACTURE CHARACTERISTICS OF ACETYLATED BIRCH

Experimental and numerical studies

GARY LAI & SAMUEL PLÖNNING

Structural Mechanics

Master's Dissertation

DEPARTMENT OF CONSTRUCTION SCIENCES

DIVISION OF STRUCTURAL MECHANICS

ISRN LUTVDG/TVSM--19/5234--SE (1-86) | ISSN 0281-6679

MASTER'S DISSERTATION

FRACTURE CHARACTERISTICS OF ACETYLATED BIRCH

Experimental and numerical studies

GARY LAI & SAMUEL PLÖNNING

Supervisor: Dr **HENRIK DANIELSSON**, Division of Structural Mechanics, LTH.
Assistant Supervisor: **KARIN FORSMAN**, MSc, Division of Structural Mechanics, LTH.
Examiner: Professor **ERIK SERRANO**, Division of Structural Mechanics, LTH.

Printed by V-husets tryckeri LTH, Lund, Sweden, July 2019 *(Pl)*.

For information, address:
Division of Structural Mechanics,
Faculty of Engineering LTH, Lund University, Box 118, SE-221 00 Lund, Sweden.
Homepage: www.byggmek.lth.se

Abstract

Modification of wood is carried out to increase the durability and dimensional stability of wood, and one of the modification methods is acetylation. Acetylation of wood means that polymers in the cell wall react with acetic anhydride. Today, acetylated wood is rarely used in load-bearing structures and there are only a few studies on how the fracture characteristics are affected by acetylation. A study found in the literature indicates a 15-20 % reduction of the fracture energy in acetylated spruce compared to untreated spruce. Due to the small number of studies made, it is important to increase the knowledge of how acetylation affects fracture characteristics in order to determine whether acetylation is a useful modification method for structural applications. In this dissertation, an investigation is made on how birch is affected by acetylation, both through a numerical and an experimental study.

A literature study is presented which includes a description of the micro and macro structures of wood, the acetylation process, basic fracture mechanics and a background of the finite element method. The experimental work, based on a Nordtest method, is performed to determine the fracture energy of the specimens. Values of the fracture energy are then used to calibrate the FE-models. 40 specimens were tested, half of which were untreated and half acetylated. The specimens had either rectangular or triangular shaped cross-section areas exposed to tension perpendicular to the grain, in order to investigate whether the geometry of the tested cross-section affected the outcome of stable or unstable response.

The acetylated birch showed a 12 % higher mean value of the density than the untreated birch. The mean moisture content was 3 % in the acetylated wood and 11 % in the untreated. From the experimental work, a 55 % reduction of the mean value of fracture energy was obtained for the acetylated birch compared to the untreated birch. When comparing the results from the numerical models with the experimental results, both models predicted a value of the maximum load that was 15 % lower than what was obtained in the tests. The value of the fracture energy was 4.5 % less for the model of the acetylated birch and 3.7 % less for untreated birch. The triangular cross-section generated more stable responses compared to the rectangular.

Sammanfattning

Modifiering av trä genomförs för att öka träets beständighet och formstabilitet. En modifieringsmetod är acetylering, som innebär att cellväggarna reagerar med ättiksyra. Idag används sällan acetylerat trä i lastbärande strukturer och det finns få studier om hur de brottmekaniska egenskaperna påverkas av acetylering. En tidigare studie indikerar en 15-20 % minskning av brottenergin för acetylerad gran jämfört med obehandlad gran. Då få studier har gjorts, är det viktigt att öka kunskapen om acetyleringens påverkan på de brottmekaniska egenskaperna för att kunna avgöra huruvida acetylering är en användbar modifieringsprocess. I det här examensarbetet görs således en undersökning om hur björk påverkas av acetylering, både genom en numerisk och en laborativ studie.

En litteraturstudie görs som behandlar träets struktur, acetyleringsprocessen, grundläggande brottmekanik samt en bakgrund inom finita elementmetoden. Den laborativa studien som genomfördes baseras på en Nordtest-metod, där värden på brottenergin från studien användes för att kalibrera finita element modeller. Totalt testades 40 provkroppar, varav hälften obehandlade och hälften acetylerade. Provkropparna hade antingen rektangulära eller triangulära brottanvisningar, för att undersöka om brottanvisningens geometri påverkar stabiliteten under provningen.

De acetylerade provkropparnas densitet hade ett 12 % högre medelvärde än de obehandlade provkropparna. Medelvärdet på fuktkvoten var 3 % för acetylerat trä och 11 % för obehandlat. Från de laborativa resultaten påvisades en 55 % minskning av medelvärdet på brottenergi för den acetylerade björken jämfört med den obehandlade. När resultaten från de numeriska modellerna jämförs med de laborativa resultaten så var den maximala lasten 15 % mindre för båda modellerna. Brottenergin underskattades med 4.5 % för modellen av den acetylerade björken och med 3.7 % för den obehandlade. Den triangulära geometrin på brottanvisningens gav flera stabila responser jämfört med den rektangulära.

Preface

This dissertation comprises 30 credits and has been completed at the Division of Structural Mechanics at Lund University. The dissertation has been written by Samuel Plönning and Gary Lai and concludes our Civil Engineering degree at Lund University. We would like to thank our supervisors Karin Forsman and Henrik Danielsson for all their valuable inputs, support and guidance throughout the process.

Samuel Plönning & Gary Lai
12th June 2019, Lund

Notations and Symbols

u	Moisture content
$w_{initial}$	Weight of water before oven-dry state
w_{dry}	Weight of water after oven-drying
R	Radial direction
T	Tangential direction
L	Longitudinal direction
E	Young's modulus (modulus of elasticity)
G	Shear modulus
$\boldsymbol{D}$	Constitutive matrix
$\boldsymbol{C}$	Material compliance matrix
U_e	Elastic strain energy
U_P	Potential energy from the loads
A	Crack area
G_c	Critical energy release rate
G_f	Fracture energy
A_{dim}	Cross sectional area
F	Force
$\boldsymbol{b}$	Body force vector
$\boldsymbol{t}$	Traction stress vector
$\boldsymbol{n}$	Unit normal vector
$\boldsymbol{B}$	Displacement differentiation matrix
$\boldsymbol{v}$	Arbitrary weight vector

$\boldsymbol{u}$	Displacement vector
$\boldsymbol{N}$	Element shape functions
$\boldsymbol{a}$	Nodal point displacements
S	Total boundary
$\boldsymbol{K}$	Stiffness matrix
$\boldsymbol{f_b}$	Boundary load vector
$\boldsymbol{f_l}$	Body force vector
$\boldsymbol{f_0}$	Initial strain vector
D	Scalar damage variable
T^o_{eff}	Effective traction at initiatioin of damage
b_c	Critical width
h_c	Critical height
m_{eq}	Mass in equilibrium
m_{tot}	Total mass of test setup
m_{prism}	Mass of prism
W	Work
A_c	Critical area
u_0	End deflection
$\boldsymbol{\delta}$	Deformation vector
$\boldsymbol{\varepsilon}$	Strain vector
ν	Poisson's ratio
ρ	Density
$\boldsymbol{\sigma}$	Stress vector
Π	Potential energy

∂	Partial derivative
$\tilde{\nabla}$	Matrix differential operator
$\int_S$	Integration over surface
$\int_V$	Integration over volume
$\tilde{\square}$	Quantity in local coordinate system
$\square^T$	Transpose

Contents

1 Introduction

This chapter describes the framework, in which the dissertation stays. A background is presented which includes a description of wood in general and birch more specific. A general description of modified wood is then presented, followed by how the modification affects mechanical properties and fracture characteristics. The aims and objectives are then stated which will be linked to the conclusion at the end of the dissertation. Further, the method and the limitations used are presented.

1.1 Background

Wood is historically a building material that has had great impact on the human life, and since the beginning of humanity, people have surrounded themselves with structures made out of wood. The advantages with wood are not only that it is renewable but also that it is easy to transport and process. Further advantages are its low dead weight, good insulation characteristics and its high strength compared to its weight. The disadvantages include its low resistance against mold, rot and moisture.[13]

During the last hundred years the forest asset in Sweden has more than doubled, since the harvesting each year is smaller than the annual growth of the forest. As seen in Figure 1.1, the harvesting in 2014 was 90 million cubic meters compared to the growth of over 120 million cubic meters. As a result, the wood stock is continuously increasing by each year and in 2014 the wood stock storage was 3 billion cubic meters.[24]

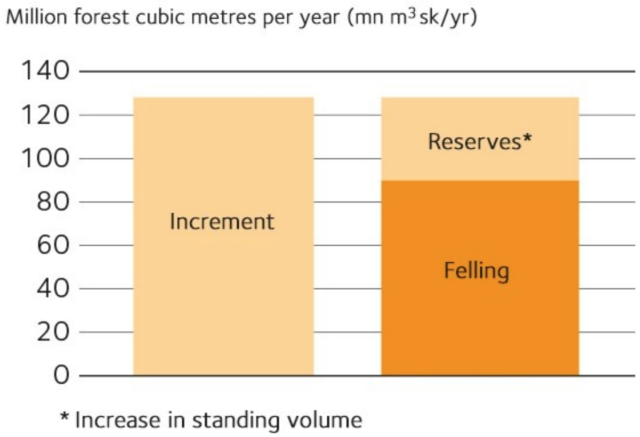

Figure 1.1: Comparison of tree growth and tree felling in Sweden 2014.[29]

The forest in Sweden corresponds to approximately one percent of the total forest area in the world. The standing volume from this amount is divided into 42 % spruce, 39 % pine, 12 % birch and the remaining 7 % are different kinds of deciduous species.[24]

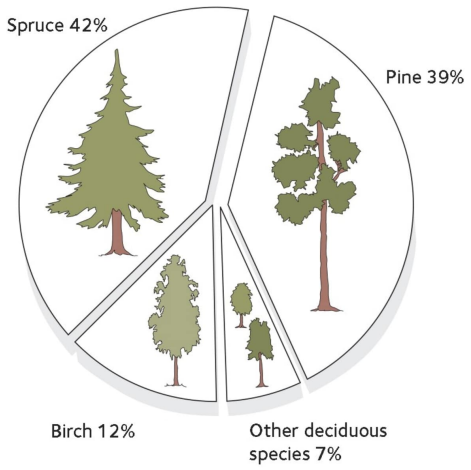

Figure 1.2: Swedish standing volume of tree species in percent.[24]

Even though birch only stands for 12 % of the standing volume, it is the tree species in Sweden that has the widest field of application. Historically, it has been used to create furniture, handicraft tools, cookware, instruments and more. Today, applications such as wood flooring, wood panels and wood splines are more common. However, birch has not been used for structural purposes due to its low durability and poor dimensional stability in varying climate. Therefore its main area of use has been in indoor environments.[34]

The most common species of birch in Sweden are the silver birch and the downy birch. They have similar but not identical characteristics. Downy birch has fibers that are more straight compared to silver birch and is therefore easier to process, while silver birch is more attractive for furniture purposes [34]. However, both commonly and in this dissertation, the various species are assumed to have the same characteristics and mechanical properties. They will further on be referred to as *birch*.

One way to improve the durability of wood in moist conditions is by chemical modification, which changes the chemical composition of the cell wall polymers. Different kinds of modification methods have been tested over the years without achieving any major commercial significance. Acetylation was one of those methods, but lately, commercial acetylated products such as Accoya wood have been developed. Acetylation changes the structure of wood by swelling of the wood, filling the cell walls with acetic anhydride. This makes the wood less susceptible to water and hence showing less swelling and shrinkage, making the material more dimensionally stable.[25]

Acetylated wood is not commonly used in structural applications and studies regarding the effects of acetylation on mechanical properties of wood for different tree species, show different results. Hill [6] compiles several different reports, and for the modulus of rupture (MOR) and for the modulus of elasticity (MOE), the results show a decrease by 6 % for both MOR and MOE for pine but an increase by 7 % for spruce. Regarding fracture characteristics of acetylated wood, only a few studies have been conducted. One of the studies was made by Reiterer and Sinn [1], showing a 15-20 % decrease of the fracture energy for acetylated spruce compared to untreated spruce.

This dissertation investigates how the acetylation affects the fracture characteristics of birch. The fracture energy, i.e. the amount of energy consumed in producing one unit of traction-free crack, is calculated. By comparing the fracture energy of untreated and acetylated birch, the impact of acetylation can be estimated. The fracture energy of a material is an important parameter to analyze as regards brittleness, when designing for example timber joints. It is also a decisive parameter for tension perpendicular to grain for end-notched beams.[32]

1.2 Aim and Objective

The aim of this dissertation is to increase the knowledge regarding fracture characteristics of birch and to investigate how these are affected by acetylation.

The objectives for this dissertation are the following:

- Determine and compare the fracture energy between acetylated and untreated birch.
- Determine and compare material properties such as density and moisture content between acetylated and untreated birch.
- Create and calibrate finite element models using experimental results.
- Compare and discuss the results from different notch geometries of the test specimens, using both the experimental work and numerical analyses.

1.3 Method

A literature study was performed focusing on material properties of wood. The main aim was to gain insight in the necessary background of wood, e.g. micro and macro structures of wood, moisture content and dimensional stability. Material properties of wood also includes how the acetylation process modifies wood and the material characteristics of birch compared to other tree species, such as spruce and pine. The literature study also involves a description of fracture mechanics, first by introducing linear elastics fracture mechanics and then nonlinear fracture mechanics. Finally, the concept of fracture energy is explained.

Experimental tests were performed using a modified version of the Nordtest method, which was developed to determine the fracture energy of wood. The Nordtest method involves three point bending of a simply supported beam, with a notch made at the bottom of the beam. The notch is made to create a propagation of an existing crack. The modification of the Nordtest method is due to several reasons, one reason is the limited size of the planks available, which made it impossible to use the sizes prescribed in the standard. To achieve stable load-displacement responses two types of notch geometries were tested, a rectangular and a triangular shape.

A numerical analysis was made using the finite element (FE) program Abaqus. A background of the finite element method used in Abaqus is presented, where the different element types used to mesh the test setup are described. In the FE-analyses,

half of the test setup was modeled in order to reduce the computational costs. In the plane of symmetry, the nonlinear fracture behavior was modelled by introducing cohesive interaction properties.

1.4 Limitations

The following limitations apply for this dissertation:

- The experimental work was not conducted in a controlled climate, i.e. the relative humidity and temperature differed from one test to another.
- The specimens are assumed to consist of clear wood, i.e. no defects in the wood are considered.
- The material behavior is assumed to be linear elastic outside the fracture process zone.

2 Material properties of wood

This chapter presents an introduction to the material properties of wood. First, a short introduction about wood anatomy, from macro to micro structure, is presented. Following that, wood-water relations are discussed and how changes in moisture content will affect the dimensional stability and durability of wood. An overview of different wood modification methods is then given, with emphasis on acetylation. The orthotropic structure of wood is then explained and described in terms of its constitutive relation. Finally, birch characteristics are introduced and compared to characteristics of pine and spruce, the two most commonly used species for load-bearing applications.

2.1 Wood anatomy

2.1.1 Macro structure and micro structure

As illustrated in Figure 2.1, a free standing tree in the forest can be seen as a cantilever beam, with the dead weight of the tree working with gravity towards the ground while resisting horizontal wind loads. For millions of years the tree has been improving and optimizing its structure and characteristics against this load case. Wood is an organic material affected by natural forces during its lifetime causing defects in the wood such as knots, splits, burls, coarse grain and fungal damage. Wood free from these defects is referred to as *clear wood*.[8][5]

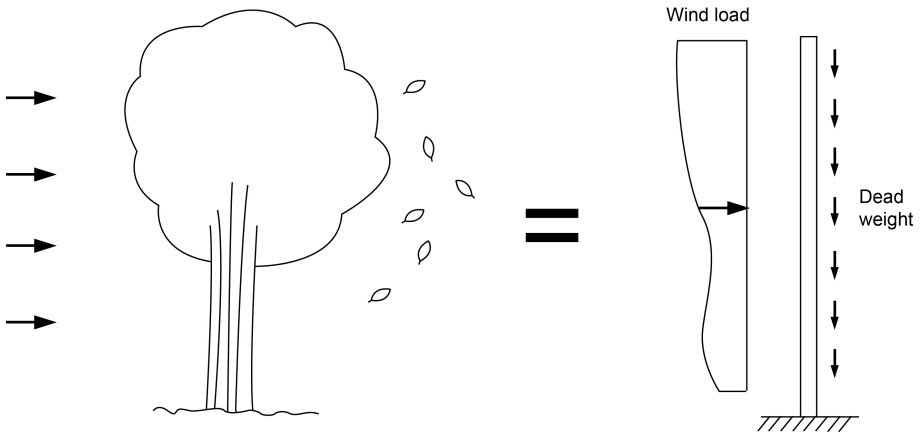

Figure 2.1: Tree seen as a cantilever exposed to wind load and dead weight, modified after [13].

The pith is located in the center of the tree trunk and is surrounded by the heartwood and the sapwood. Outside of the sapwood is the cambium, which produces cells inwardly while bark cells are producing cells outwardly. The cambium is encased by the bast and finally the outer bark. The macro structure is illustrated to the left in Figure 2.2. Trees only grow during a limited period of the year, and the cell walls grow differently during these time periods, thus the wood is divided into earlywood and latewood. The earlywood and the latewood together denote a growth ring for one year. The growth rings are built up by wood cells which have the structure shown to the right in Figure 2.2. The wood cell consists of the middle lamella (ML), the primary

wall (P), the outer layer (S1), middle layer (S2), inner layer (S3) of the secondary wall and the warty layer (W). The middle lamella is a cohesive layer between the wood cells, holding them together. Inside the warty layer is the lumen, the cavity of the cell.[28][23]

Wood consists of cellulose, hemicellulose and lignin, where the cellulose is built up by coupled glucose molecules. Hemicellulose is a shorter version of cellulose and is build up by different kinds of sugar molecules. Lignin is holding the wood cells together and could be described as wood glue. Lignin also adds rigidity to the cell and has a good resistance against mold.[28][23]

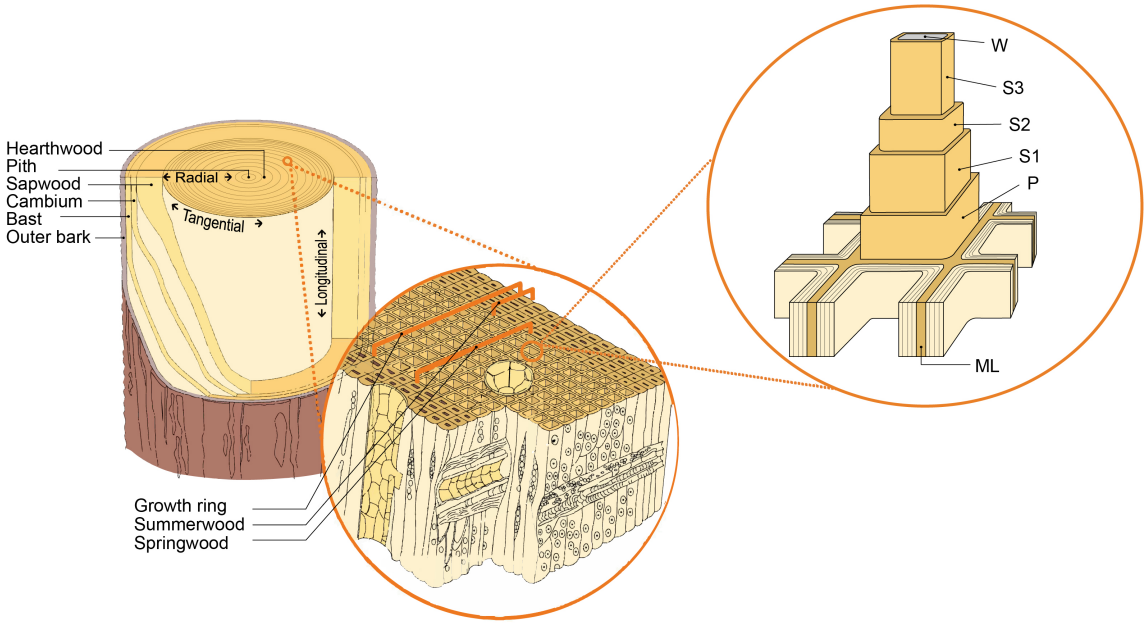

Figure 2.2: Composition of the tree trunk and the structure of a wood cell. The wood cell consists of the middle lamella (ML), the primary wall (P), the outer (S1), middle (S2), and inner (S3) layers of the secondary wall, and the warty layer (W). Modified after [28] and [23].

2.1.2 Softwood and hardwood

Coniferous trees, commonly known as softwoods, such as pine and spruce, represent a majority of the produced wood in Sweden. In the northern part of Sweden the pine trees are dominating due to the favorable dry conditions in the ground. In the southern part on the other hand, where the soil is more moist and fertile, the spruce dominates. Pine is mainly used for furniture, flooring, poles, plywood and timber whereas spruce is the dominating tree species within structural timber. Deciduous trees, commonly known as hardwoods, such as birch, aspen and alder are found throughout all of Sweden. Birch is a hard and tough material but has a low resistance against mold and rot. Its main area of use is furniture, floors, paper, plywood, fibre board, particle board and crafts.[24][21]

2.2 Wood physics

2.2.1 Moisture content

Wood physics, or the science of physical-mechanical properties of wood and wood-based materials, focusing to a large extent on wood density and how wood behaves when exposed to moisture. The moisture content determines how other properties of wood such as stiffness and strength, thermal conductivity and sensitivity to fungi are affected, particularly when moisture content exceeds 20 %.[5]

Wood is a capillary-porous material with a hygroscopic cavity system that is capable of absorbing both airborne moisture and liquid water using a capillary transport process. Bound water is a term used to express the proportion of water in the wood up to the *fibre saturation point*, which is the point when all free hydroxyl groups are occupied and is the point before any presence of free water in the cell cavities. *Free water* is the water that remains in the macro system up to the *water saturation point*, the stage at which no more water can be absorbed.[5]

The moisture content, u, is defined as the weight of the water in the wood divided by the weight of the wood in an oven-dry state. It is often expressed in percent. [26]

$$u = \frac{w_{initial} - w_{dry}}{w_{dry}} \cdot 100 \tag{2.1}$$

When freshly cut timber is dried, the water initially lost is the free water, with no molecular bounding to the wood. The bound water that remains in the cell walls on the other hand has molecular bonds and this is the reason why the energy required to drive out water from cell walls is much greater compared to eliminating free water. The fibre saturation point is between 25-35 %, where 28 % is chosen as a reasonable mean value for most practical applications. A significant change in most physical and mechanical properties can be shown for varying moisture content up to the fibre saturation point. Furthermore, most of the properties are virtually constant above the fibre saturation point.[5]

2.2.2 Dimensional stability and durability

The water molecules stored make the cell walls expand, a process known as swelling, while volume contraction, the process when moisture is released, is termed shrinking. Since expansion and contraction of cell walls relates to water molecules are accumulated or released, swelling and shrinking is limited to the hygroscopic area. When the fibre saturation point is reached, there will be no further swelling nor shrinking since only free water can be absorbed or discharged. As mentioned before, it is crucial to ensure an appropriate moisture content of wood to avoid unwanted swelling and shrinking deformation. The risk for rot and fungal problems also increases with increased moisture content [5][34]. The shrinkage varies depending on which direction referred to. A compilation of average values of the shrinkage in percent for different tree species and different directions is presented in Figure 2.1.

Table 2.1: Average values for shrinkage in various wood types, from the fibre saturation to absolutely dry wood.[27]

Wood type	Shrinkage			
	Fibre direction, along length of stem, axial βa (%)	Radial direction, across the growth rings βr (%)	Tangential direction, along the growth rings, βt (%)	Volume change βv (%)
Ash	0,2	5	8	13,2
Birch	0,3	6,7	10,4	17,4
Beech	0,3	5,8	11,8	17,9
Oak	0,4	4	7,8	12,2
Alder	0,5	4,4	9,3	14,2
Aspen	0,2	3,8	8,7	12,7
Spruce	0,3	3,6	7,8	11,7
Pine	0,4	4	7,7	12,1

For practical calculations, 7 percent can be used as the average figure for movement in sawn pine and spruce timber, which corresponds to 0.24 percent per 1 percentage point change in the moisture content.

2.3 Wood modification

2.3.1 Purpose

Wood in moist environments is often treated or modified, to increase its otherwise low durability. Due to environmental concerns, there is an increased interest of finding solutions to improve the properties of wood in an environmental friendly way. Modified wood should not present more harm to the environment than untreated wood when disposed at the end of its life cycle. The aim with wood modification is to improve dimensional stability and increase resistance against biological attacks, such as mold and rot. Although wood modification has been studied for over 50 years, it has not been applied commercially until recently.[6]

2.3.2 Thermal and chemical modification

Today, there are various wood modification methods, where the most common ones are thermal modification and chemical modification. Thermal modification came to focus in the beginning of the 21th century when it was realized that the moisture content in wood was decreased using a heating process. The process changes the properties of wood, making it more hydrophobic. An improved dimensional stability compared to untreated wood was seen, but also that wood dried at a higher temperature changed color. Darker tree species became lighter and lighter tree species became darker.[11]

Chemical modification of wood is when a chemical reagent reacts with the components of the cell wall polymers, such as cellulose and lingin. Acetylation and furfurylation are the most used methods commercially, and in this dissertation the modification process referred to as acetylation will be the main focus. The effect of the modification depends on the temperature, time of treatment and dimensions of the specimen [7]. Modification of wood results in a change of performance of the modified wood, which is the basis of chemical modification of wood.

2.3.3 Acetylation

Free hydroxyls are located in the wood cell wall, absorbing and releasing water molecules depending on the climate to which the wood is exposed. By acetylation, acetic anhydride reacts with the free hydroxyls in the cell wall of the wood, forming acetyl groups bonded to hydroxyl. Acetylation is a single-addition chemical reaction where acetic anhydride is used as the chemical reagent. One acetyl group is added to one hydroxyl group in the cell wall with no polymerization, which means that all the weight from the acetyl can be converted into units of hydroxyl groups.[6]

$$\underset{\text{acetic anhydride}}{\text{WOOD-OH} + (CH_3CO)_2O} \rightarrow \underset{\text{acetylated wood}}{\text{WOOD-O-COCH}_3} + \underset{\text{acetic acid}}{CH_3COOH}$$

As a result, the modified product will have a reduced ability to absorb water molecules, making it less susceptible to swelling and shrinkage, and therefore more dimensionally stable. The reason is that the cell walls are already filled with acetyl groups, causing the wood to be in a swollen condition, leaving less space for external water molecules to bind to.[6]

The practical process of making acetylated wood is by drying the wood in an oven until a low moisture content is reached, normally with a temperature between 100°C and 120°C [11]. The dried wood is then directly moved to the reactor to soak up the liquid acetic anhydride as visualized in Figure 2.3. This setup is used by Accsys Technologies in Arnhem, Netherlands when making the product Accoya wood. The acetic anhydride that is unused will be directed back to the acetic anhydride tank to be re-used. A vaporized system to soak the wood can be used instead of the liquid acetic anhydride. After soaking the wood with acetic anhydride, the wood is once again heated to dry.[11]

Acetylated wood has shown to have improved biological and physical properties. Regarding the biological properties it reaches the highest durability class when acetylated, with increased resistance against white- and brown rot fungi. The highest durability

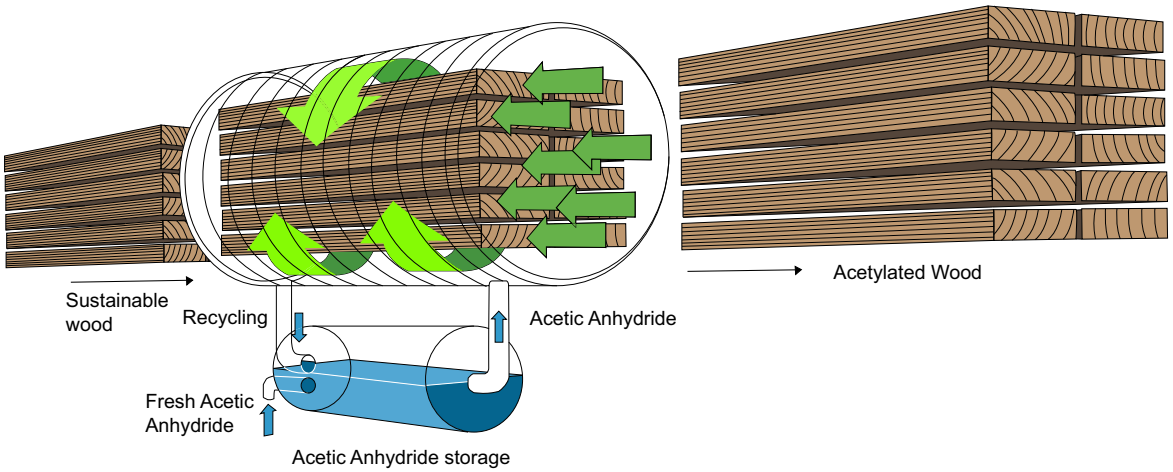

Figure 2.3: The acetylation process used by Accsys Technologies in Arnhem, Netherlands. Modified after [2].

class, class 1, in the European Standard is described as "very durable". With approximately 20 % acetyl content the acetylated wood has a fiber saturation point below 15 %. This results in shrinking and swelling deformations being reduced by 70-75 % compared to untreated wood. This because the wood becomes more hydrophobic when the acetyl groups have filled the cell walls. Acetylated wood has shown an increase in hardness between 15-30 % [11]. Studies of mechanical properties for acetylated wood, have shown different results for different tree species, where some suggest an increase and some a decrease, but still consistent results within each species. The increase and decrease shown has not been significant.[6]

2.4 Mechanical properties of wood

2.4.1 Orthotropic

With the structure of the tree described in subsection 2.1.1, it is easy to understand that the characteristics differ in different directions. This is termed anisotropy and it is important to understand in which direction the wood is being loaded and which characteristics that are used. The three principal axes are illustrated in Figure 2.4, these are called the longitudinal direction (L), tangential direction (T) and radial direction (R), and describes the coordinate system of wood [3]. As shown in the figure, the longitudinal direction is parallel to the fibre direction, the radial direction is starting in the center of the stem crossing the annual rings towards the edge of the stem and the tangential is perpendicular to the radial direction. Since wood has three orthogonal planes of symmetry with different properties, it is considered an orthotropic material. Characteristics often specified for materials are Young's modulus also known as the modulus of elasticity (E), the shear modulus (G) and Poisson's ratio (ν).[10]

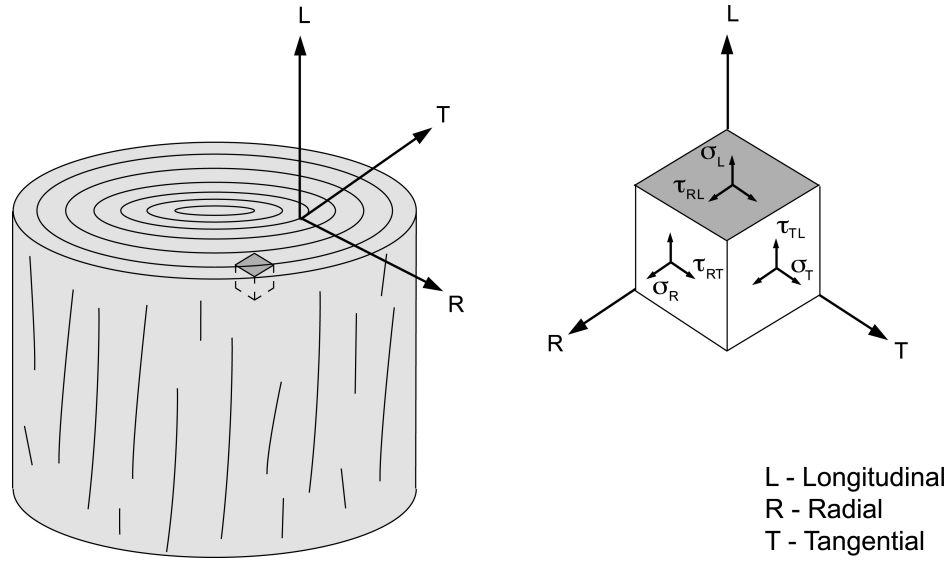

Figure 2.4: Definition of normal- and shear stresses in principal directions of wood. Modified after [30].

In Table 2.2, different material properties are compared for different wood species. As shown, the highest modulus of elasticity is in the longitudinal direction and lowest in the tangential.

Table 2.2: A compilation of wood properties.[10]

Species	Density (kg/m^3)	Moisture content (%)	E_L	E_R	E_T	ν_{TR}	ν_{LR}	ν_{RT}	ν_{LT}	ν_{RL}	ν_{TL}	G_{LT}	G_{LR}	G_{TR}
Hardwoods														
Balsa	200	9	6 300	300	106	0.66	0.018	0.24	0.009	0.23	0.49	203	312	33
Khaya	440	11	10 200	1130	510	0.60	0.033	0.26	0.032	0.30	0.64	600	900	210
Walnut	590	11	11 200	1190	630	0.72	0.052	0.37	0.036	0.49	0.63	700	960	230
Birch	620	9	16 300	1110	620	0.78	0.034	0.38	0.018	0.49	0.43	910	1180	190
Ash	670	9	15 800	1510	800	0.71	0.051	0.36	0.030	0.46	0.51	890	1340	270
Beech	750	11	13 700	2240	1140	0.75	0.073	0.36	0.044	0.45	0.51	1060	1610	460
Softwoods														
Norway spruce	390	12	10 700	710	430	0.51	0.030	0.31	0.025	0.38	0.51	620	500	23
Sitka spruce	390	12	11 600	900	500	0.43	0.029	0.25	0.020	0.37	0.47	720	750	39
Scots pine	550	10	16 300	1100	570	0.68	0.038	0.31	0.015	0.42	0.51	680	1160	66
Douglas fir[a]	590	9	16 400	1300	900	0.63	0.028	0.40	0.024	0.43	0.37	910	1180	79

[a] Listed in the original as Oregon pine.
E is the modulus of elasticity in a direction indicated by the subscript (N/mm^2).
G is the modulus of rigidity in a plane indicated by the subscript (N/mm^2).
ν_{ij} is the Poisson's ratio for an extensional stress in the j direction, given by

$$\nu_{ij} = \frac{\text{compressive strain in the } i \text{ direction}}{\text{extensional strain in the } j \text{ direction}}$$

2.4.2 Constitutive properties

For a linear elastic orthotropic material with principal directions L, T, R and small strains assumed, the constitutive relation between stress and strain can be expressed by Hooke's generalized law in the local coordinate system as:

$$\bar{\boldsymbol{\sigma}} = \bar{\boldsymbol{D}}\bar{\boldsymbol{\varepsilon}} \tag{2.2}$$

Where $\bar{\boldsymbol{\sigma}}$ is the stress vector, $\bar{\boldsymbol{\varepsilon}}$ is the strain vector and $\bar{\boldsymbol{D}}$ is the material stiffness matrix. They are specified in the material directions L, T and R as:

$$\bar{\boldsymbol{\sigma}} = \begin{bmatrix} \sigma_{LL} & \sigma_{RR} & \sigma_{TT} & \tau_{LR} & \tau_{LT} & \tau_{RT} \end{bmatrix}^T \tag{2.3}$$

$$\bar{\boldsymbol{\varepsilon}} = \begin{bmatrix} \varepsilon_{LL} & \varepsilon_{RR} & \varepsilon_{TT} & \gamma_{LR} & \gamma_{LT} & \gamma_{RT} \end{bmatrix}^T \tag{2.4}$$

$$\bar{\boldsymbol{D}} = \bar{\boldsymbol{C}}^{\boldsymbol{-1}} \tag{2.5}$$

$$\bar{\boldsymbol{C}} = \begin{bmatrix} \frac{1}{E_L} & \frac{-\nu_{RL}}{E_R} & \frac{-\nu_{TL}}{E_T} & 0 & 0 & 0 \\ \frac{-\nu_{LR}}{E_L} & \frac{1}{E_R} & \frac{-\nu_{TR}}{E_T} & 0 & 0 & 0 \\ \frac{-\nu_{LT}}{E_L} & \frac{-\nu_{RT}}{E_R} & \frac{1}{E_T} & 0 & 0 & 0 \\ 0 & 0 & 0 & \frac{1}{G_{LR}} & 0 & 0 \\ 0 & 0 & 0 & 0 & \frac{1}{G_{LT}} & 0 \\ 0 & 0 & 0 & 0 & 0 & \frac{1}{G_{RT}} \end{bmatrix} \tag{2.6}$$

where $\bar{\boldsymbol{C}}$ is the material compliance matrix. For the material stiffness matrix, there are three moduli of elasticity, E_L, E_R, and E_T, three shear moduli, G_{RT}, G_{LT} and G_{LR} and six Poisson's ratios, ν_{LR}, ν_{LT}, ν_{RL}, ν_{RT}, ν_{TL} and ν_{TR}. The indices correspond to the three material directions, L, R and T. The first index of Poisson's ratio is the loading direction while the second index is the strain direction. For an orthotropic material, the material stiffness matrix will be symmetric with nine independent coefficients. The following relation can be expected[3]:

$$\frac{\nu_{LR}}{E_L} = \frac{\nu_{RL}}{E_R}, \quad \frac{\nu_{LT}}{E_L} = \frac{\nu_{TL}}{E_T}, \quad \frac{\nu_{RT}}{E_R} = \frac{\nu_{TR}}{E_T} \tag{2.7}$$

These expressions are valid for an orthotropic material in its local coordinate system. Hooke's law may also be expressed in the global coordinate system with the global directions xyz:

$$\boldsymbol{\sigma} = \boldsymbol{D}\boldsymbol{\varepsilon} \tag{2.8}$$

$$\boldsymbol{\sigma} = \begin{bmatrix} \sigma_{xx} & \sigma_{yy} & \sigma_{zz} & \tau_{xy} & \tau_{xz} & \tau_{yz} \end{bmatrix}^T \tag{2.9}$$

$$\boldsymbol{\varepsilon} = \begin{bmatrix} \varepsilon_{xx} & \varepsilon_{yy} & \varepsilon_{zz} & \gamma_{xy} & \gamma_{xz} & \gamma_{yz} \end{bmatrix}^T \tag{2.10}$$

Where $\boldsymbol{\sigma}$ is the stress vector, $\boldsymbol{\varepsilon}$ is the strain vector and $\boldsymbol{D}$ is the material stiffness matrix in the global directions.[17]

2.4.3 Moisture content impact on mechanical properties

Various mechanical properties are affected when the level of moisture content varies. For example, the compressive strength is more sensitive to humidity than the tensile strength in direction along the grain, due to that the bonding of the cell walls are more moisture sensitive when subjected to compression force than for tension force.[5]

Table 2.3 shows a compilation of changes in the properties of clear wood with a one percent change in moisture content in wood, relative the properties at a moisture content of 12 %. The compilation shows the impact that wood moisture has on mechanical properties of wood.

Table 2.3: A compilation of changes in properties of clear wood with a one percent change in wood moisture.[5]

Property	Change
Compressive strength parallel to the grain	6%
Compressive strength perpendicular to the grain	5%
Bending strength	4%
Tensile strength parallel to the grain	2.5%
Tensile strength perpendicular to the grain	2%
Shear	2.5%
Modulus of elasticity (MOE) parallel to the grain	1.5%

Since the moisture content of wood varies depending on the climate and since the volume also changes accordingly when below the fibre saturation point, the density also depends on the level of moisture. The density is almost always specified for a specific climate often an ambient temperature of 20°C, 65 % humidity and a 12 % wood moisture. Density is one of the main variables that influences all wood characteristics, where most mechanical properties correlate positively to density. In Figure 2.5, a schematic illustration of the influence of density is shown.[5]

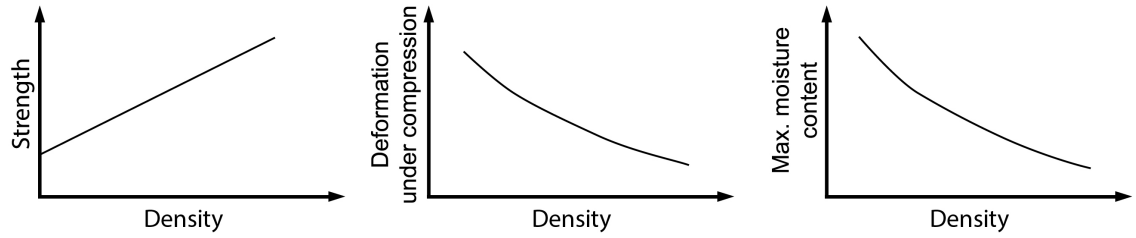

Figure 2.5: Schematic illustration of the influence of density.[5]

2.4.4 Properties of birch in relation to spruce and pine

Figure 2.6 presented by Ödlund [34] shows a compilation of calculated mean values of properties for birch, spruce and pine. The mean values for birch are set to 100 as a

reference value, and the values for both spruce and pine are related to that value. As seen in the comparison, birch matches and even surpasses spruce and pine in many properties, with moisture related properties being the only exception.[34]

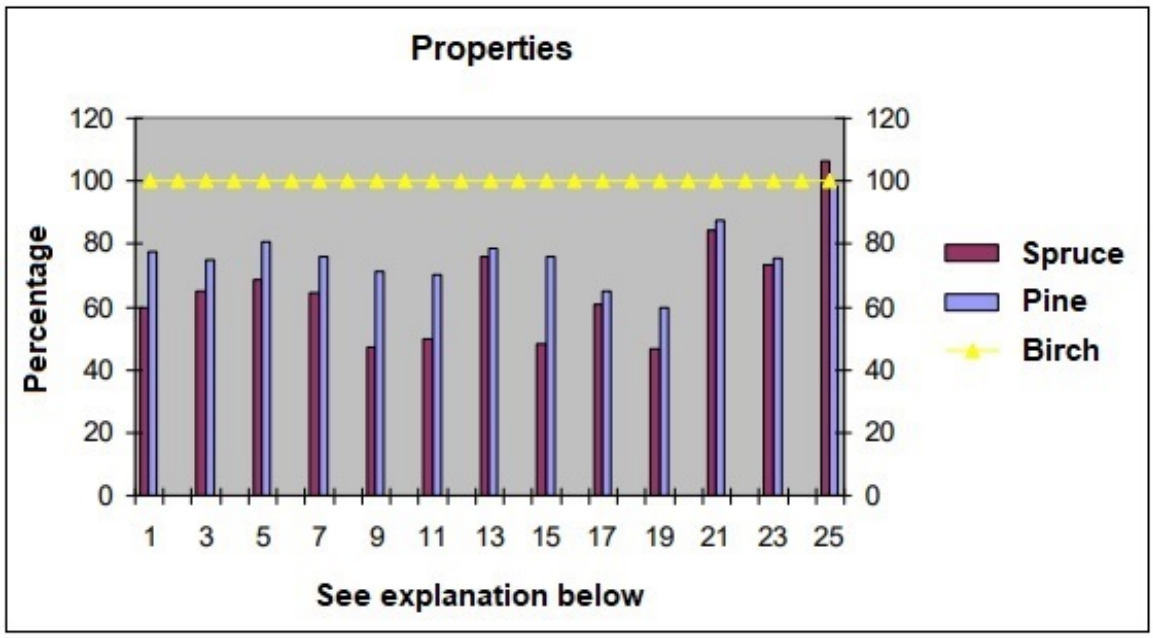

Figure 2.6: A comparison between different properties for birch, spruce and pine. Modified after [34].

The permeability, in this context the ability to absorb water, in the longitudinal direction is often higher for hardwood compared to softwood which is why the use of hardwood should be avoided in high moisture environments. Permeability for timber from birch can be around 1000 times higher than for spruce. Further, the risk of bacterial and fungi attacks in wood rises if the moisture content is beyond 20 % and the relative humidity varies [5]. Wood is a hygroscopic and orthotropic material. Therefore, it is of importance to take the sensitivity for moisture content for birch into consideration to avoid unwanted deformations.[34]

3 Fracture mechanics

Fracture mechanics is commonly divided into linear elastic fracture mechanics and nonlinear fracture mechanics. This chapter starts with a description of linear elastic fracture mechanics followed by nonlinear fracture mechanics. Both theories are a necessity to understand the fracture mechanics which the laboratory work is based on. The concept of fracture energy and the test setup used to determine it, is also introduced.

3.1 Linear elastic fracture mechanics

Linear elastic fracture mechanics (LEFM) is the theory and analysis of cracks and crack propagation within a material. The theory assumes an ideally elastic material and the existence of a sharp crack or a notch in the material. Due to the material behavior assumed within LEFM, the stress at the tip of the crack theoretically approaches infinity. This assumption is not reasonable but gives equations that are manageable and results that in many cases are reasonable accurate. The assumptions would result in fracture of the test specimen as soon as a small load is applied, which in the practical application is not the case. The theory of LEFM is based on the assumption that the existence of a sharp crack or notch gives rise to an inverse square root stress singularity. Due to the singularity, the conventional stress analysis with a stress based failure criterion is not applicable. Instead, energy-based criteria are typically used. Figure 3.1 visualizes a test specimen with a sharp crack where the stress distribution, σ, is shown in relation to the distance from the crack, r. LEFM is applicable as long as the fracture process zone (FPZ), the zone where the material is not behaving linear and where the cracking is occurring, is small compared to the length of the crack. LEFM assumes an elastic stress distribution in the material hence the non-linearities in the FPZ are disregarded. Furthermore, an ideally brittle material behavior and an infinite material strength is assumed. LEFM cannot be used to analyze crack initiation but can be used to analyze if an existing crack will propagate or not.[12][9]

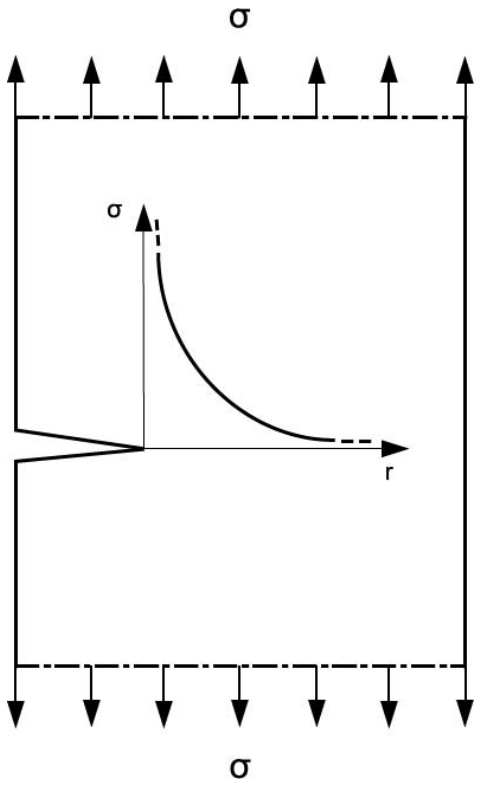

Figure 3.1: Stress distribution in relation to the distance from the crack. Modified after [12].

Crack propagation analysis can be made using an energy balance approach which in this case analyses how the propagation of the crack will affect the energy in the system. The energy release rate, G, is commonly used in this context and according to Griffith [9] the potential energy in the system after crack propagation is the same or reduced. The energy release rate, G, could also be described as the decrease in potential energy, Π, at an infinitely small increase in crack area, A. The potential energy, Π, is the sum of the elastic strain energy, U_e, and the potential energy from the loads, U_P.[9]

$$G = -\frac{\delta \Pi}{\delta A} = -\frac{\delta}{\delta A}(U_e + U_P) \tag{3.1}$$

The energy release rate depends on several parameters, for example the geometry of the structure, the geometry of the crack, the boundary conditions, the applied load and the stiffness of the material. For crack propagation, the following criterion should be met:

$$G = G_c \tag{3.2}$$

where G_c is a material parameter denoting the critical energy release rate of the material. It is also described as the energy required to propagate an initial and sharp crack by a unit area or as the energy dissipating at the tip of the crack when the crack propagates. In general terms, G is the energy available to grow a crack per unit area while G_c is the energy needed to grow a crack per unit area.[9]

3.2 Nonlinear fracture mechanics

LEFM has one mayor drawback: that the stress at the tip of the crack is theoretically infinite. In cases where the fracture process zone (FPZ) no longer is small in comparison to the length of the crack, the non-linearity is no longer negligible. Applying LEFM in such cases will generate unconservative predictions of the materials resistance to crack propagation. Further limitations with LEFM is that the fracture zone must be small in comparison to the size of the body. Nonlinear fracture mechanics (NLFM), quantifies and describes the nonlinear behavior in the FPZ. The approach based on NLFM considered within this dissertation, is also referred to as the cohesive crack model or the cohesive zone model (CZM).[9]

A stable uniaxial test is conducted by applying a force, F, over an area, A_{dim}, generating a tensile stress as

$$\sigma = \frac{F}{A_{dim}} \tag{3.3}$$

for example as illustrated in Figure 3.2. The test is performed in displacement control, where the displacement of the body sample is registered. The result is then presented with the tensile stress in relation to the change in length in the test specimen. A uniaxial test is conducted to achieve the complete curve, which includes the descending branch of the curve all the way to zero external load and complete fracture of the specimen.[9]

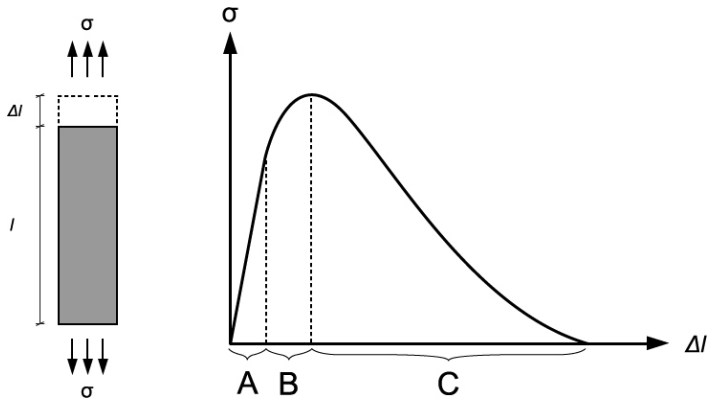

Figure 3.2: Uniaxial tension of the test specimen. Modified after [9].

As shown in Figure 3.2, the uniaxial test curve can be divided into three parts. In the initial phase, the material behaves in a linear elastic manner as described in the LEFM theory (A). Between the linear phase and the maximum material strength at the top of the curve, the material behaves in an initial nonlinear manner which may be due to small nonlinear elastic straining, plastic straining or microcracking (B). When reaching peak stress, a localized fracture process zone in the test specimen is created. As the crack displacement increases, the traction in the fracture process zone decreases which results in decreased stress (C).[9]

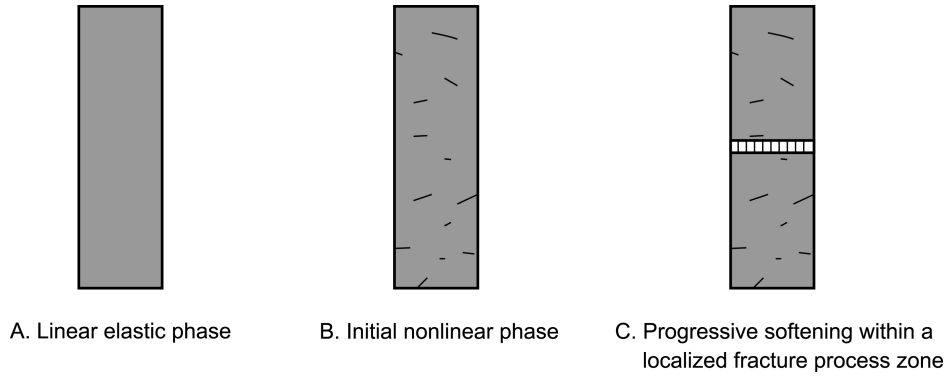

Figure 3.3: Different phases during uniaxial tension of the test specimen shown in Figure 3.2. Modified after [9].

In Figure 3.3, (C) is shown as a model, where the displacement in the test specimen is concentrated to a localised fracture plane and the rest of the specimen behaves elastically. In reality, the displacement is spread out over a larger zone and is not divided into two parts as the schematic model is assuming. The model is despite the simplification, a fair description of the displacement within the test specimen. In Figure 3.4, the simplification of (C) in Figure 3.3 is elaborated and the model is compared to reality. In the model, the lines between the two parts represent the cohesive forces in the material.[12][9]

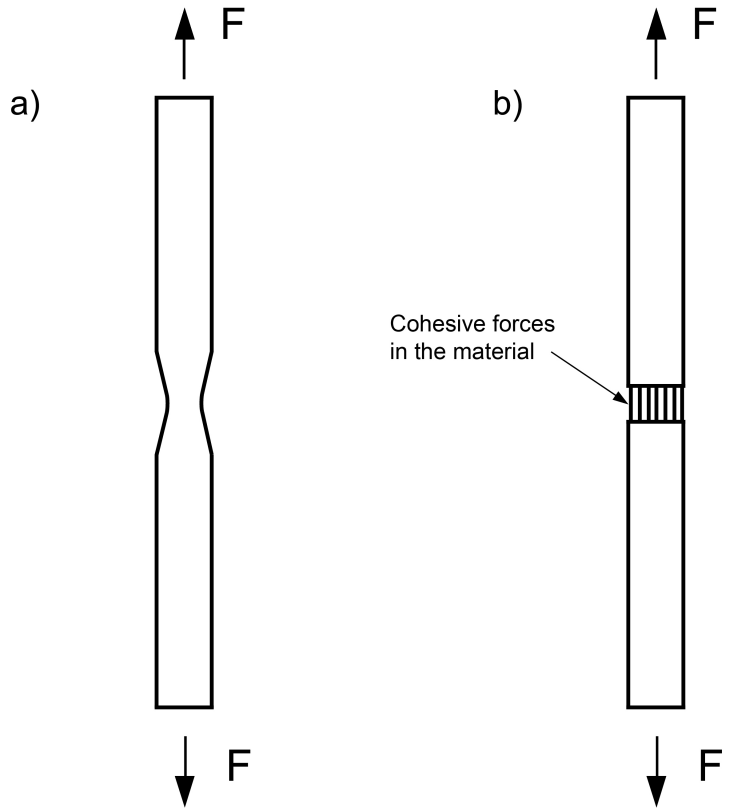

Figure 3.4: Visualization of test specimen in a) reality and b) model. Modified after [12].

When describing the uniaxial tension test, the concept with the cohesive zone model involves dividing the material behavior in two constitutive relations. A stress vs. strain

relation for the bulk material and a stress vs. deformation relation for the FPZ, as shown in Figure 3.5. The change in length of the test specimen, referred to as the total elongation, is divided into uniform straining outside the FPZ, εl, and into deformation inside the FPZ, δ. Further, the area beneath the stress vs. deformation curve is the fracture energy, G_f. The fracture energy, G_f, is defined as the energy dissipated during the process, from the creation of a fracture process zone crack to a traction free crack. The fracture energy, G_f, and the critical energy release rate, G_c are closely related but are not identical. G_c is commonly used to determine the critical energy for the propagation of a sharp crack while G_f is used for a specimen (with or without a notch) in a stable test run with displacement control, that fractures. G_c and G_f are theoretically equal for an ideally elastic material behavior outside the FPZ.[9]

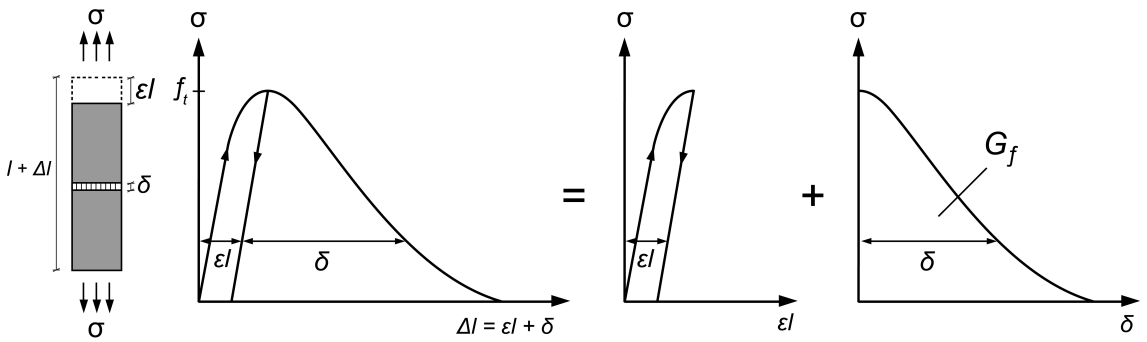

Figure 3.5: Relation between stress-strain and stress-deformation. Modified after [9].

The cohesive model is visualized in Figure 3.6. The traction-free part of the crack does not transfer stress since the faces are separated. In the fracture process zone, the traction between the crack faces follows the stress distribution indicated for $r < 0$ in Figure 3.6. In comparison to LEFM, where the stress is theoretically infinite, the stress has a finite value at the tip of the crack, f_t, in NLFM. The stress is in relation to the distance, r, which has the origin at the tip of the crack.[9]

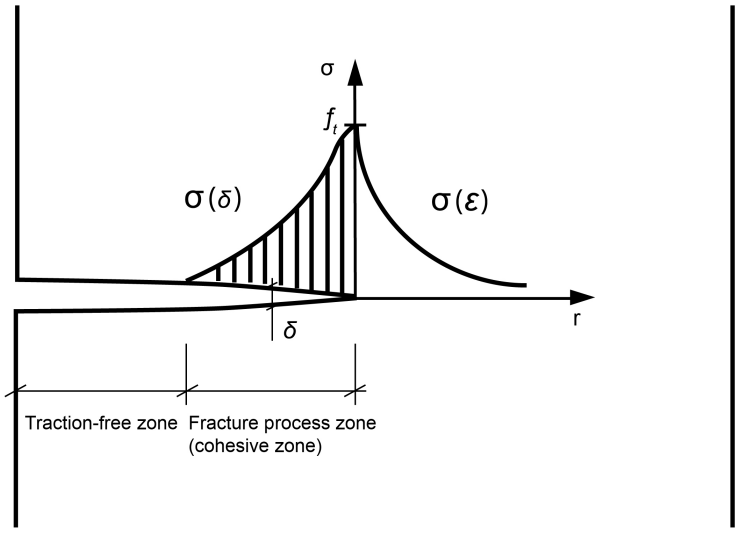

Figure 3.6: Stress distribution according to the cohesive zone model. Modified after [9].

3.3 Fracture mechanics of wood

As presented in subsection 2.4.1, wood is an orthotropic material which means that its material properties differs in three principal directions. The crack planes can be defined based on in which direction the normal to the crack plane is oriented, either in the L, R or T direction, and in which direction the crack propagates. This results in six different principal systems of crack propagation where the first letter denoted the normal to the crack plane and the second letter denotes the direction in which the crack propagates. The principal systems of crack propagation in wood is in the TL, TR, RL, RT, LR and LT directions which are visualized in Figure 3.8.[9][14]

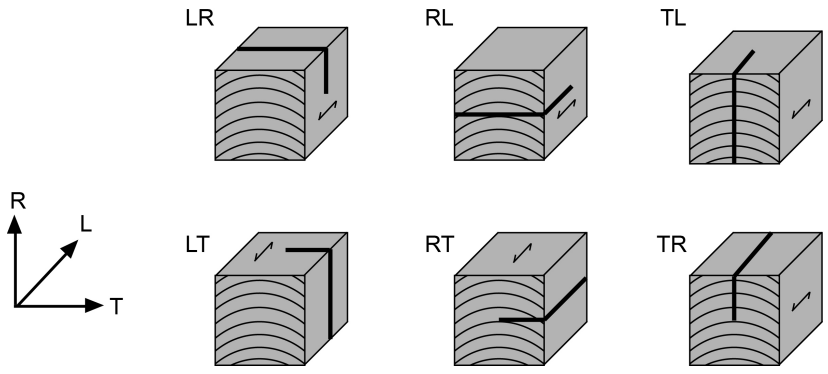

Figure 3.7: The six principal crack propagation direction in wood. Modified after [9].

There are three types of relative displacement considered in LEFM, referred to as modes of deformation. As illustrated in Figure 3.8, Mode I is due to tension perpendicular to the crack plane while Mode II is due to in-plane shear and Mode III is due to transverse shear.[9]

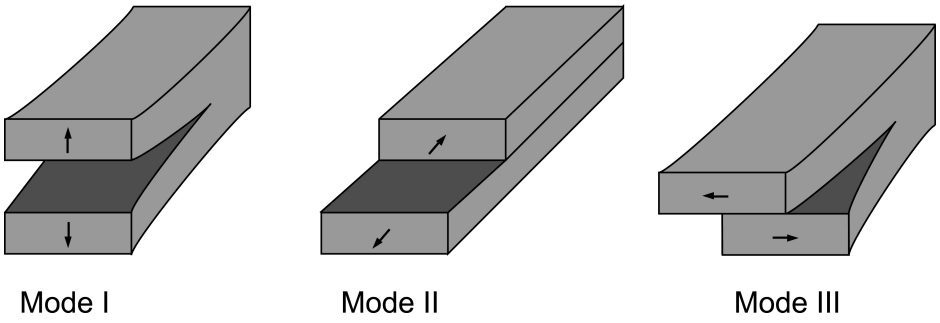

Figure 3.8: Mode I, II and III of deformation. Modified after [9].

In this dissertation only Mode I, also referred to as the opening deformation, is of interest. The test setup for creating a Mode I crack plane is the single edge notched beam (SENB) which is illustrated in Figure 3.9. This setup is commonly used to determine the fracture energy, G_f. One method that prescribes the SENB is the Nordtest method [16], which is the method the experimental work in this dissertation will be based on. Since the aim is to generate a load-displacement curve to evaluate the fracture energy, G_f, a notch is made in the bottom of the test specimen. It is also of importance that the test specimen is of relative small dimensions to avoid defects such as knots, resin pockets and grain misalignment in the body which could reduce the chance to get accurate values of the fracture energy.[18][9]

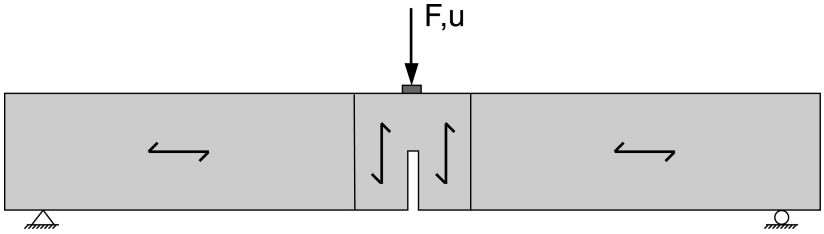

Figure 3.9: The single edge notched beam (SENB). Test setup used to determine fracture energy, G_f. Modified after [9].

In Figure 3.10, a stable response is visualized to the left and an unstable response is visualized to the right. The softening performance can simplified be described as how the curve behaves after the peak load to complete fracture. When the load has passed the peak, the material starts to soften and the surrounding material starts to unload as the applied load decreases. A stable response occurs when the unloading deformations are less than the softening. If not, the specimen needs to decrease its deformations but at the same time the testing machine forces it to increase generating a brittle failure, called an unstable response. If this happens, the area underneath the curve remains unknown and the possibility to calculate the fracture energy is gone.[33]

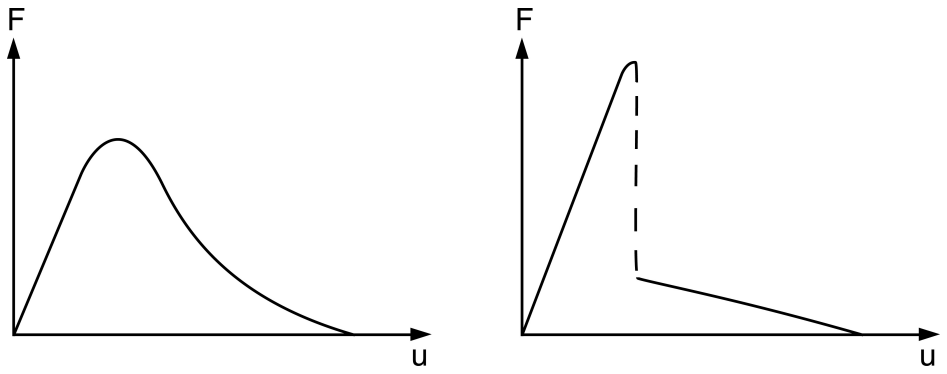

Figure 3.10: Visualization of a stable response to the left and an unstable response to the right.

A summary of various wood species and their respective values of fracture energy in different crack propagation directions, is presented in Table 3.1. For birch, the research is limited and therefore no values are presented.

Table 3.1: Specific fracture energy of various wood species tested in the RL, TL and TR direction. Modified after [19].

Species	Spec.fracture energy (J/m^2)		
	RL	TL	TR
Alder	240	160	-
Ash	550	340	-
Balsa	-	-	940
Beech	320-540	730	550-690
Birch	-	-	-
Larch	200	200	-
Oak (White)	350-370	270	320
Pine (Lodgepole, Scots,	250-420	420	630-920
Spruce (Norway, Red)	180-340	210-230	420-430
Yew (Common)	-	-	230-310

"-" values are unknown.

4 The Finite Element Method

The finite element (FE) method is used in the modeling part of the work in this dissertation. First, a general introduction is presented and thereafter a short derivation of the finite element formulation for three dimensional elasticity is presented. Different element types and a description of cohesive behavior are further introduced. Note that the FE-methodology presented in this chapter is only about the choices made and not about all the possible alternatives.

4.1 General

Problems found in engineering are often modeled and described by differential equations. Often, the differential equations are too complicated to be solved by classical analytical methods and numerical methods such as the finite element method may then be used. The finite element method is used to solve general differential equations using an approximate approach.[17]

The differential equations that describe the problem considered are assumed to hold for a certain region. The characteristics of the finite element method are that instead of finding an approximate solution for the entire region, the region is divided into smaller parts called *finite elements*. The calculation is then carried out for each element. Furthermore, the collection of all elements is called a *finite element mesh*. The numerical solution converges towards the exact solution as the number of elements increases and as the sizes of the elements decreases.[17]

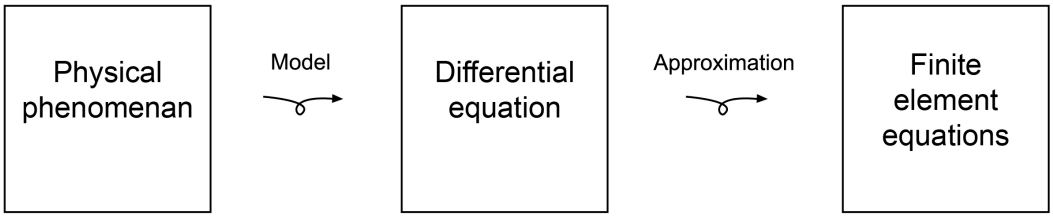

Figure 4.1: Steps in engineering analysis. Modified after [17].

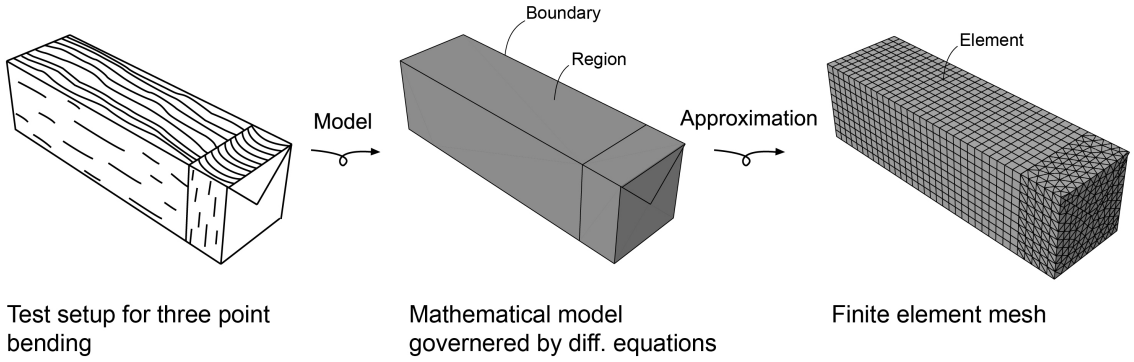

Figure 4.2: Illustration of modeling steps. Modified after [17].

The behavior for each element can be determined, when the approximation over each element has been determined. When the behavior for all the elements are determined, an approximate solution can finally be obtained for the behavior of the entire body. The finite element method is a numerical method for solving general differential equations and it has a wide field of application for solving physical problems. The FE-method can be applied for arbitrary differential equations.[17]

4.2 Weak form of three dimensional elasticity

The elasticity equations formulated in this section are amongst the most important within the FE-method and are applicable for any solid material. The differential equation of equilibrium for three dimensional problems is defined as

$$\tilde{\nabla}^T \boldsymbol{\sigma} + \boldsymbol{b} = 0 \tag{4.1}$$

where

$$\tilde{\nabla}^T = \begin{bmatrix} \frac{\partial}{\partial x} & 0 & 0 & \frac{\partial}{\partial y} & \frac{\partial}{\partial z} & 0 \\ 0 & \frac{\partial}{\partial y} & 0 & \frac{\partial}{\partial x} & 0 & \frac{\partial}{\partial z} \\ 0 & 0 & \frac{\partial}{\partial z} & 0 & \frac{\partial}{\partial x} & \frac{\partial}{\partial y} \end{bmatrix}; \quad \boldsymbol{\sigma} = \begin{bmatrix} \sigma_{xx} \\ \sigma_{yy} \\ \sigma_{zz} \\ \sigma_{xy} \\ \sigma_{xz} \\ \sigma_{yz} \end{bmatrix}; \quad \boldsymbol{b} = \begin{bmatrix} b_x \\ b_y \\ b_z \end{bmatrix} \tag{4.2}$$

where $\tilde{\nabla}$ is the matrix differential operator, $\boldsymbol{\sigma}$ is the stress vector and $\boldsymbol{b}$ is a body force vector. To derive the weak form, equations 4.1 are multiplied with arbitrary weight functions, $\boldsymbol{v}$, and then integrated over the volume, V. Then an integration by parts is performed using the Green-Gauss theorem. By using the equation for the traction vector in the x-direction, t_x, in equation 4.3, the differential equations can be further reduced. The unit normal vector is denoted $\boldsymbol{n}$.[17]

$$\boldsymbol{t} = \begin{bmatrix} t_x \\ t_y \\ t_z \end{bmatrix}; \qquad \begin{aligned} t_x &= \sigma_{xx}n_x + \sigma_{xy}n_y + \sigma_{xz}n_z \\ t_y &= \sigma_{yx}n_x + \sigma_{yy}n_y + \sigma_{yz}n_z \\ t_z &= \sigma_{zx}n_x + \sigma_{zy}n_y + \sigma_{zz}n_z \end{aligned} \tag{4.3}$$

By doing the corresponding steps for the y-direction and z-direction the equation can be formulated in a three dimensional manner where $\mathbf{v}$ is the arbitrary weight vector as

$$\mathbf{v} = \begin{bmatrix} v_x \\ v_y \\ v_z \end{bmatrix}; \quad \tilde{\nabla}\mathbf{v} = \begin{bmatrix} \frac{\partial v_x}{\partial x} \\ \frac{\partial v_y}{\partial y} \\ \frac{\partial v_z}{\partial z} \\ \frac{\partial v_x}{\partial y} + \frac{\partial v_y}{\partial x} \\ \frac{\partial v_x}{\partial z} + \frac{\partial v_z}{\partial x} \\ \frac{\partial v_y}{\partial z} + \frac{\partial v_z}{\partial y} \end{bmatrix} \tag{4.4}$$

the weak form can finally be formulated as

$$\int_V (\tilde{\nabla}\mathbf{v})^T \boldsymbol{\sigma} dV = \int_S \mathbf{v}^T \boldsymbol{t} dS + \int_V \mathbf{v}^T \boldsymbol{b} dV \tag{4.5}$$

The derivation above is simplified. The full derivation is presented by Ottosen and Petersson [16].

4.3 The finite element formulation of three dimensional elasticity

Using equation 4.5, which is the weak form of equilibrium, the FE-equations for three dimensional elasticity can be derived. The displacement vector is denoted $\boldsymbol{u}$, the weight vector, $\mathbf{v}$, nodal point displacements, $\boldsymbol{a}$, and the shape functions, $\boldsymbol{N}$. The relation between them are described as

$$\boldsymbol{u} = \boldsymbol{N}\boldsymbol{a} \tag{4.6}$$

$$\mathbf{v} = \boldsymbol{N}\boldsymbol{c} \tag{4.7}$$

where the weight vector is formulated using the Galerkin method. Since $\mathbf{v}$ is arbitrary it follows that the matrix $\boldsymbol{c}$ is arbitrary. Multiplying with the matrix differential operator gives

$$\tilde{\nabla}\mathbf{v} = \boldsymbol{B}\boldsymbol{c} \quad \text{where} \quad \boldsymbol{B} = \tilde{\nabla}\boldsymbol{N} \tag{4.8}$$

By using equation 4.7 and equation 4.8 in the weak form and noting that $\boldsymbol{c}$ is independent of the coordinates and that the matrix is arbitrary, the result becomes

$$\int_V \boldsymbol{B}^T \boldsymbol{\sigma} dV = \int_S \mathbf{N}^T \boldsymbol{t} dS + \int_V \mathbf{N}^T \boldsymbol{b} dV \tag{4.9}$$

Introducing the constitutive model where $\boldsymbol{D}$ is the constitutive matrix, $\boldsymbol{\varepsilon}$ is the strain and $\boldsymbol{\varepsilon_0}$ the initial strain, which normally depends on temperature changes. If there is initial strain, it can be calculated independently and the material is assumed to respond thermoelastically.[17]

$$\boldsymbol{\sigma} = \boldsymbol{D\varepsilon} - \boldsymbol{D\varepsilon_0} \tag{4.10}$$

The kinematic relation is stated as

$$\boldsymbol{\varepsilon} = \tilde{\boldsymbol{\nabla}} \boldsymbol{u} \tag{4.11}$$

Combining the kinematic relation in equation 4.11 with equation 4.6, equation 4.8 and equation 4.10, the results becomes

$$\boldsymbol{\sigma} = \boldsymbol{DBa} - \boldsymbol{D\varepsilon_0} \tag{4.12}$$

There are two types of boundary conditions used. The *natural boundary condition* where a prescribed traction vector, $\boldsymbol{t}$, is used and an *essential boundary condition* where a prescribed displacement vector, $\boldsymbol{u}$, is used. In equation 4.13 the boundary conditions are stated where both $\boldsymbol{h}$ and $\boldsymbol{g}$ are known vectors. The total boundary, S, consist of both S_h and S_g.

$$\begin{aligned} \boldsymbol{t} = \boldsymbol{Sn} = \boldsymbol{h} \quad &\text{on} \quad S_h \\ \boldsymbol{u} = \boldsymbol{g} \quad &\text{on} \quad S_g \end{aligned} \tag{4.13}$$

When combing the boundary conditions with equations 4.12 and equation 4.9, the FE-formulation sought can be presented as

$$\begin{aligned} \boldsymbol{K} &= \int_V \boldsymbol{B^T D B} dV \\ \boldsymbol{f_b} &= \int_{S_h} \boldsymbol{N^T h} dS + \int_{S_g} \boldsymbol{N^T t} dS \\ \boldsymbol{f_l} &= \int_V \boldsymbol{N^T b} dV \\ \boldsymbol{f_0} &= \int_V \boldsymbol{B^T D \varepsilon_0} dV \end{aligned} \tag{4.14}$$

where $\boldsymbol{K}$ is the stiffness matrix, $\boldsymbol{f_b}$ is the boundary load vector, $\boldsymbol{f_l}$ is the body force vector, $\boldsymbol{f_0}$ is the initial strain vector. The relation can then be formulated as

$$\boldsymbol{Ka} = \boldsymbol{f_b} + \boldsymbol{f_l} + \boldsymbol{f_0} \tag{4.15}$$

The derivation above is simplified. The full derivation is presented by Ottosen and Petersson [17].

4.4 Tetrahedral and hexahedral elements

When creating a mesh in 3D, different types of element geometry can be used. Which type of geometry to use depends on the shape of the mesh itself. The simplest three dimensional element is the four noded tetrahedral. When using nodal points midways between the four corner points, the ten nodal tetrahedral is obtained. The four node and ten node tetrahedrals are shown in Figure 4.3. The generalized approximation for the ten node tetrahedral becomes

$$T = \alpha_1 + \alpha_2 x + \alpha_3 y + \alpha_4 z + \alpha_5 x^2 + \alpha_6 y^2 + \alpha_7 z^2 + \alpha_8 xy + \alpha_9 xz + \alpha_{10} yz \qquad (4.16)$$

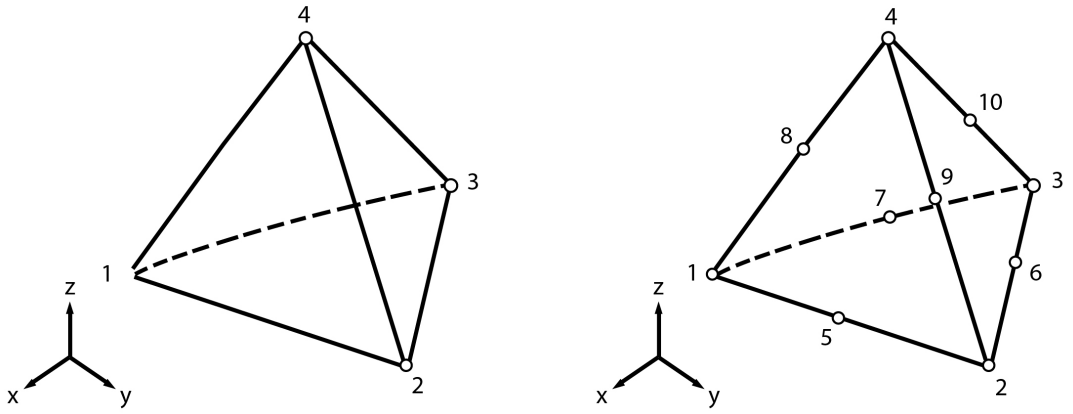

Figure 4.3: The four and ten node tetrahedrals. Modified after [17].

For three dimensional prism shaped geometries, also referred to as hexahedral elements, the version with fewest nodes is the eight node prism element. When using nodal points midways between the eight nodal points, the twenty nodal tetrahedral is obtained. The eight node and twenty node tetrahedrals are shown in Figure 4.4. The generalized approximation for the eight node hexahedral becomes

$$T = \alpha_1 + \alpha_2 x + \alpha_3 y + \alpha_4 z + \alpha_5 x^2 + \alpha_6 y^2 + \alpha_7 z^2 + \alpha_8 xyz \qquad (4.17)$$

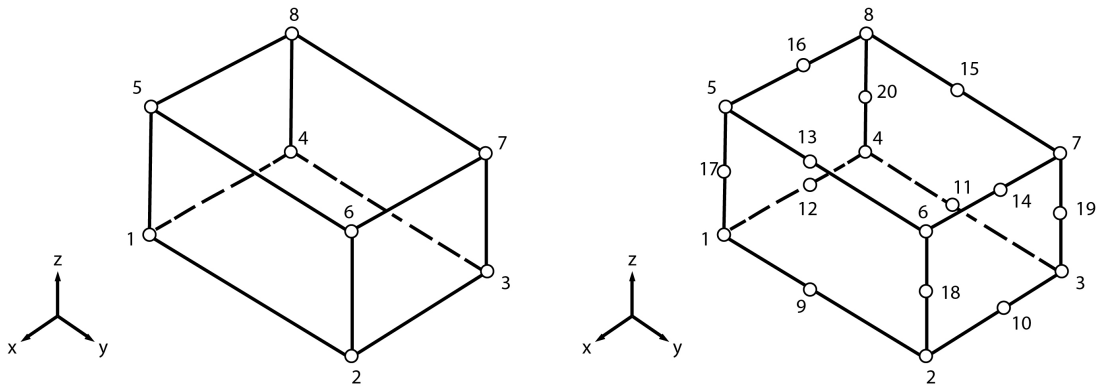

Figure 4.4: The eight and twenty nodal hexahedral. Modified after [17].

The generalized approximation of the element geometries is connected to the global shape functions and adapted into the FE-formulation presented in section 4.3 by

$$T = \boldsymbol{N}\boldsymbol{a} \tag{4.18}$$

4.5 Cohesive behavior

There are several alternatives when it comes to implementing a cohesive zone model. The options available in Abaqus include implementing a surface-based cohesive behavior or by creating cohesive zone elements. The cohesive zone model is a gradual phenomenon of fracture, where separation occurs over an extended crack tip but is resisted by the cohesive traction force. The cohesive behavior is not representing a material on its own but representing the cohesive forces when the material elements are being pulled apart [15]. The surface-based cohesive behavior and its background within FE-methodology are further presented in this section.[20]

4.5.1 Linear elastic traction-separation law

A linear elastic traction-separation law prior to initiation of damage is assumed. The elastic behavior is formulated using normal and shear stress which relate to the normal and shear separations over the extension of the crack. The nominal traction stress vector, $\boldsymbol{t}$, consists of three parameters; the normal, t_n, and the two shear tractions, t_s and t_t. The stiffness matrix is denoted $\boldsymbol{K}$, and the corresponding separations are denoted $\boldsymbol{\delta}$.[20]

$$\boldsymbol{t} = \begin{bmatrix} t_n \\ t_s \\ t_t \end{bmatrix} = \begin{bmatrix} K_{nn} & K_{ns} & K_{nt} \\ K_{ns} & K_{ss} & K_{st} \\ K_{nt} & K_{st} & K_{tt} \end{bmatrix} \begin{bmatrix} \delta_n \\ \delta_s \\ \delta_t \end{bmatrix} = \boldsymbol{K}\boldsymbol{\delta} \tag{4.19}$$

4.5.2 Damage initiation

After the linear elastic traction-separation response, damage behavior is used to describe the degradation, i.e the diminishing stress-transferring capability. The model formulation is divided into two parts, the initiation criterion and the damage evolution. A typical traction-separation curve with both the linear elastic and the strain softening part is shown in Figure 4.5, for a local contact point in the material.[20]

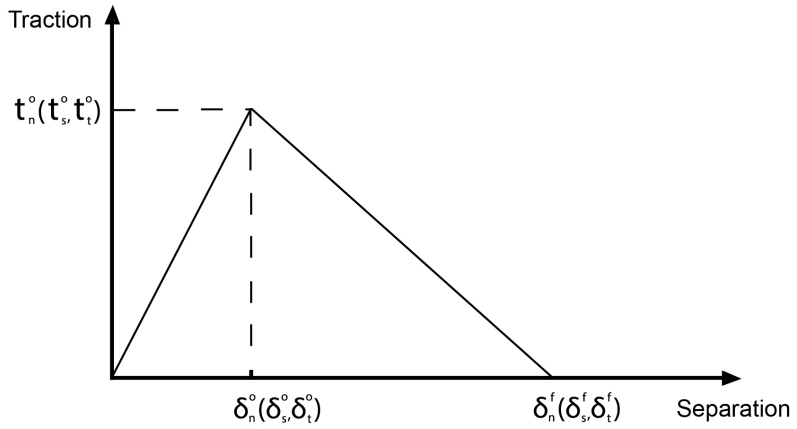

Figure 4.5: A typical traction-separation curve in a local material point. Modified after [20].

The damage initiation criterion defines the start of the degradation response. This starts when the contact stress reaches the damage initiation criterion. The peak value for the contact stress in pure normal, first shear or second shear direction are denoted as t_n^0, t_s^0 or t_t^0, respectively. The Macaulay bracket used around t_n^0 in equation 4.20 means that only tensile stress initiates damage. The criterion used for the maximum stress is given as

$$max \left\{ \frac{\langle t_n \rangle}{t_n^0}, \frac{t_s}{t_s^0}, \frac{t_t}{t_t^0} \right\} = 1 \tag{4.20}$$

4.5.3 Damage evolution

The rate of how the cohesive stiffness is degraded after the initiation criterion is reached, is described by the damage evolution law. To describe the overall damage at the contact point, a scalar damage variable, D is introduced. The value varies when the damage evolution is initialized, from $D = 0$ to $D = 1$ for complete damage. The contact stress components t_n^0, t_s^0 or t_t^0 are based on the elastic traction-separation behavior, when no damage has developed. The stress components are affected by the scalar damage variable as

$$t_n = \begin{cases} (1-D)\bar{t_n}, & \bar{t_n} \geq 0 \\ \bar{t_n} \end{cases}$$

$$t_s = (1-D)\bar{t_s} \tag{4.21}$$

$$t_t = (1-D)\bar{t_t} \tag{4.22}$$

For combined normal and shear separations, the evolution of damage at the interface is described as a function of the effective separation δ_m:

$$\delta_m = \sqrt{\langle \delta \rangle_n^2 + \delta_s^2 + \delta_t^2} \tag{4.23}$$

The damage variable is used as an input value to determine the stress components. The damage variable for a linear softening curve according to Figure 4.5 is given by

$$D = \frac{\delta_m^f(\delta_m^{max} - \delta_m^o)}{\delta_m^{max}(\delta_m^f - \delta_m^o)} \tag{4.24}$$

where

$$\delta_m^f = \frac{2G_f}{T_{eff}^o} \tag{4.25}$$

with the effective traction at damage initiation, δ_m^f, the maximum effective separation during the loading history, δ_m^{max}, the fracture energy, G_f, and the effective traction at damage T_{eff}^o.[20]

4.5.4 Viscous regularization

Viscosity coefficients can be specified as damage stabilization coefficients. These can be used to overcome convergence problems in Abaqus which the model can exhibit with various shapes on the softening behavior and on the stiffness degradation. This can be applied both for cohesive elements and for surface-based cohesive behavior. Regulating the viscosity coefficient makes the tangent stiffness matrix, $\boldsymbol{K}$, positive definite for sufficiently small time increments.[20]

5 Experimental determination of fracture characteristics

The fracture energy is determined experimentally by using a modified version of the Nordtest method. In this chapter, the test setup and the test specimen are described, as well as the preparation and the implementation during the experimental work. How the evaluation of the results is made is then stated, before the experimental results are presented.

5.1 Method

The experimental work is based on the Nordtest method [16]. The test setup is shown in Figure 5.1 and in Figure 5.2, and the test specimen geometry is shown in Figure 5.3. The test specimens are loaded as simply supported beams where the aim is to create tension perpendicular to the grain, Mode I. The test setup and theoretical approach is the same as SENB (see subsection 3.3). The beam is loaded in three-point bending and therefore the test setup is more commonly referred to as single edge notched beam loaded in three point bending (SEN-TPB). The aim is to induce a crack propagation in the TL direction until failure, using a stable test run with a displacement controlled loading of the specimen. The fracture energy, G_f, is determined from the work done by the applied load during the complete loading process, using equation 5.1. The Nordtest method was used with modifications regarding the test specimen geometry and the sawn notch geometry as described below.

5.1.1 Test setup and specimens

Figure 5.2 shows the used test setup. The specimens were tested as simply supported beams, with a steel prism resting on a steel ball at one end and a steel prism resting on a steel cylinder at the other end. The tests were performed with displacement controlled loading, with load introduction at the midpoint of the beam, and with a rate of 2 mm/minute.

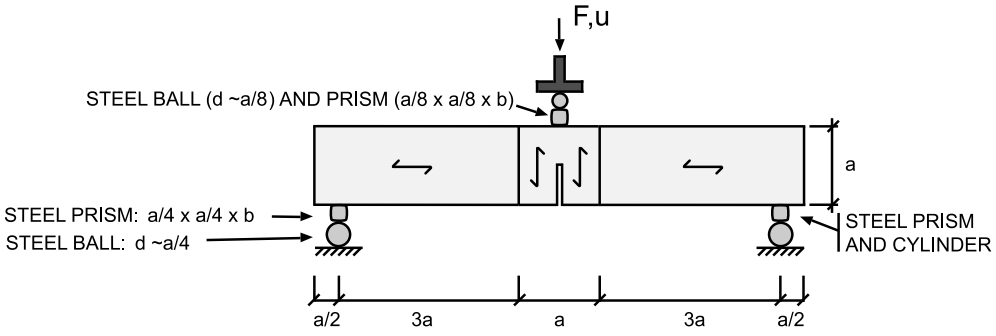

Figure 5.1: Test setup for the Nordtest method. Modified after [16].

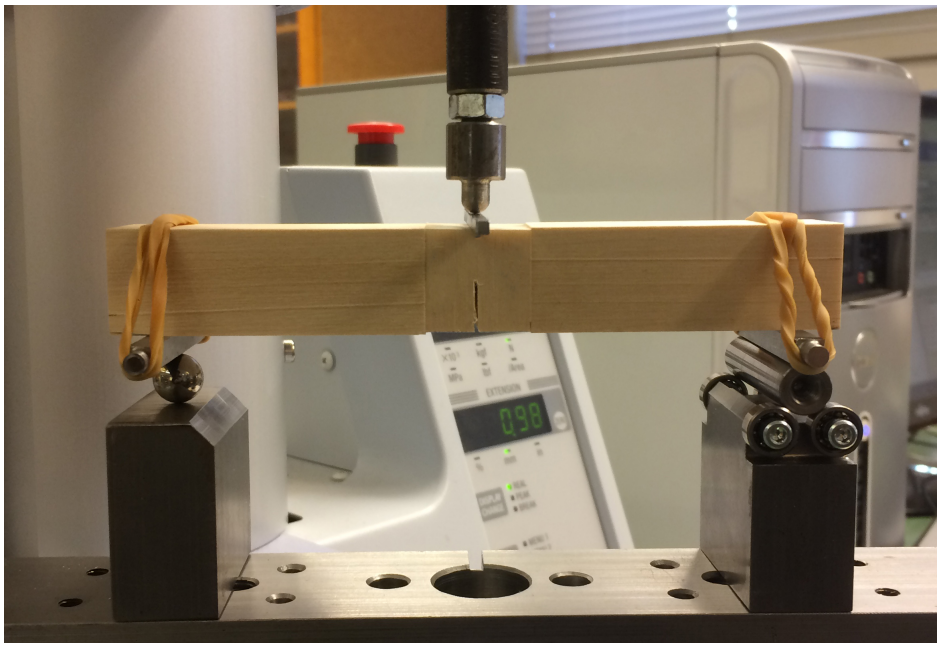

Figure 5.2: Test setup used in the experimental work.

The test specimens were composed of three pieces of wood glued together to form a beam with a total length of 140 mm, as visualized in Figure 5.3. The middle pieces were oriented to achieve a fracture plane oriented in the TL direction, see subsection 3.3. The notches were made at the bottom of the middle pieces and the aim was to achieve a cut as the one shown in Figure 5.4 a) and to avoid getting defective shapes as visualized in Figure 5.4 b).[16]

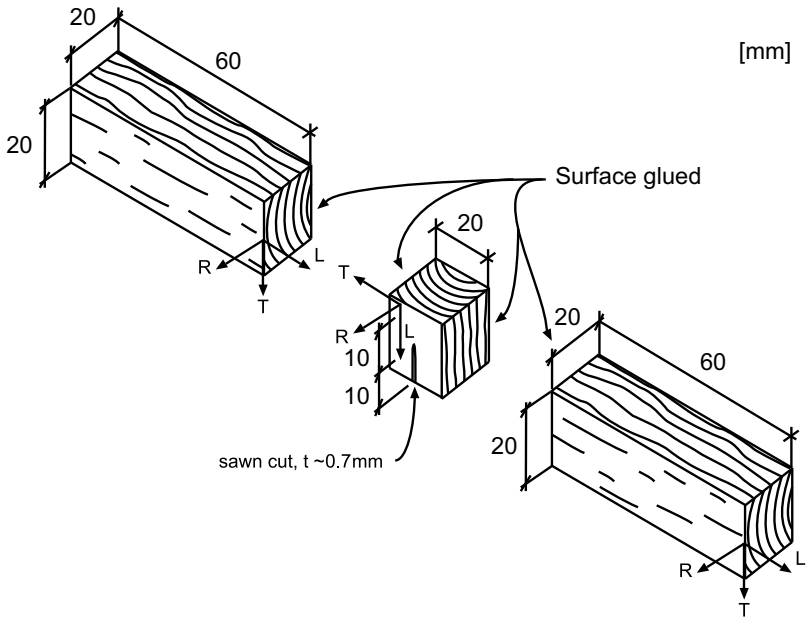

Figure 5.3: Illustration of the test specimen. Modified after [14] and [16].

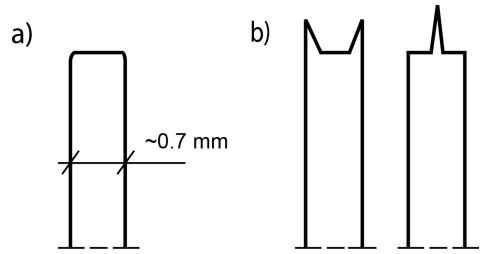

Figure 5.4: a) Desired shape of notch. b) Defective shapes. Modified after [16]

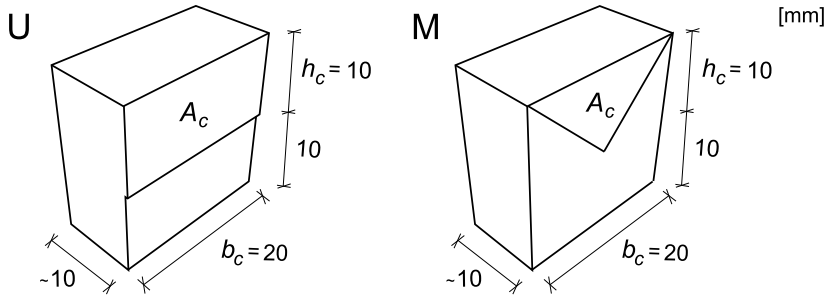

Figure 5.5: Dimensions on the sawn cut for the rectangular shape (U) and the triangular shape (M).

Specimens with two different types of notch geometries were tested; the rectangular shape (U) and the triangular shape (M). The rectangular shape is visualized to the left and the triangular to the right in Figure 5.5. The height, h_c, is 10 mm for both geometries and is defined as the vertical distance from the tip of the notch to the top of the middle piece. The width, b_c, is 20 mm for both geometries and is defined as the width of the middle piece. A_c is the area of the middle piece.

5.1.2 Preparation and implementation

Two birch planks were divided into two halves as shown in Figure 5.6. One of the planks was then left untreated, as a reference, and the other half was chemically modified by acetylation as described in subsection 2.3.3. Note that the acetylation process was designed for a different wood species than birch.

Two sticks with the approximate dimensions $20 \times 20 \times 150$ mm^3 were extracted from each plank, in total eight sticks. From each stick, five test specimens for experimental tests of fracture energy and one piece for moisture content measurement, were obtained. Both the untreated and the acetylated birch were conditioned at a temperature of $20.2 \pm 0.2°C$ and a relative humidity of 63 ± 2 %.

All test specimens were numbered, the numbering system used can be seen in Figure 5.6 and is further explained in Figure 5.7. For the pieces used for moisture content measurements, the numbering system is the same as for the test specimens, but the last digit was instead replaced with "RH", for relative humidity.

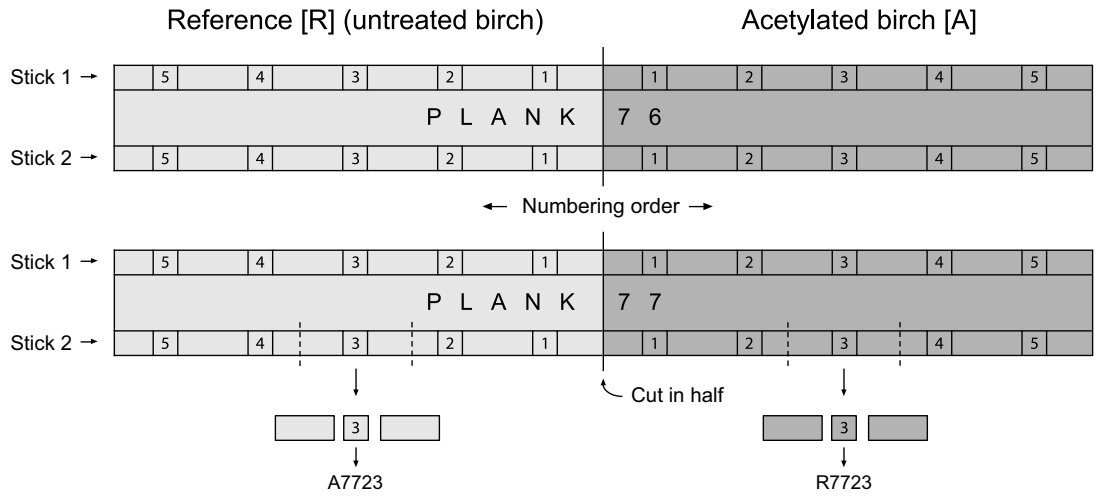

Figure 5.6: The system of sawing and numbering test specimens.

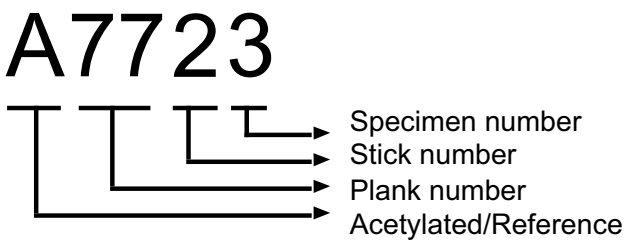

Figure 5.7: Numbering system of test specimens.

The test specimens were stored in the conditioned climate until equilibrium was reached. Equilibrium in this case is defined as a change in weight to be less than 0.1 % after 24 hours. The dimensions of the middle pieces were measured and were approximated to the nearest 0.01 mm. The 0.7 mm saw cuts were made just before conducting the fracture energy tests.

The following steps were followed during the fracture energy tests

1. By using rubber bands, steel prism were attached to the test specimen.
2. The test specimen, with the attached steel prisms, was placed on a steel ball at one end and a steel cylinder at the other.
3. A steel prism was placed on top of the beam.
4. The loading equipment was lowered to just above the steel prism.
5. The test started and ran until complete failure, or F=0.00 N.

In Figure 5.8, an illustration of all the test specimens with their respective notch geometries (rectangular (U) or triangular (M)) is shown. The notch geometry shape

used for each plank was not as systematic as first intended. The first experimental tests were conducted with rectangular shapes. They generated unstable responses and stable responses are a necessity to be able to calculate the fracture energy. Therefore, different notch geometries were investigated. By FE-analyses (see section 6.3) it was concluded that a triangular shape would lower the maximum load, and increase the chances of achieving stable responses.

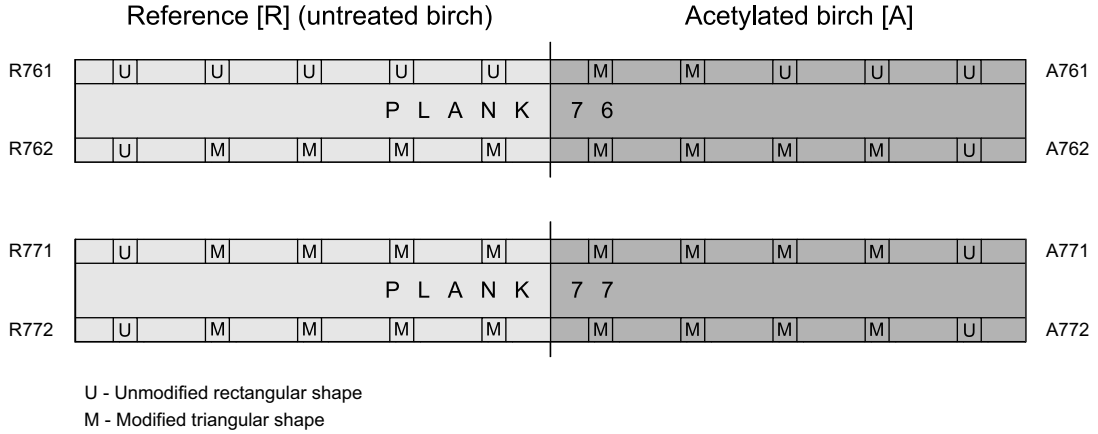

Figure 5.8: Illustration of all test specimens with either rectangular notch geometry (U) or triangular notch geometry (M).

A summary of the amount of test specimens with rectangular and triangular notch geometries are shown in Table 5.1. The total number of test specimens was 40.

Table 5.1: Number of test specimens with different shapes.

	Number of test specimens	**Number of rectangular shape (U)**	**Number of triangular shape (M)**
Reference (R)	20	8	12
Acetylated (A)	20	6	14

In order to perform measurements of moisture content for the different planks, the oven dry method was used, according to SS-EN 13183-1. The pieces named "RH" were put in an oven maintaining a temperature of $105°C$ until the change of weight was less than 0.01 gram over a 24 h time period.[22]

5.1.3 Evaluation of results

The fracture energy, G_f, is determined according to the Nordtest method [16] as:

$$G_f = \frac{W + mgu_0}{A_c} \tag{5.1}$$

where

$$m = \frac{5}{6}m_{tot} + 2m_{prism} \tag{5.2}$$

The total mass of the specimen, m_{tot}, and the mass of the steel prism, m_{prism}, are input parameters to calculate the mass, m, in equation 5.2. In equation 5.1, W is the work calculated as the integral of the load-displacement curve, g is the gravitational acceleration, u_0 is the end deflection and A_c is the critical area (as shown in Figure 5.5).[16]

The density, ρ, of the test specimen was determined with equation 5.3. The mass of the test specimen, m_{eq}, was determined when the test specimen reached equilibrium, i.e. a change of weight less than 0.1 % after 24 hours [16]. The dimensions of the specimen, a,b, and l, were measured after the test specimen reached equilibrium.

$$\rho = \frac{m_{eq}}{a \cdot b \cdot l} \tag{5.3}$$

The moisture content was determined by equation 2.1 in section 2.2.1 and is defined as the weight of the water in the wood divided by the weight of the wood in its oven dry state, often expressed in percent by multiplying the result by 100.[26]

From the laboratory work, data showing the load-displacement response was achieved. The area underneath the curve is the work, W, done by the midpoint load as visualised in Figure 5.9. The work stands for $95-97$ % of the fracture energy and is determined by calculating the integral in MATLAB using a trapezoidal numerical integration scheme.

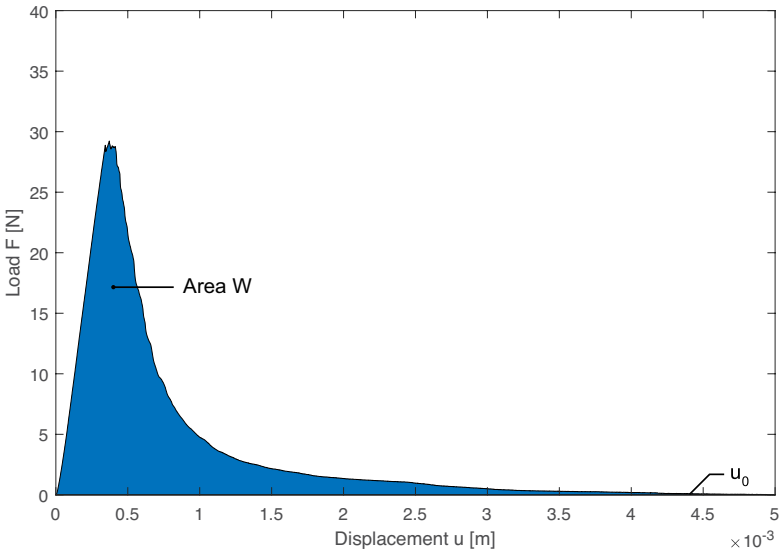

Figure 5.9: Schematic illustration of load-displacement curve obtained from the experiments.

5.2 Experimental results

5.2.1 Density and moisture content

The density and a comparison between reference and acetylated test specimens, are shown in Table 5.2. The test specimens weight and dimensions used to calculate the

density are presented in Appendix A. The results show approximately a 12 % increase in mean density for acetylated birch compared to the untreated birch.

Table 5.2: Mean value and standard deviation of density for reference (R) and acetylated specimens (A).

Reference		**Density** ρ [kg/m^3]		**Acetylated**		**Density** ρ [kg/m^3]		
Test group	**No. of test specimens**	**Mean value**	**Std**	**Test group**	**No. of test specimens**	**Mean value**	**Std**	**Percent Change [%]**
R761	6	609.16	3.28	A761	6	665.84	10.20	9.31
R762	6	650.43	4.64	A762	6	704.91	5.22	8.38
R771	6	711.84	8.34	A771	6	834.72	14.64	17.26
R772	6	702.75	1.69	A772	6	796.59	8.93	13.35
Total	24	668.55	4.49	Total	24	750.52	9.75	12.07

The results of the moisture content are shown in Table 5.3. The results show a decrease in mean value of the moisture content from approximately 11 % to 3 % when acetylated.

Table 5.3: Moisture content for both reference (R) and acetylated (A) specimen.

Specimen ID	**Moisture content** [%]	**Specimen ID**	**Moisture content** [%]
R761RH	11.08	A761RH	2.87
R762RH	10.98	A762RH	3.08
R771RH	10.80	A771RH	3.15
R772RH	10.99	A772RH	3.16
Mean value:	10.96	Mean value:	3.07
Standard Deviation:	0.10	Standard Deviation:	0.12

5.2.2 Notch geometry impact on experimental results

For the reference specimens, the mean value of the maximum load decreased from 123 N to 39 N. This is a 68 % decrease of the maximum load when using the triangular shape (M) instead of the rectangular shape (U). In Table 5.4, the number of stable vs. unstable responses are summarized. Only one of the reference specimens with the rectangular shape generated a stable response. Out of the triangular shaped, four out of twelve generated stable responses.

For the acetylated birch the mean value of the maximum load decreased from 90 N to 28 N when using the triangular shape (M) instead of the rectangular shape (U). This is a 69 % decrease of the maximum load. All of the rectangular shapes for the acetylated specimens generated unstable responses, while eleven out of fourteen test specimens with the triangular shapes generated stable responses.

Table 5.4: Summary of experimental results on notch geometry, stable and unstable responses for both reference and acetylated test specimens.

	Reference (R)		**Acetylated (A)**	
	Rectangular shape (U)	**Triangular shape (M)**	**Rectangular shape (U)**	**Triangular shape (M)**
Number of stable responses	1	4	0	11
Number of unstable responses	7	8	6	3

5.2.3 Fracture energy and maximum load

In Figure 5.10, typical load-displacement curves for reference and acetylated test specimen with rectangular shapes (U) are shown. In Figure 5.11, typical load-displacement responses for reference and acetylated test specimens with triangular shapes (M) are shown. A typical load-displacement curve in this case is a curve with maximum load closest to the mean value of the maximum load. In Appendix B, all the individual test specimens and their respective load-displacement curves are presented.

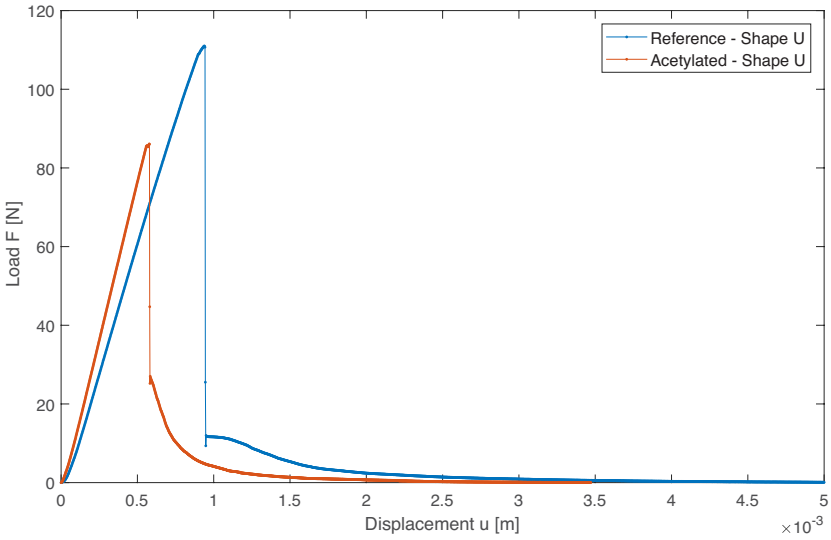

Figure 5.10: Typical load-displacement curves for reference and acetylated test specimens with rectangular shapes (U).

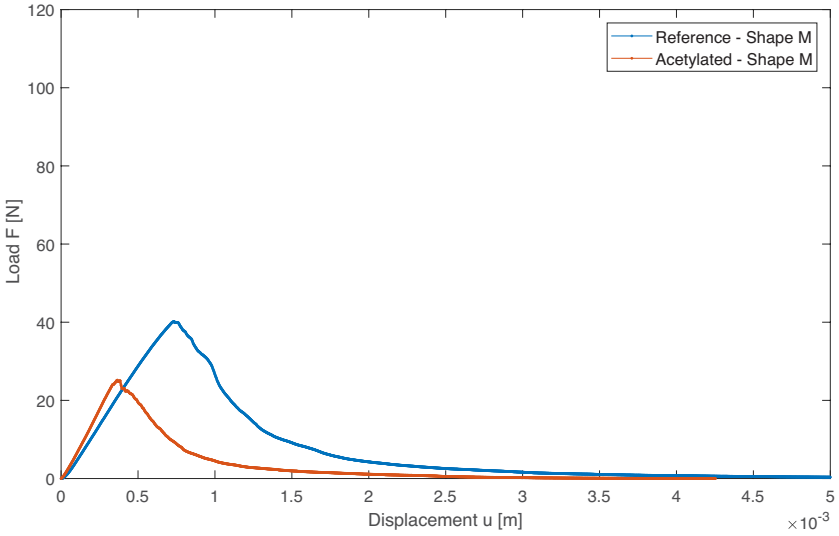

Figure 5.11: Typical load-displacement curves for reference and acetylated test specimens with triangular shapes (M).

In Table 5.5 and 5.6, both mean value and standard deviation of the fracture energy are presented. The tables show the number of stable and unstable responses for both

reference and acetylated test specimens and for the two notch geometries. In Appendix B, all the calculated fracture energies are presented for all the individual test specimens. Only stable responses are of interest when investigating the fracture energy. Due to the instant drop in the load-displacement curves for unstable responses, the value of the fracture energy is unreliable. For stable responses considering specimens with a triangular shaped notch (M), the mean value of the fracture energy equals 426.6 J/m^2 for the reference test specimens and 193.9 J/m^2 for the acetylated test specimens. That equals a 55 % decrease of the mean value of the fracture energy for acetylated birch compared to untreated birch. For specimens with a rectangular shaped notch (U), only one stable response was obtained. Therefore, the same comparison between reference and acetylated test specimens could not be made.

Table 5.5: A summary of mean value and standard deviation of the fracture energy, G_f, for reference specimens with two notch geometries.

	Fracture energy, G_f [J/m^2]					
	Reference (R)					
	Rectangular shape (U)			**Triangular shape (M)**		
	No. of test specimens	Mean value	Std	No. of test specimens	Mean value	Std
Stable responses	1	537.91	0.00	4	426.64	37.54
Unstable responses	7	350.86	63.45	8	406.18	28.58

Table 5.6: A summary of mean value and standard deviation of the fracture energy, G_f, for acetylated specimens with two notch geometries.

	Fracture energy, G_f [J/m^2]					
	Acetylated (A)					
	Rectangular shape (U)			**Triangular shape (M)**		
	No. of test specimens	Mean value	Std	No. of test specimens	Mean value	Std
Stable responses	0	-	-	11	193.88	40.90
Unstable responses	6	211.60	53.02	3	194.78	36.78

In Table 5.7 and 5.8, both mean values and standard deviation of the maximum load are presented. The tables show number of stable and unstable responses for both reference and acetylated test specimen and for the two notch geometries. In Appendix B, all the calculated maximum load are presented for all the individual test specimens. Stable responses for reference specimens with a triangular shape show a mean value for the maximum load of approximately 39.5 N, for the acetylated specimens the corresponding value is 28.5 N. That equals a decrease of approximately 28 % of the mean value of the maximum load for acetylated birch compared to untreated birch.

Table 5.7: A summary of mean value and standard deviation of the maximum load for reference specimens with two notch geometries.

	Maximum load [N]					
	Reference (R)					
	Rectangular shape (U)			**Triangular shape (M)**		
	No. of test specimens	Mean value	Std	No. of test specimens	Mean value	Std
Stable responses	1	123.43	0.00	4	39.46	4.95
Unstable responses	7	111.03	10.89	8	45.36	6.16

Table 5.8: A summary of mean value and standard deviation of the maximum load for acetylated test specimens with the two notch geometries.

	Maximum load [N]					
	Acetylated (A)					
	Rectangular shape (U)			**Triangular shape (M)**		
	No. of test specimens	Mean value	Std	No. of test specimens	Mean value	Std
Stable responses	0	-	-	11	28.46	8.60
Unstable responses	6	90.01	19.82	3	28.83	4.48

5.2.4 Impact of density on fracture energy

In Figure 5.12, a fracture energy vs. density plot is visualized, with color coding for each stick (for clarification, see Figure 5.8). Note that both stable and unstable responses are shown as well as reference specimens and acetylated specimens. Despite different responses and shapes, the results from each plank show consistency. A slight increase in fracture energy with increased density can be seen, for both untreated and acetylated test specimens.

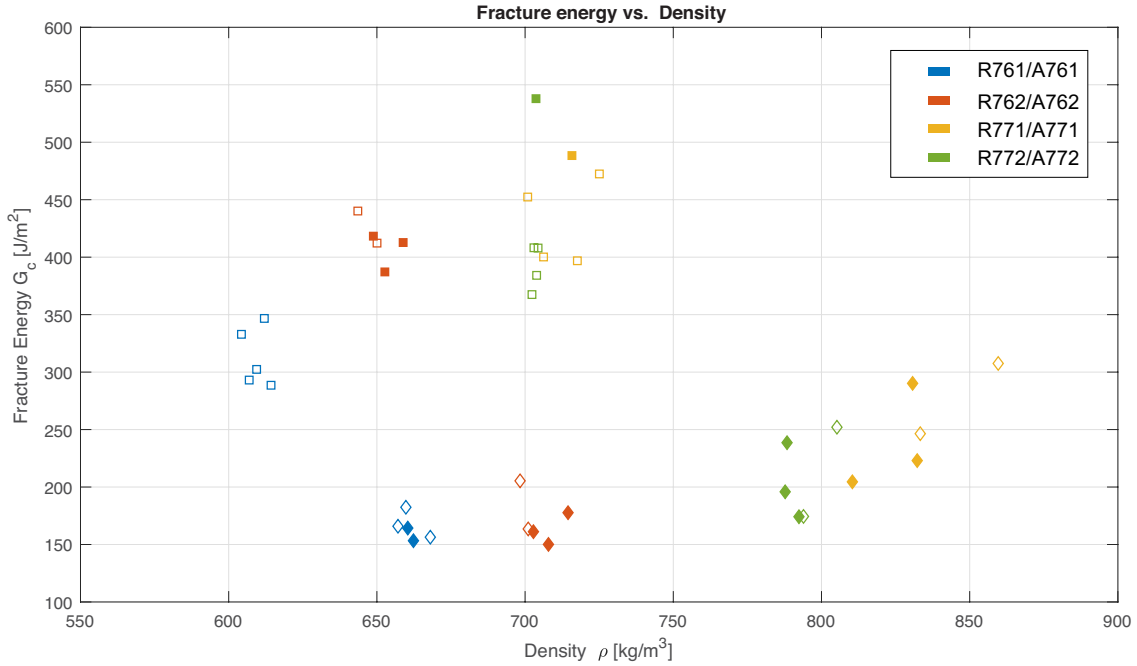

Figure 5.12: Fracture energy vs. density. Reference specimen shown as "□" and acetylated test specimen shown as "◊". The filled symbols represent stable responses while unfilled symbols represent unstable responses. Same color represent specimen extracted from the same stick.

6 Numerical analyses

The model was created and analyzed in the commercial FE-program Abaqus. First, a description of the important input parameters in Abaqus is given, together with a convergence study to determine a reasonable element size. The notch geometry, the viscosity coefficient and their impact on the results, are then stated. The stress distribution over the cross-section is also studied. Finally, the results from the analyses are presented together with a comparison to the experimental results and parameter studies.

6.1 Modeling test setup

In order to perform a finite element analysis of the test setup to compare with the experimental work, a model was created and analyzed using the FE-program Abaqus. Due to symmetry, only half of the test setup was modeled. As shown in Figure 6.1, the specimen was modeled as two separate solid parts; the lateral piece and half of the middle piece. The middle piece was modeled to have a rotated coordinate system to imitate the orientation of the actual test setup, with the longitudinal direction in the vertical direction instead of the horizontal, as shown in Figure 6.1. In the plane of symmetry, a solid rigid plate was modeled. Interaction properties were applied between the specimen and the rigid plate, to simulate a cohesive zone along a predefined crack path.

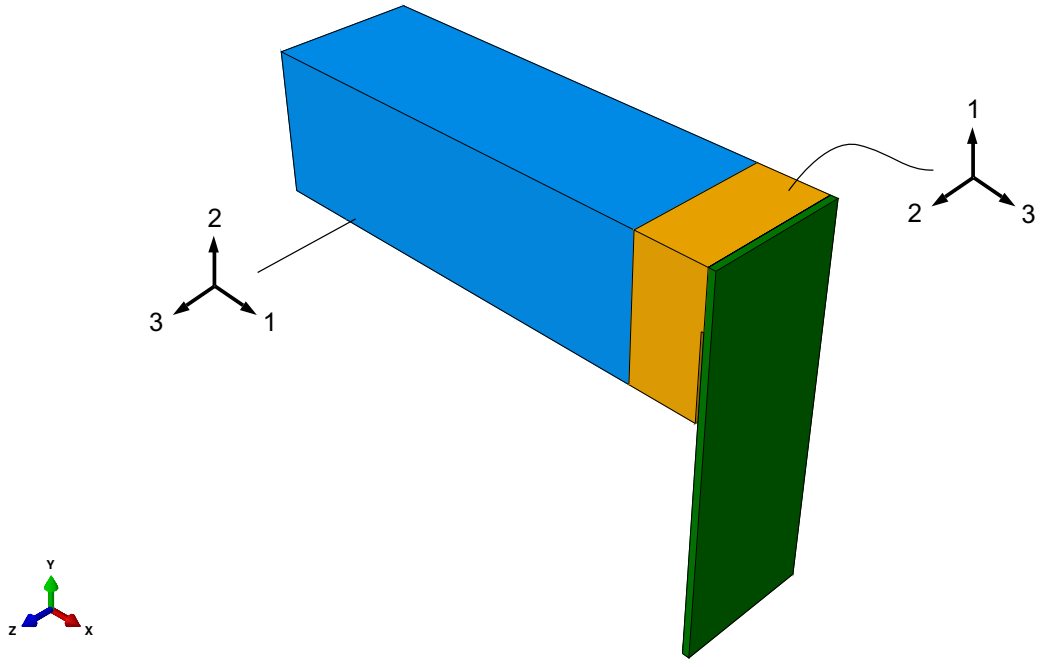

Figure 6.1: Model of the test setup in Abaqus, with the lateral piece (blue), half of the middle piece (orange) and the solid rigid plate (green).

6.1.1 Material parameters

The stiffness properties that were used as input data for the model are stated in Table 6.1, where directions 1, 2 and 3 represent the longitudinal, radial and tangential directions respectively. As seen in Table 6.1, the highest value of Young's modulus is in the longitudinal direction and the lowest is in the tangential direction.

Table 6.1: Input data for Young's modulus E, Poisson's ratio ν and shear modulus G for birch at a moisture content of 9 %.[10]

E_1 [MPa]	E_2 [MPa]	E_3 [MPa]	ν_{12} [-]	ν_{13} [-]	ν_{23} [-]	G_{12} [MPa]	G_{13} [MPa]	G_{23} [MPa]
16300	1110	620	0.034	0.018	0.78	1180	910	190

6.1.2 Constraints and interaction properties

In Abaqus, the lateral piece and the middle piece were put in contact as a tied constraint. The lateral piece was put as the master surface and the middle piece as the slave surface. The master surface is given to the piece with the higher stiffness, in this case the lateral piece. When using a tied constraint, the nodes of the slave surface are forced to follow the master surface and the tied parts move as one.

Interaction properties were set in the symmetry plane in order to permit the nodes to separate. The symmetry plane is the surface where the middle piece and the surface of the rigid plate is in contact. The symmetry plane was in Abaqus modeled with three different types of mechanical behavior; normal-, cohesive- and damage behavior.

A surface-based cohesive behavior (see section 4.5) was implemented to allow the two surfaces in the symmetry plane to initially be in contact during the analysis before the bond between them subsequently may damage and fail. An uncoupled traction-separation behavior was used, meaning that the normal and tangential stiffness components are uncoupled and that pure normal separation does not give rise to cohesive forces in the shear directions. The stiffness in the normal direction, K_{nn} is set to a high value while the stiffness in the shear directions, K_{ss} and K_{tt}, are set to a low stiffness value. In the symmetry plane, no shear stress will occur and therefore the values of K_{ss} and K_{tt} will not affect the results.

Table 6.2: Input data for cohesive behavior.

K_{nn} [N/m^3]	K_{ss} [N/m^3]	K_{tt} [N/m^3]
$5 \cdot 10^{11}$	1	1

Damage behavior (see section 4.5.2), allows specification of relevant data such as initiation, evolution and stabilization of damage. The damage modeling that follows allows a simulation of degradation and failure of the bond between the surfaces. The damage initiation criterion was set to 7 MPa in the normal direction (see equation 4.20), which is the tensile strength perpendicular to grain for birch, specified at a moisture

content of 12 % [31]. Shear directions are not of interest when regarding a loading situation giving pure Mode I loading, which is the case for the considered application, and therefore these were set to the low values of 1 Pa. When the initiation criterion is reached, the stiffness degradation follows a damage evolution law based on the energy dissipated from the damage process, i.e. the fracture energy, G_f. The fracture energy is equal to the area under the traction-separation curve in the local stress vs. deformation response (see subsection 4.5.3). The softening behavior was set to a linear softening.

As regards damage stabilization, no convergence problems were discovered when the viscosity coefficient was set to zero. In section 6.4, the viscosity coefficient is further discussed.

The input damage parameters used for untreated birch are shown in Table 6.3 and the input parameters for the acetylated birch in Table 6.4. Since only one symmetric half of the test setup was modeled, the input value of the fracture energy was set to half of the mean value of the fracture energy, obtained from the experimental analysis. The value of the fracture energy includes the dead weight of the specimen and therefore, the models are modelled without a value on the density. Generating a model without a weight to avoid adding the weight of the specimen twice.

Table 6.3: Cohesive- and damage parameters for untreated birch.

Initiation			Evolution
Normal only [Pa]	Shear 1 only [Pa]	Shear 2 only [Pa]	Energy [J/m^2]
$7 \cdot 10^6$	1	1	213.3

Table 6.4: Cohesive- and damage parameters for acetylated birch.

Initiation			Evolution
Normal only [Pa]	Shear 1 only [Pa]	Shear 2 only [Pa]	Energy [J/m^2]
$7 \cdot 10^6$	1	1	96.6

In Figure 6.2, a schematic illustration of the traction-separation curve for the local response is shown. Since the considered load case only creates normal stresses in the symmetry plane, shear components are not shown in the figure.

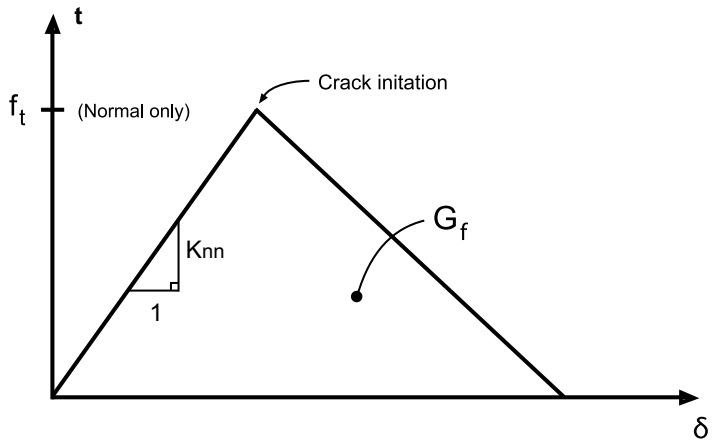

Figure 6.2: The traction-separation curve for the local response. Tensile strength f_t in normal direction, the fracture energy G_f and K_{nn} are presented in Table 6.2, Table 6.3 and Table 6.4. Modified after [20].

6.1.3 Mesh

The element size used in the model was decided based on the convergence study described in section 6.2. The outcome from the convergence study generated an element size of 1 mm for the middle piece and 2 mm for the lateral piece. The rigid plate did not need to be meshed more than necessary since its only functionality was to have corresponding elements for the cohesive interaction.

In Figure 6.3, the element types for both parts are visualized and the background within the FE-method for both element types were described in subsection 4.4. The lateral piece has a rectangular shape and was modeled with hexahedral element types, called C3D8R in Abaqus, and has the form of cuboids. The middle piece with the triangular shaped geometry was modeled with tetrahedral elements called C3D10.

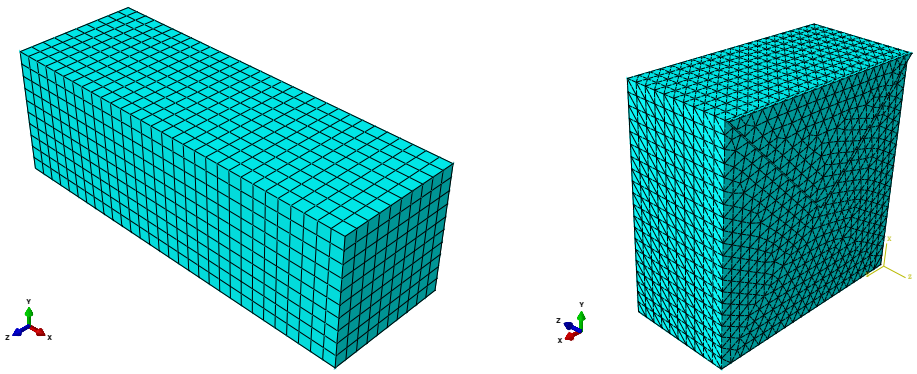

Figure 6.3: Lateral piece with hexahedral type elements and the middle piece with tetrahedral type elements.

6.1.4 Boundary conditions

The support with prescribed movements in the y- and z-axis was placed along a straight line 10 mm from the edge as visualized in Figure 6.4. Rotations about the x-axis and

y-axis are not prescribed but due to symmetry in both the test setup and in the prescribed displacement at mid-span, no rotations in other directions than around the z-axis occurs. In Figure 6.5, the prescribed surface for the rigid plate is visualized. Movements in the x- and z-axis are prescribed while rotation about x-, y- and z-axis are prescribed. Figure 6.6 shows the displacement load placed along a straight line and modeled as a boundary condition in the y-direction. The displacement load is set to 5 mm and placed at the top edge of the symmetry cut.

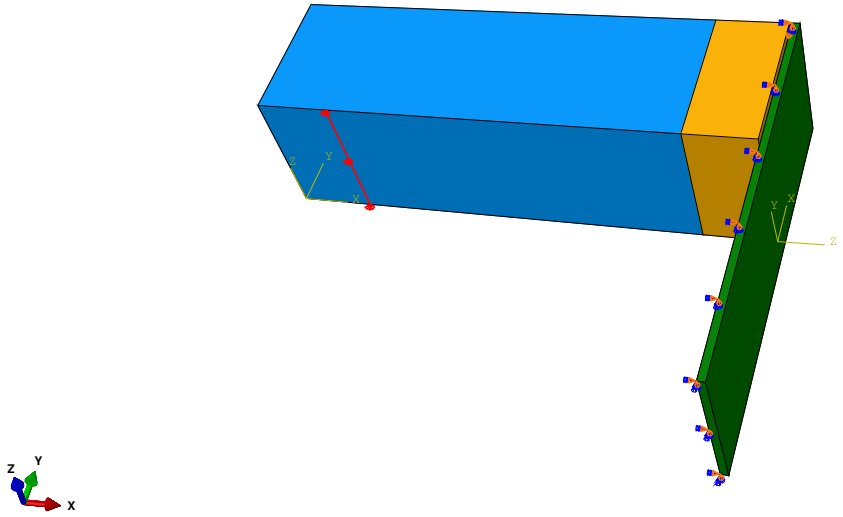

Figure 6.4: The placement of support, showed as a red line.

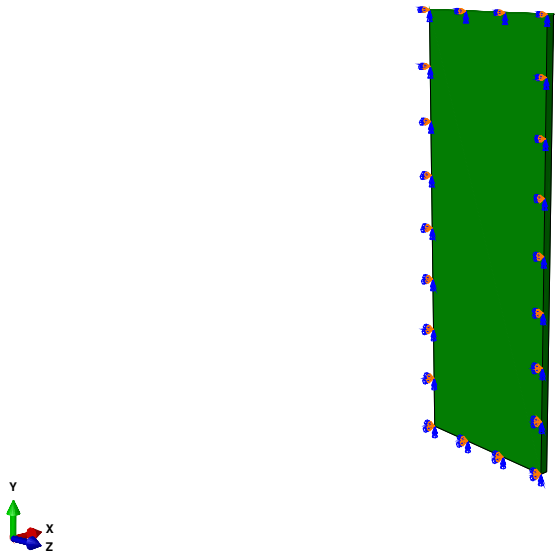

Figure 6.5: The prescribed surface for the rigid plate.

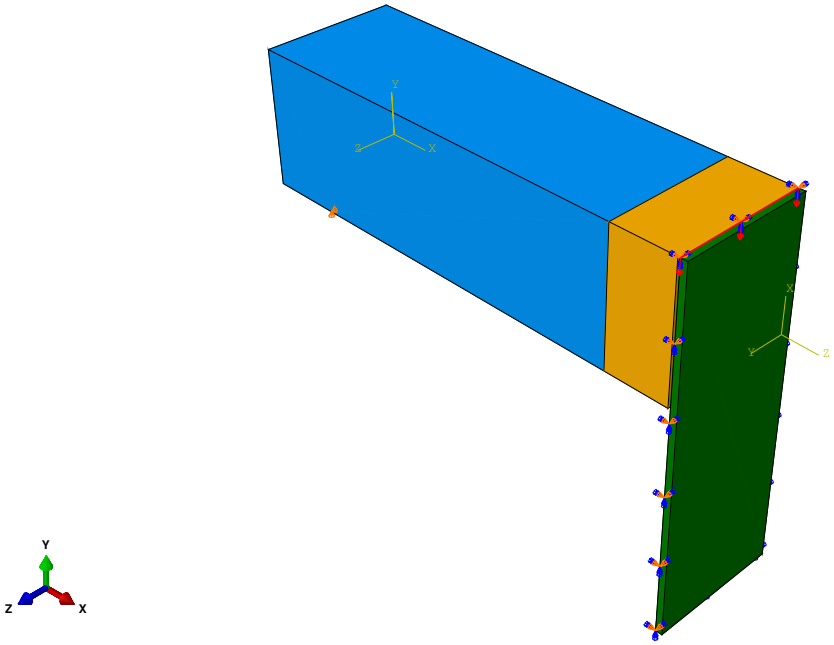

Figure 6.6: The placement of the load shown as a red line.

6.2 Element size and convergence study

The aim of a convergence study is to find a balance between result accuracy and the running time on the computer. A finer mesh with smaller element sizes typically results in a more accurate solution but with the drawback of an increased running time.

A convergence study is made by creating a mesh with a reasonable small number of elements before analyzing the results in detail. The model is then regenerated with larger number of elements, re-analyzed and then compared with the previous model with the smaller number of elements. The number of elements are then further increased until a satisfactorily result is achieved [4]. The satisfactorily results in this case will be when the difference in result between two mesh refinements is relatively small compared to the difference in running time.

The convergence study was made using an iterative method by halving the element sizes until the solution converged and a satisfactorily result was achieved. A convergence study was made for both the lateral piece and the middle piece, separately. The result is based on how the element size affects the difference in maximum load and fracture energy, between two mesh refinements. The element sizes used for the convergence study for the lateral piece were 4, 2 and 1 mm. The element sizes used for the middle piece were 4, 2, 1 and 0.5 mm. When performing the convergence study for the lateral piece, the element size was changed for the lateral piece while the other part had constant element size, and on the contrary when analyzing the middle piece.

In Table 6.5, input parameters for the lateral piece when performing a convergence study are presented. As seen in Table 6.6 and in Figure 6.7, a decrease of element size from 2 to 1 mm only had a difference of 0.034 % in maximum load, and the difference in running time was relatively small. The difference in fracture energy between changes of element size was also relatively small as shown in Table 6.6 and Figure 6.8.

Table 6.5: Element size, number of element nodes and run time for convergence study of the lateral piece.

Element size [mm]		Number of element nodes		Total number of element nodes*	Run time (hh:mm:ss)
Lateral piece	Middle piece	Lateral piece	Middle piece		
4	2	576	6153	7367	00:03:04
2	2	3751	6153	10542	00:04:30
1	2	26901	6153	33692	00:23:16

*includes 638 element nodes from the rigid plate.

Table 6.6: Results from the convergence study for the lateral piece.

Element size [mm]	Change in maximum load between curves	Change in G_f between curves
4 to 2	0.044%	0.023%
2 to 1	0.034%	0.035%

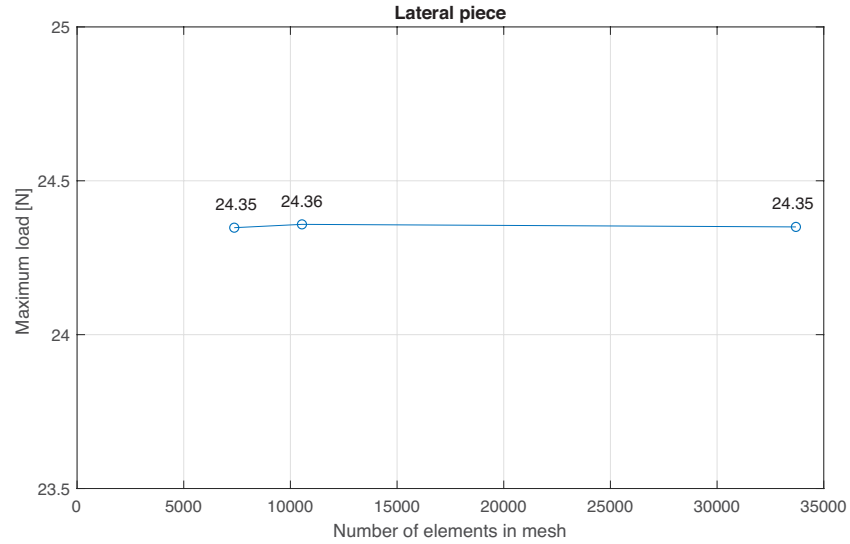

Figure 6.7: Plot of maximum load vs. the number of element nodes in the model for convergence study of the lateral piece.

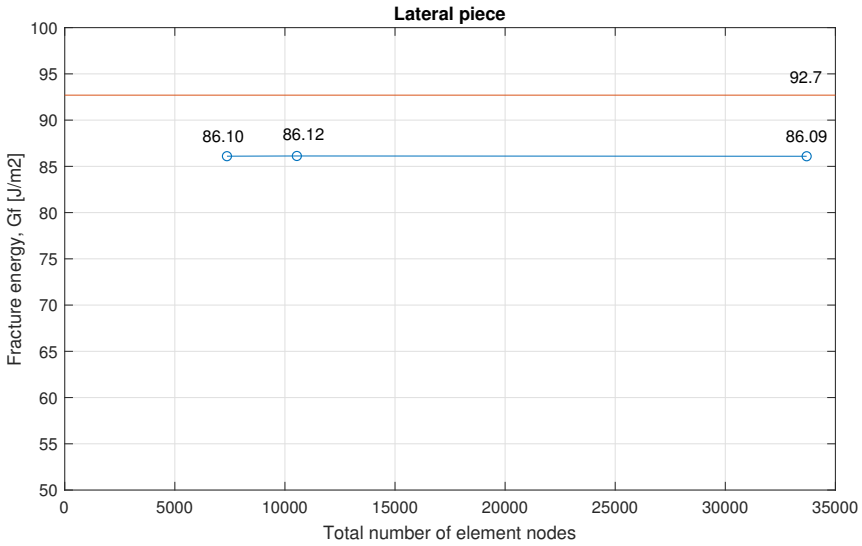

Figure 6.8: Plot of fracture energy vs. the number of element nodes in the model for convergence study of the lateral piece. The straight line represents the input value of the fracture energy.

In Table 6.7, input parameters for the middle piece when performing a convergence study are presented. The convergence study for the middle piece showed greater changes in both maximum load and fracture energy compared to the lateral piece, as seen in Table 6.8, Figure 6.10 and Figure 6.11 . Due to that the running time, when element size changed from 1 to 0.5 mm increased by about 14 times, an element size of 1 mm was therefore accepted. In conclusion from the convergence study, an element size of 2 mm is used for the lateral piece and an element size of 1 mm is used for the middle piece.

Table 6.7: Element size, number of element nodes and run time for convergence study of the middle piece.

Element size [mm]		Number of element nodes		Total number of element nodes*	Run time (hh:mm:ss)
Lateral piece	Middle piece	Lateral piece	Middle piece		
4	4	576	944	2158	00:00:57
4	2	576	6153	7367	00:03:06
4	1	576	38620	39834	00:33:30
4	0.5	576	207165	208379	07:40:29

*includes 638 element nodes from the rigid plate.

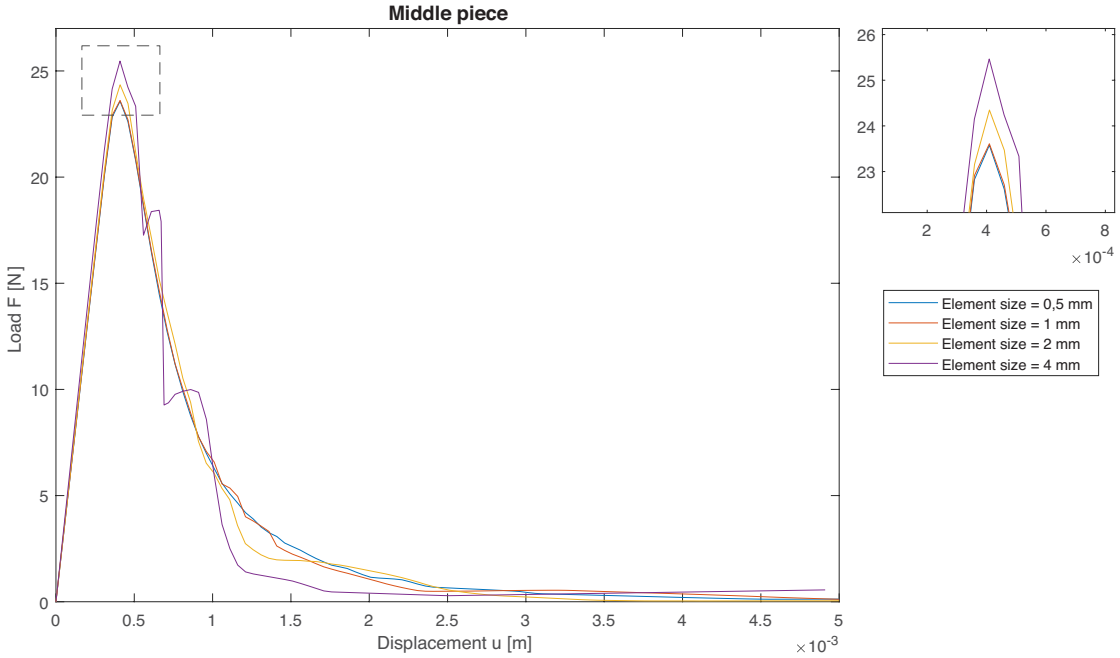

Figure 6.9: Load-displacement curves for different element sizes of the middle piece.

Table 6.8: Results from the convergence study for the middle piece.

Element size [mm]	Change in maximum load between curves	Change in G_f between curves
4 to 2	4.59 %	2.62 %
2 to 1	3.13 %	3.14 %
1 to 0.5	0.13 %	0.34 %

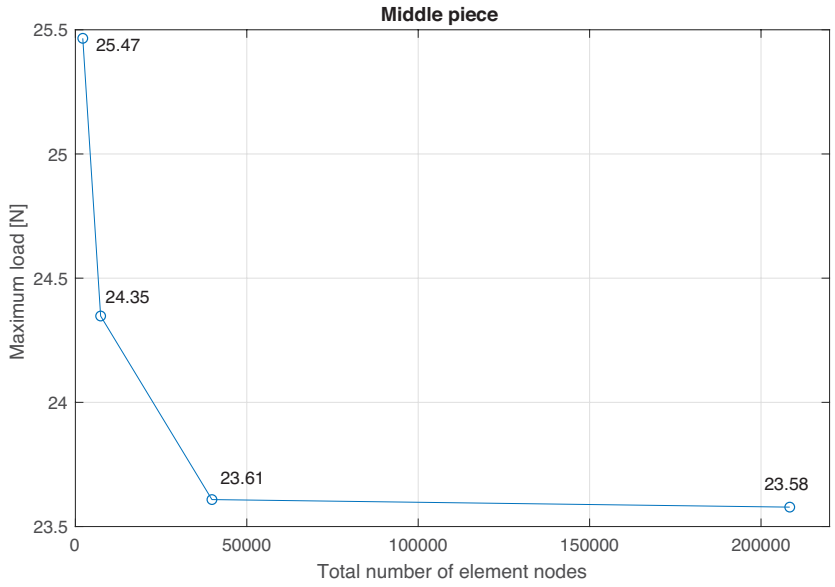

Figure 6.10: Plot of maximum load vs. the number of element nodes in the model for convergence study of the middle piece.

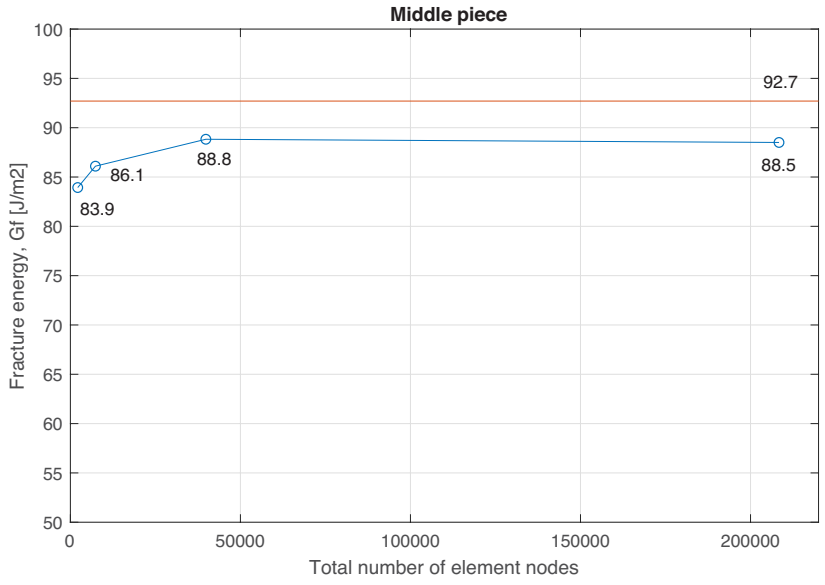

Figure 6.11: Plot of fracture energy vs. the number of element nodes in the model for convergence study of the middle piece. The straight line represents the input value of the fracture energy.

6.3 Notch geometry impact on results

After performing the first experiments with the reference specimens, unstable responses were obtained. Hence an investigation of how notch geometries impact the results, started. By changing the shape of the notch, the maximum load was affected. With increased maximum load, an increase in stored elastic energy is obtained. The increase in stored elastic energy could generate a more brittle response. Therefore, in order to

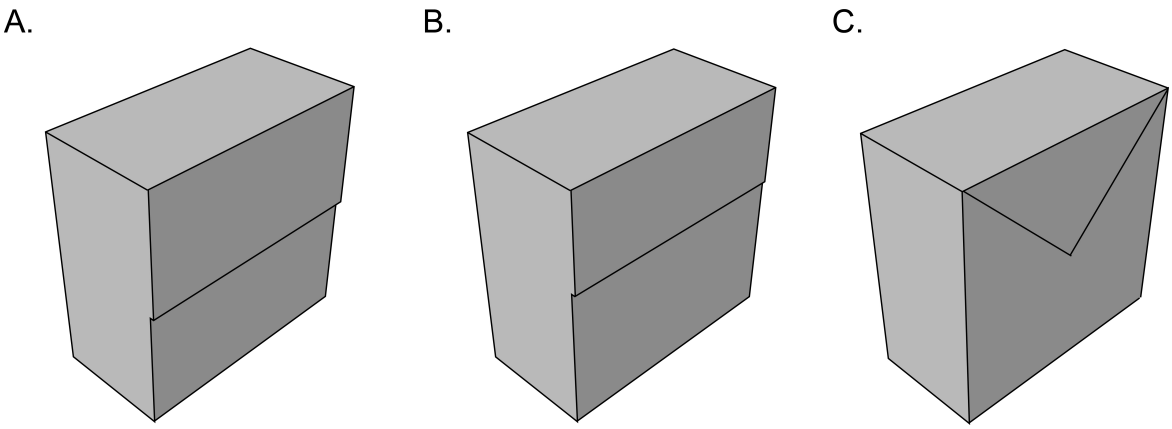

Figure 6.12: Different notch geometries: A. Rectangular shape, $h_c = 10\ mm$. B. Rectangular shape, $h_c = 8\ mm$. C. Triangular shape, $h_c = 10\ mm$.

lower the risk of achieving unstable responses and to be able to calculate the fracture energy, the maximum load was decreased by increasing the length of the notch, i.e. decrease the critical area, A_c.

Three different types of notch geometries were investigated using FE-analysis, as shown in Figure 6.12. First the rectangular test setup with a 10 mm notch was modeled, simply creating the model and calibrating it using experimental values of the fracture energy. Changing the rectangular notch from 10 mm to 12 mm still generated unstable responses, but when changed to a triangular shape, stable responses were achieved, as shown in Figure 6.13. The responses from rectangular shapes were interpreted as unstable. Hence triangular shapes were used in most experiments to increase the possibility of obtaining stable responses.

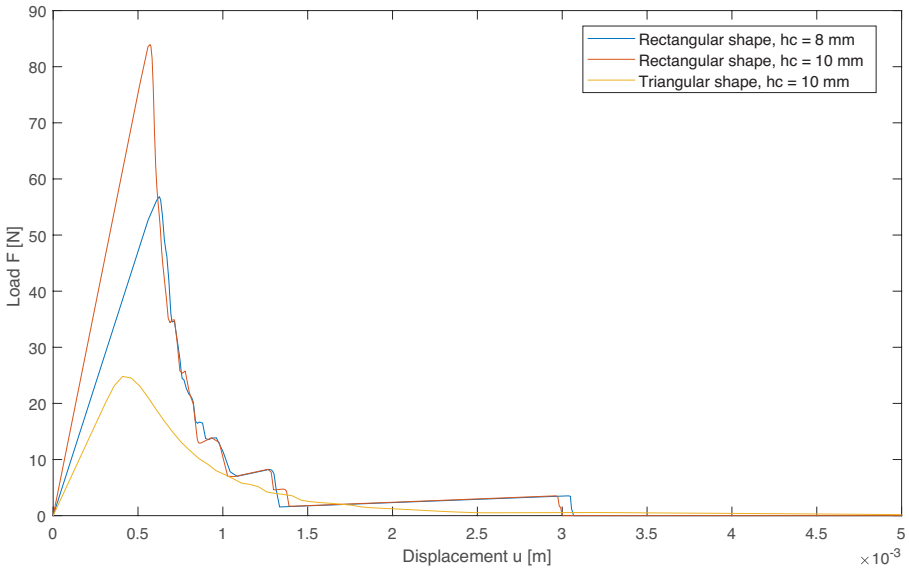

Figure 6.13: Load-displacement curve for the three different notch geometries. Cohesive properties according to Table 6.4, i.e. for acetylated birch.

6.4 Viscosity coefficient impact on results

As stated in subsection 4.5.4, to solve some of the convergence problems in Abaqus that often appear when including softening behavior, the viscous regularization can be used when modeling. However, the results may become inaccurate if used without caution. Therefore, a sensitivity analysis for this parameter was made in order to obtain proper results. Figure 6.14 illustrates how the viscosity coefficient for damage stabilization affects the results. The value used for the viscosity coefficient can, as visualized in Figure 6.14, affect the results to a great extent. For low values, the change in results are relatively small. In this dissertation the viscosity coefficient used was 0, since the model worked without experiencing convergence problems.

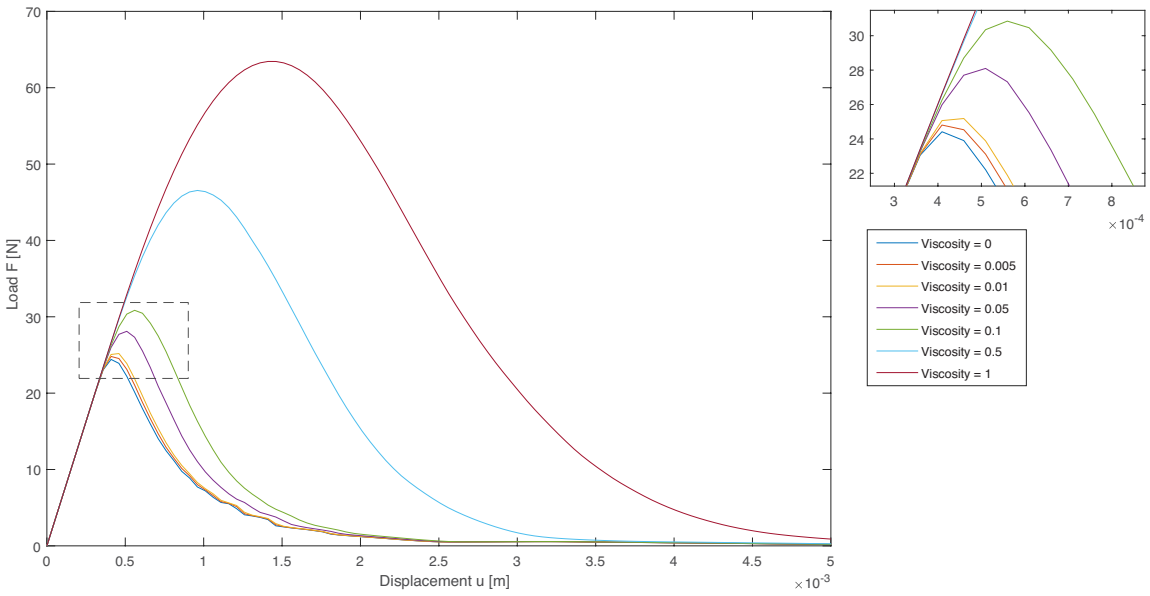

Figure 6.14: Load-displacement curve with different viscosity coefficients. Cohesive properties according to Table 6.4, i.e. for acetylated birch.

6.5 Stress distribution over cross section

In Figure 6.15, the stress distribution over the two different geometries are visualized, for a model with cohesive properties according to Table 6.4, i.e. for acetylated birch. The dotted lines illustrates where on the cross section the stress distributions shows. The time frame, shown in Figure 6.16 and Figure 6.17, illustrates at which time step the different stress distributions are taken from. Both geometries have similar shape on the stress distribution. After crack initiation, the peak load moves upwards and if following the peak, the fracture point in the material can be identified. Tension is at the bottom of the cross-section while compression is at the top of the cross-section. Note the difference in scale of the load axis in Figure 6.16 and Figure 6.17 between the two different geometries, where the rectangular geometry reaches a more than three times higher maximum load.

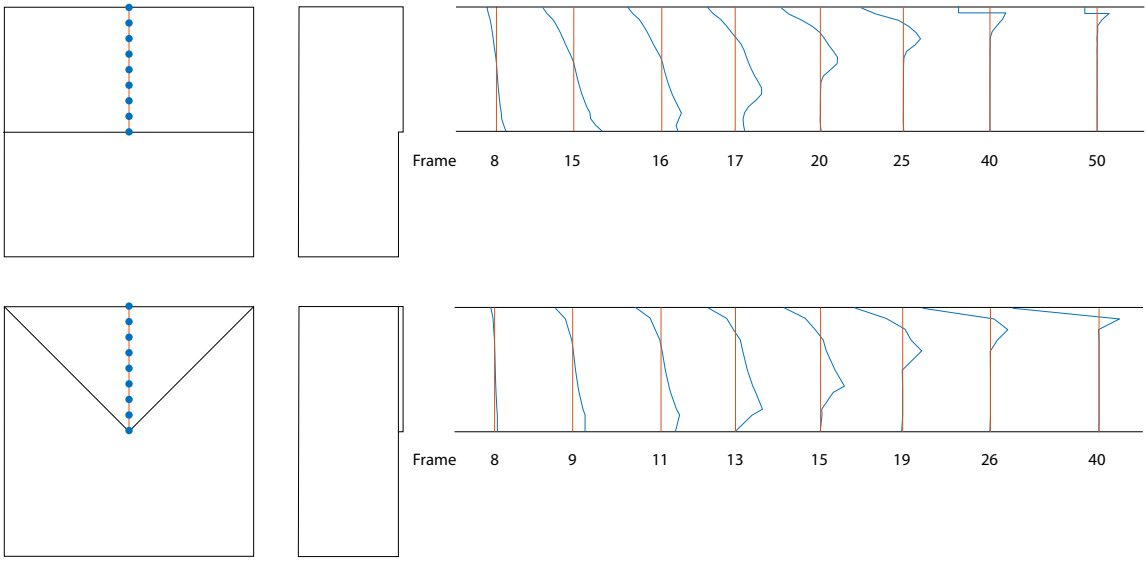

Figure 6.15: Stress distribution over the cross section with the two different notch geometries.

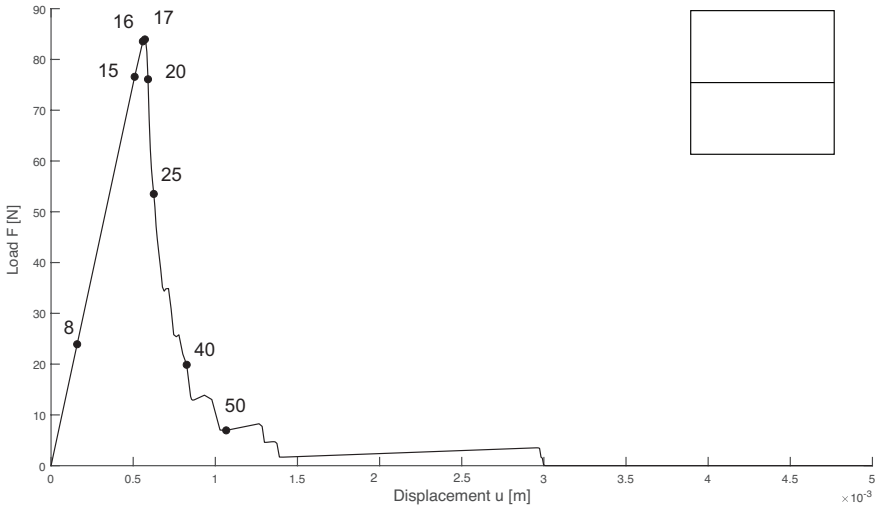

Figure 6.16: The time frames shown in Figure 6.15 and where they are taken from on load-displacement curve, for the rectangular notch geometry.

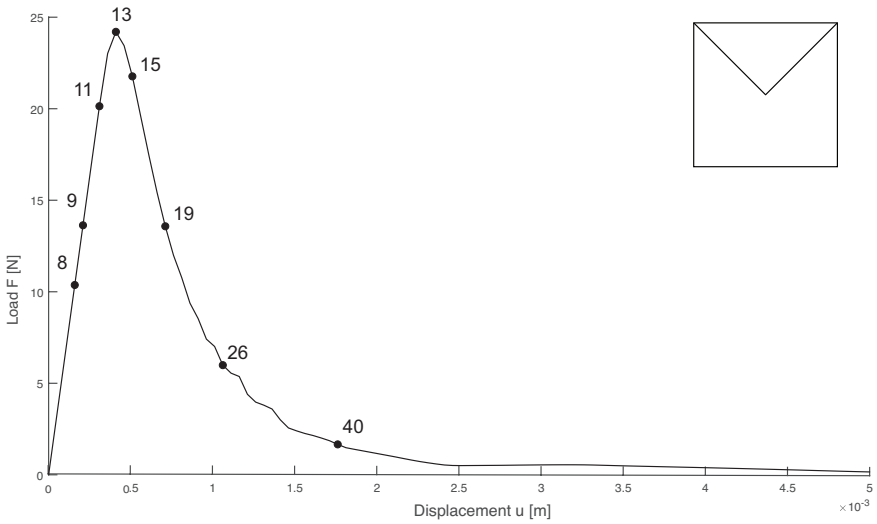

Figure 6.17: The time frames shown in Figure 6.15 and where they are taken from on load-displacement curve, for the triangular notch geometry.

6.6 Numerical modeling result

In Figure 6.18, load-displacement curves for the triangular notch geometry, for both reference and acetylated specimens are shown. The figure shows the modeling results from Abaqus when settings and input data from section 6.1 were used.

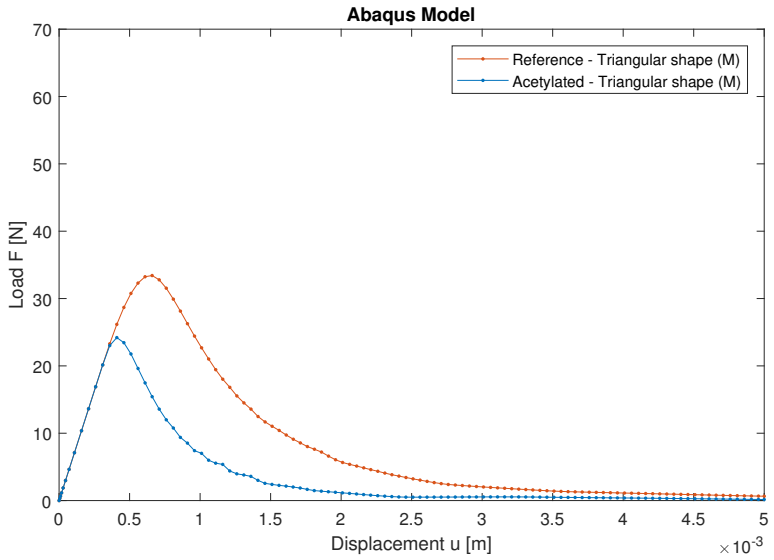

Figure 6.18: Load-displacement curve from Abaqus for reference and acetylated specimen with triangular notch geometry.

6.6.1 Comparison between experimental and numerical results

In the FE-model, mean values of the fracture energy achieved in the experimental work, are used as input values. The input value of fracture energy for the untreated birch was 213.3 J/m^2 and the output value from the Abaqus model was 205.6 J/m^2,

which is 3.7 % less. For the acetylated birch the input value was 96.9 J/m^2 and the output value from the Abaqus model was 92.7 J/m^2, which is 4.5 % less.

In Figure 6.19, a typical load-displacement curve from the experimental work of a reference specimen is illustrated with the corresponding numerical model, both with triangular notch geometry. A typical load-displacement curve in this case is a curve with maximum load closest to the mean value of the maximum load. The experimental work generated a mean value of the maximum load for the reference specimen of 39.5 N, while the model in Abaqus generated 33.4 N, which is 15 % less. The curves are fairly similar, with similar slopes for the linear part. The maximum load is higher for the experimental curve, and it has a steeper softening curve than the numerical model. Note that the curves from the experimental work in the figures only are typical responses, meaning curves with a maximum load value closest to the mean value of the maximum load.

In Figure 6.20, a typical load-displacement curve from the experimental work of an acetylated specimen is illustrated with its respective numerical model, both with triangular notch geometries. The experimental work generated a mean value of the maximum load for the acetylated specimen of 28.5 N, while the model in Abaqus generated 24.2 N, which is 15 % less. The curves are fairly similar for the acetylated specimen, where the inclination of the linear part is steeper for the experimental, indicating a higher Young's modulus in the tangential direction E_3 and/or in the longitudinal direction E_1, in the acetylated specimen than for the untreated. The maximum load is higher for the experimental, and it has a steeper softening than the numerical model.

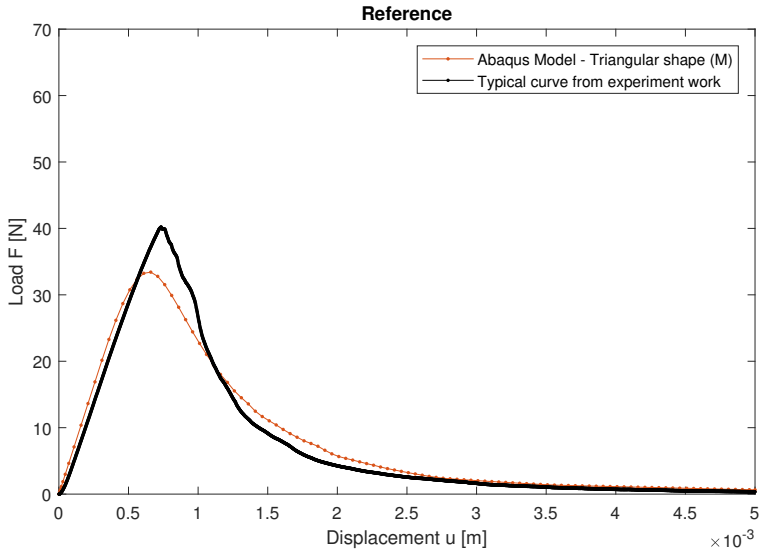

Figure 6.19: Load-displacement curve from model in Abaqus and typical load-displacement curve for a reference specimen from the experimental work, both with triangular notch geometry.

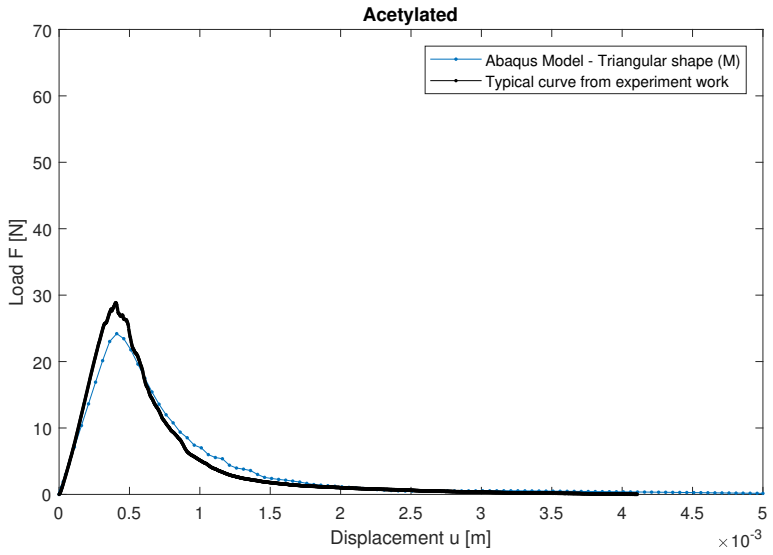

Figure 6.20: Load-displacement curve from model in Abaqus and typical load-displacement curve for an acetylated specimen from the experimental work, both with triangular notch geometry.

6.6.2 Parameter studies of the model

A parameter study is made by changing one parameter at a time and keeping the other parameters constant. The parameter studies involve investigating the fracture energy, G_f, the tensile strength, f_t, and Young's modulus in the tangential direction, E_3. Each parameter is investigated with both a 20 % increase and decrease. In Table 6.9, input values of the parameters are shown. The parameter study is made for the model with cohesive properties according to Table 6.4, i.e. for acetylated birch.

Table 6.9: Input data for the parameter study.

	Fracture energy, G_f [J/m^2]	**Tensile strength,** f_t [MPa]	**Young's modulus,** E_3 [MPa]
+20 %	116.3	8.4	744
+0 %	96.9	7.0	620
-20 %	77.5	5.6	496

In Figure 6.21, the parameter study for the fracture energy is shown. The inclination of the linear part is unchanged, but it reaches a higher maximum load with increased fracture energy. In Figure 6.22, the parameter study for the tensile strength is shown. Only a small change in maximum load can be visualized with increased/decreased tensile strength. In Figure 6.23, the parameter study for the Young's modulus in the tangential direction is shown. By increasing the value, a steeper inclination of the linear curve can be seen as well as a steeper softening curve. Because the fracture energy, or area underneath the curve, is unchanged, an increase in area somewhere has to be compensated by a decrease somewhere else.

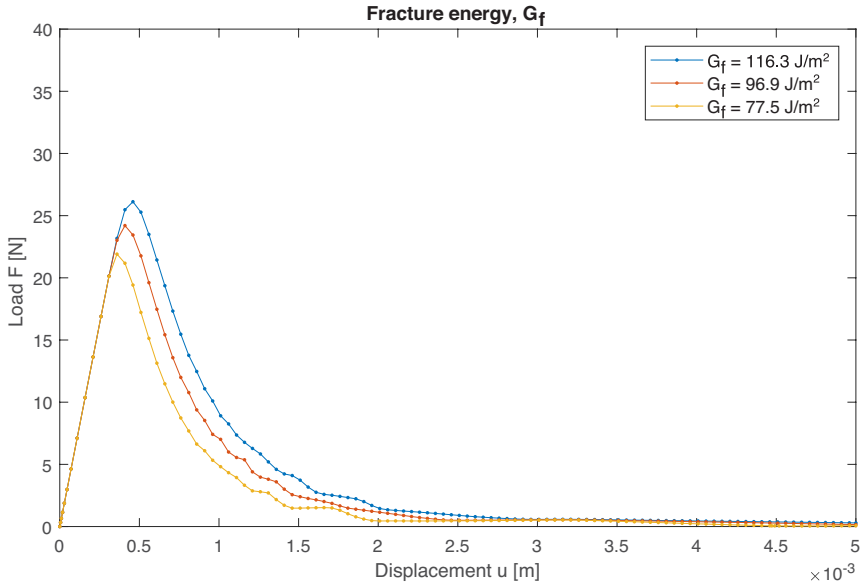

Figure 6.21: Parameter study of fracture energy, G_f.

Table 6.10: Result from the parameter study of fracture energy, G_f.

	Fracture energy, G_f [J/m^2]	**Max Load** [N]	**Change**
+20 %	116.3	26.1	+7.9 %
+0 %	96.9	24.2	+0 %
-20 %	77.5	21.9	-9.5 %

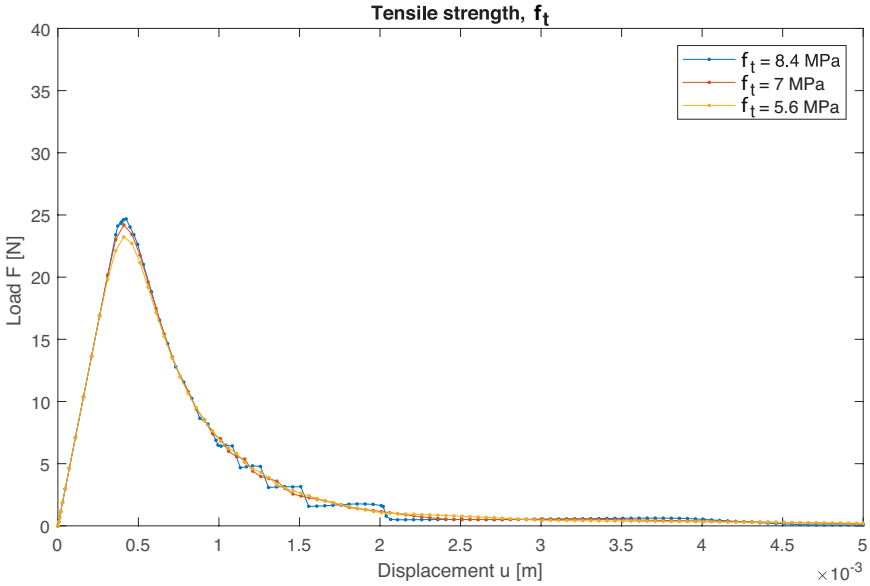

Figure 6.22: Parameter study of tensile strength, f_t.

Table 6.11: Result from the parameter study of tensile strength, f_t.

	Tensile strength, f_t [MPa]	**Max Load [N]**	**Change**
+20 %	8.4	24.7	+2.0 %
+0 %	7	24.2	+0 %
-20 %	5.6	23.2	-4.0 %

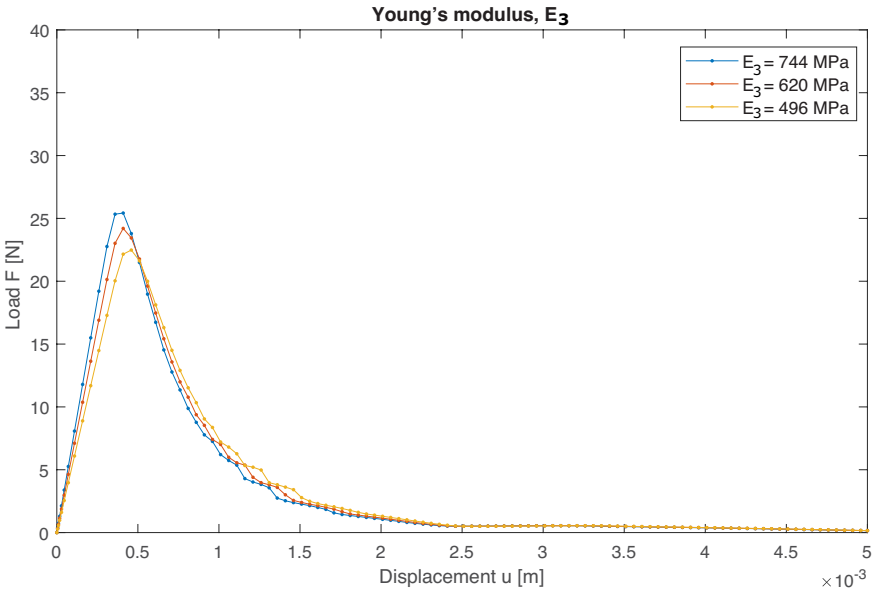

Figure 6.23: Parameter study of Young's modulus, E_3.

Table 6.12: Result from the parameter study of Young's modulus, E_3.

	Young's modulus, E_3 [MPa]	**Max Load [N]**	**Change**
+20 %	744	25.4	+5.1 %
+0 %	620	24.2	+0 %
-20 %	496	22.5	-7.1 %

7 Concluding remarks

7.1 Summary of results

Experimental work was performed in order to determine the fracture energy for both untreated and acetylated birch. The results from the experimental work showed a decrease of the mean value of the fracture energy, when comparing acetylated birch to untreated birch. The triangular shaped saw cut compared to the rectangular, reduced the mean value of the maximum load and generated more stable responses.

- The mean values of the fracture energy were 426.6 J/m^2 for untreated birch and 193.9 J/m^2 for acetylated birch. That equals a 55 % decrease of the mean value of the fracture energy for acetylated birch compared with untreated birch. Further, the mean value of the maximum load for acetylated birch decreased by about 28 % compared with the untreated birch.

- The acetylated specimens showed a 12 % higher mean value of the density than the untreated birch. The mean value of the moisture content was approximately 3 % for acetylated birch and approximately 11 % for untreated birch when conditioned in a climate of $20.2 \pm 0.2°C$ and a relative humidity of 63 ± 2 %.

- The experimental work generated a mean value of the maximum load of 28.5 N for acetylated specimens and 39.5 N for the untreated. The model in Abaqus generated 24.2 N for the acetylated specimen and 33.4 N for the untreated. Hence results from both models were 15 % less than the experimental results. Further, the value of the fracture energy was 4.5 % less for acetylated birch and 3.7 % less for untreated birch when comparing the results from the FE-analysis with the experimental results.

- The triangular notch geometry reduced the mean value of the maximum load by 60-65 % compared to the rectangular shape. The triangular shape generated more stable responses compared to the rectangular.

7.2 Discussion

The results from the experimental work shows a decreased, almost halved, fracture energy between the untreated and acetylated birch. The results also show a lower maximum load for acetylated test specimens. As described and visualized in section 6.6.2, a decrease in fracture energy when keeping other parameters constant, generates a lower maximum load. The only change between the input parameters in Abaqus between the untreated and acetylated birch, is the fracture energy. It could therefore be said that as a result of the decreased fracture energy, a decrease in the maximum load is obtained.

As mentioned earlier, the acetylation process used in this study was not customized for birch but for another wood species. When using a process not customized for a certain species, the result of the acetylation might lack in uniformity. This might cause internal stresses resulting in e.g. microcracking. Overall, this could lead to a reduction of fracture energy and strength. An optimized degree of acetylation for birch could therefore generate other, possibly improved, mechanical properties.

A decrease in moisture content in the acetylated birch was expected. The results shows that the modified birch was filled with the acetyl groups in the cell walls as intended, which reduces the birch's ability to absorb external water molecules that otherwise would have increased the moisture content. The modification process can likely be used to explain the increase of density in the acetylated birch, compared to the untreated birch. The value of the tensile strength used as input data when modeling, is based on birch with a moisture content of 12 %, while values of Young's modulus, E, Poisson's ratio, v, and shear modulus, G, are based on a moisture content of 9 %. The degree of moisture content is different in the test specimens, which might affect the results.

Both the model of the reference specimen and the model of the acetylated specimen had a mean value of the maximum load that were 15 % less than what the experimental test generated. The modulus of elasticity used in the model was the same for both the untreated and the acetylated birch. As shown in section 6.6.2, the initial (linear elastic) stiffness for the reference model is a fair approximation to the experimental work. The inclination for the model of the acetylated specimen, is lower than the experimental which can indicate a higher value of Young's modulus in the tangential direction, E_3. With both models having the same difference in maximum load, it could indicate that it is the same input parameter or a combination of parameters that generated the discrepancy. The references to the value of the tensile strength did not specify the quality of the timber. But as the sizes of the test specimens are small and knots and other defects in the wood were avoided, the wood could be assumed to be clear wood. Whereas the value used is a design value, i.e. a value including the possibility of defects in the wood. As shown in section 6.6.2, an increased value of the tensile strength alone does not have a major impact on the results, but might in combination with other parameters.

Different notch geometries could, according to our results, be a way to lower the maximum load and therefore decrease the stored elastic energy, which increases the

possibility for achieving stable responses. By halving the critical area, as is done with the triangular geometry, the maximum load was decreased by 60-65 %. The prescribed rectangular geometry in the Nordtest method should normally be enough to generate stable responses, but the tensile strength of birch is approximately twice as high as for spruce and pine, generating a higher maximum load in the test specimens than what the setup might be designed for to achieve stable responses. The amount of results and tests performed is too few to make an absolute conclusion, but the results can be seen as an indication.

There are various factors that could have affected the outcome of the experimental study. Some of the possible sources of errors could be human errors, e.g. when preparing test specimens which includes sawing, measuring and gluing. But also during the performance of the experimental tests where the placement of the test setup could differ between tests. The material is assumed to be clear wood and local defects were avoided, but weaknesses in the wood could however occur.

7.3 Suggestions for further research

Suggestions for future work concerning the investigation presented in the dissertation includes:

- The amount of stable responses from test specimens in this dissertation are not enough to present more than an indication of the outcome of both fracture energy and the impact of different notch geometries. A more profound study with a larger number of test specimens regarding both the fracture energy and the notch geometry should preferably be performed. It is also of interest to investigate whether rectangular and triangular notch geometries will generate similar fracture energies from stable responses.

- An interesting approach would have been to investigate the fracture energy and its value for stable and unstable responses, an analysis regarding if the unstable responses actually generates unreliable values. The values of the fracture energy in this dissertation have shown similar results for both stable and unstable responses.

- How the different shapes of the traction separation curve in the local response affects the global response, would add interesting knowledge. Investigate in what way linear and exponential softening affect the global results.

Bibliography

[1] A. Reiterer and G. Sinn. Fracture behaviour of modified spruce wood: A study using linear and non linear fracture mechanics. Holzforschung. 2002-01;56(2):191-198.

[2] Accoya. Acetylation: What it is and what is acetylated wood?. [Internet]. [Cited 2019-04-28]. Available from: https://www.accoya.com/blog/acetylation-what-is-it-and-and-what-is-acetylated-wood/.

[3] M. Ansell. *Wood Composites*. Elsevier Limited, 2015.

[4] Autodesk. How to perform a Mesh Convergence study. [Internet]. [Updated 2015-05-26; Cited 2019-03-18]. Available from: https://knowledge.autodesk.com/support/simulation-mechanical/learn-explore/caas/sfdcarticles/sfdcarticles/How-to-Perform-a-Mesh-Convergence-Study.html.

[5] H. J. Blaß and C. Sandhaas. *Timber engineering - Principles for Design*. Scientific Publishing, 2013.

[6] C. Hill. Acetylated wood, the science behind the material. [Internet]. Accoya: University of Wales, Bangor, School of the Environment and Natural Resources [Cited 2019-02-08]. Available from: https://www.accoya.com/wp-content/uploads/2013/09/\OT1\textquotedblleftAcetylated-Wood-The-Science-Behind-the-Material\OT1\textquotedblright-Callum-Hill-Acetylated-Wood-.pdf.

[7] D. Sandberg and A. Kutnar. Thermally modified timber: Recent developments in Europe and North America. Wood and fiber science: journal of the Society of Wood Science and Technology. 2016-02;48:28-39,.

[8] D. Smith. Understanding working with wood defects. [Internet]. Woodworking Network [Updated 2016-04-04; [Cited 2019-03-25]. Available from: https://www.woodworkingnetwork.com/best-practices-guide/solid-wood-machining/understanding-working-wood-defects.

[9] H. Danielsson. *Perpendicular to grain fracture analysis of wooden structural elements Models and Applications*. Lund University, Division of Structural Mechanics, Lund, Sweden. Report: TVSM-1024, 2013.

[10] J. Dinwoodie. *Timber: Its nature and behaviour*. E FN Spon, 2004.

[11] G. Mantanis. Chemical modification of wood by acetylation or furfurylation: A review of the present scaled-up technologies. [Internet]. Bioresources. 2017-04 [Cited 2019-03-22]. Available from: https://www.researchgate.net/publication/319927413_Chemical_Modification_of_Wood_by_Acetylation_or_Furfurylation_A_Review_of_the_Present_Scaled-up_Technologies DOI: 10.15376/biores.12.2.Mantanis.

[12] A. Hillerborg. *Materialbrott*. Lund University, Division of Building Materials, Lund, Sweden. Report: TVBM 3004, 1977.

[13] T. Isaksson, A. Mårtensson, and S. Thelandersson. *Byggkonstruktion*. Studentlitteratur, 2010.

[14] J. Morais, N. Dourado and M.F.S.F. deMoura. A numerical study on the SEN-TPB test applied to mode I wood fracture characterization. International Journal of Solids and Structures. 2011-02;48(2):234-242.

[15] R. Kregting. *Cohesive zone models- Towards a robust implementation of irreversible behaviour*. Eindhoven University of Technology, Materials Technology, Eindhoven, Netherlands. Report: MT05.11, 2005.

[16] Nordtest method. NT BUILD 422. Fracture energy in tension perpendicular to the grain, 1993.

[17] N. Ottosen and H. Petersson. *Introduction to the finite element method*. Pearson Education Limited, 1992.

[18] S. Morel, J. Morais, N. Dourado and M.F.S.F. deMoura. Wood fracture characterization under mode I loading using the three-point-bending test. Experimental investigation of Picea abies L. International Journal of Fracture. [Internet]. 2015-09 [Cited 2019-03-18]. Available from: `https://www.researchgate.net/publication/280021796_Wood_fracture_characterization_under_mode_I_loading_using_the_three-point-bending_test_Experimental_investigation_of_Picea_abies_L` DOI: 10.1007/s10704-015-0029-y.

[19] S. Stanzl-Tschegg, D. Keunecke and E. Tschegg. Fracture tolerance of reaction wood (yew and spruce wood in the TR crack propagation system). Journal of the Mechanical Behavior of Biomedical Materials. 2011-07;4(5):688-698.

[20] Sharcnet. Abaqus manual. [Internet]. [Cited 2019-03-22]. Available from: `https://www.sharcnet.ca/Software/Abaqus/6.14.2/v6.14/books/usb/default.htm?startat=pt01ch03s02abx11.html`.

[21] Skogssverige. Användning av olika träslag. [Internet]. [Updated 2016-10-12; Cited 2019-04-26]. Available from: `https://www.skogssverige.se/tra/fakta-om-tra/anvandning-av-olika-traslag`.

[22] Swedish Standards Institute. SS-EN 13183-1. Moisture content of a piece of sawn timber – part 1: Determination by oven dry method. European committee for standardisation, 2003.

[23] Swedish wood. Cellstruktur. [Internet]. [Cited 2019-02-12]. Available from: `https://www.traguiden.se/om-tra/materialet-tra/traets-uppbyggnad/traets-uppbyggnad/cellstruktur/`.

[24] Swedish wood. Choosing wood. [Internet]. [Cited 2019-02-01]. Available from: `https://www.swedishwood.com/about_wood/choosing-wood/`.

[25] Swedish wood. Modifiering. [Internet]. [Cited 2019-02-12]. Available from: https://www.traguiden.se/om-tra/materialet-tra/kemisk-behandling/kemisk-behandling/modifiering/.

[26] Swedish wood. Moisture content. [Internet]. [Cited 2019-03-21]. Available from: https://www.swedishwood.com/about_wood/choosing-wood/wood-and-moisture/.

[27] Swedish wood. Moisture-related wood movement. [Internet]. [Cited 2019-03-22]. Available from: https://www.swedishwood.com/about_wood/choosing-wood/wood-and-moisture/moisture-related-wood-movement/.

[28] Swedish wood. Properties of softwood. [Internet]. [Cited 2019-02-01]. Available from: https://www.swedishwood.com/about_wood/choosing-wood/from-log-to-plank/properties-of-softwood/.

[29] Swedish wood. The forest and sustainable forestry. [Internet]. [Cited 2019-02-04]. Available from: https://www.swedishwood.com/about_wood/choosing-wood/wood-and-the-environment/the-forest-and-sustainable-forestry/.

[30] SwedishWood. *Design of timber structures - Structural aspects of timber construction*. Swedish Forest Industries Federation - Swedish Wood, 2016.

[31] Träcentrum. Björk - Glasbjörk. [Internet]. [Cited 2019-03-18]. Available from: http://www.tracentrum.se/sv/publikationer/traslagsinformation/bjork/glasbjork/.

[32] Träguiden. Urtag i balkände. [Internet]. [Updated 2017-01-17; Cited 2019-05-22]. Available from: https://www.traguiden.se/konstruktion/limtrakonstruktioner/projektering-av-limtrakonstruktioner/hal-och-urtag/urtag-i-balkande/urtag-i-balkande/.

[33] H. Wernersson. *Fracture Characterization of Wood Adhesive Joints*. Lund University, Division of Structural Mechanics, Lund, Sweden. Report: TVSM-2012, 1994.

[34] L.-O. Ödlund. *Why isn't more birch wood being sawn in Sweden?* Växjö University, School of Technology and Design, Växjö, Sweden. Report: TD-123, 2009.

Appendix A
Test specimen data

A.1 Test specimen dimensions

[mm]

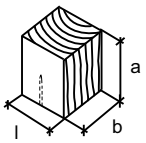

Table A.1: Table of dimensions for reference specimens.

Reference					
Specimen ID	**Weight** [g]	**l** [mm]	**b** [mm]	**a** [mm]	**Volume** [mm^3]
R7611	5.246	20.72	20.69	20.25	8681.11
R7612	5.196	20.72	20.68	19.98	8561.22
R7613	5.346	20.70	20.68	20.33	8702.79
R7614	5.342	20.70	20.69	20.38	8728.41
R7615	5.254	20.70	20.70	20.12	8621.22
R761RH	5.265	20.71	20.70	20.20	8659.68
R7621	5.520	20.69	20.66	19.60	8378.13
R7622	5.663	20.67	20.65	20.41	8711.71
R7623	5.636	20.66	20.64	20.25	8635.05
R7624	5.608	20.67	20.63	20.27	8643.58
R7625	5.535	20.69	20.65	20.13	8600.51
R762RH	5.590	20.63	20.67	20.21	8617.99
R7711	6.313	20.86	20.96	20.12	8796.98
R7712	6.241	20.85	20.94	19.97	8718.88
R7713	6.480	20.92	20.87	20.47	8937.21
R7714	6.321	20.93	20.86	20.50	8950.30
R7715	6.221	20.86	20.94	20.32	8875.95
R771RH	6.030	20.94	20.86	19.57	8548.34
R7721	6.236	21.03	21.07	19.98	8853.18
R7722	6.298	21.07	21.06	20.19	8958.99
R7723	6.236	21.06	21.07	20.01	8879.12
R7724	6.166	21.04	21.07	19.76	8759.86
R7725	6.205	21.04	21.05	19.91	8817.98
R772RH	6.183	21.10	21.09	19.87	8842.13

Table A.2: Table of dimensions for acetylated specimens.

Acetylated					
Specimen ID	**Weight** [g]	**l** [mm]	**b** [mm]	**a** [mm]	**Volume** [mm^3]
A7611	5.734	20.61	20.61	20.44	8682.34
A7612	5.680	20.62	20.64	20.15	8575.78
A7613	5.708	20.65	20.60	20.42	8686.46
A7614	5.745	20.67	20.65	20.40	8707.44
A7615	5.760	20.67	20.61	20.24	8622.42
A761RH	6.050	20.68	20.61	20.65	8801.34
A7621	5.894	20.62	20.53	19.86	8407.31
A7622	6.120	20.57	20.60	20.55	8707.90
A7623	6.131	20.60	20.62	20.39	8661.10
A7624	6.109	20.62	20.65	20.08	8550.12
A7625	5.950	20.62	20.63	20.03	8520.57
A762RH	5.982	20.66	20.63	19.91	8485.96
A7711	7.400	20.90	20.92	20.31	8880.10
A7712	7.213	21.08	20.94	19.67	8682.64
A7713	7.434	20.94	20.94	20.37	8931.91
A7714	7.157	20.93	20.94	20.15	8831.23
A7715	7.742	20.94	20.96	20.52	9006.28
A771RH	7.853	20.99	21.08	21.08	9327.25
A7721	6.828	20.80	20.83	19.85	8600.29
A7722	6.941	20.81	20.80	20.34	8804.13
A7723	6.969	20.82	20.85	20.26	8794.81
A7724	6.804	20.86	20.87	19.84	8637.31
A7725	7.169	20.84	20.84	20.50	8903.26
A772RH	7.055	20.85	20.87	19.97	8689.74

A.2 Density

Table A.3: Density of R761 and A761.

Reference		Acetylated	
Specimen ID	**Density** ρ [kg/m^3]	**Specimen ID**	**Density** ρ [kg/m^3]
R7611	604.30	A7611	660.42
R7612	606.92	A7612	662.33
R7613	614.29	A7613	657.11
R7614	612.02	A7614	659.78
R7615	609.43	A7615	668.03
R761RH	607.99	A761RH	687.40
Mean value:	609.16	Mean value:	665.84
Standard Deviation:	3.28	Standard Deviation:	10.20
Change:	665.84/609.16=1.093		

Table A.4: Density of R762 and A762.

Reference		Acetylated	
Specimen ID	**Density** ρ [kg/m^3]	**Specimen ID**	**Density** ρ [kg/m^3]
R7621	658.86	A7621	701.06
R7622	650.04	A7622	702.81
R7623	652.69	A7623	707.88
R7624	648.81	A7624	714.49
R7625	643.57	A7625	698.31
R762RH	648.64	A762RH	704.93
Mean value:	650.43	Mean value:	704.91
Standard Deviation:	4.64	Standard Deviation:	5.22
Change:	704.91/650.43=1.084		

Table A.5: Density of R771 and A771.

Reference		Acetylated	
Specimen ID	**Density** ρ [kg/m^3]	**Specimen ID**	**Density** ρ [kg/m^3]
R7711	717.63	A7711	833.32
R7712	715.80	A7712	830.74
R7713	725.06	A7713	832.30
R7714	706.23	A7714	810.42
R7715	700.88	A7715	859.62
R771RH	705.40	A771RH	841.94
Mean value:	711.84	Mean value:	834.72
Standard Deviation:	8.34	Standard Deviation:	14.64
Change:	834.72/711.84=1.173		

Table A.6: Density of R772 and A772.

Reference		Acetylated	
Specimen ID	**Density** ρ [kg/m^3]	**Specimen ID**	**Density** ρ [kg/m^3]
R7721	704.38	A7721	793.93
R7722	702.98	A7722	788.38
R7723	702.32	A7723	792.40
R7724	703.89	A7724	787.75
R7725	703.68	A7725	805.21
R772RH	699.27	A772RH	811.88
Mean value:	702.75	Mean value:	796.59
Standard Deviation:	1.69	Standard Deviation:	8.93
Change:	796.59/702.75=1.134		

A.3 Moisture content

Table A.7: Moisture content of reference test specimen.

Reference			
Specimen ID	**Weigth,** $w_{initial}$ [g]	**Weigth,** w_{dry} [g]	**Moisture content** [%]
R761RH	5.265	4.740	11.08
R762RH	5.590	5.037	10.98
R771RH	6.030	5.442	10.80
R772RH	6.183	5.571	10.99
		Mean value:	10.96
		Standard Deviation:	0.10

Table A.8: Moisture content of acetylated test specimen.

Acetylated			
Specimen ID	**Weigth,** $w_{initial}$ [g]	**Weigth,** w_{dry} [g]	**Moisture content** [%]
A761RH	6.050	5.881	2.87
A762RH	5.982	5.803	3.08
A771RH	7.853	7.613	3.15
A772RH	7.055	6.839	3.16
		Mean value:	3.07
		Standard Deviation:	0.12

Appendix B
Test results, fracture energy

B.1 Calculated fracture energy

Table B.1: Test results and calculated fracture energy, G_f, for reference test specimen.

Specimen ID	W [J]	m_{tot} [kg]	m_{prism} [kg]	m [kg]	u_0 [m]	h_c [m]	b_c [m]	Max Load [N]	G_f [J/m^2]	Notch geometry	Stable curve
R7611	0.0702	0.03678	0.002685	0.036018	0.006374	0.01052	0.02069	116.10	(332.87)	U	
R7612	0.0584	0.03645	0.002685	0.035747	0.006292	0.01000	0.02068	105.30	(293.07)	U	
R7613	0.0541	0.03752	0.002685	0.036635	0.007209	0.00950	0.02068	97.18	(288.56)	U	
R7614	0.0658	0.03693	0.002685	0.036143	0.007222	0.00953	0.02069	99.60	(346.70)	U	
R7615	0.0621	0.03636	0.002685	0.035673	0.006220	0.01027	0.02070	110.99	(302.35)	U	
R7621	0.0347	0.03820	0.002685	0.037206	0.007758	0.00971	0.01873	33.70	412.73	M	x
R7622	0.0369	0.03877	0.002685	0.037678	0.008180	0.00968	0.02001	40.21	(412.23)	M	
R7623	0.0371	0.03884	0.002685	0.037734	0.007631	0.01011	0.02040	36.88	387.16	M	x
R7624	0.0396	0.03884	0.002685	0.037733	0.007069	0.01032	0.01956	40.22	418.28	M	x
R7625	0.0880	0.03916	0.002685	0.038001	0.007504	0.00999	0.02065	116.58	(440.14)	U	
R7711	0.0350	0.04313	0.002685	0.041314	0.007975	0.00979	0.01968	42.65	(396.87)	M	
R7712	0.0459	0.04343	0.002685	0.041563	0.009739	0.01008	0.02026	47.05	488.40	M	x
R7713	0.0469	0.04363	0.002685	0.041725	0.005845	0.01016	0.02054	59.03	(472.41)	M	
R7714	0.0324	0.04313	0.002685	0.041308	0.006274	0.00944	0.01850	37.78	(400.16)	M	
R7715	0.0906	0.04357	0.002685	0.041677	0.008446	0.00993	0.02094	131.47	(452.32)	U	
R7721	0.0388	0.04359	0.002685	0.041698	0.008480	0.01004	0.02064	48.12	(407.95)	M	
R7722	0.0384	0.04327	0.002685	0.041428	0.007069	0.00986	0.02051	41.67	(408.18)	M	
R7723	0.0345	0.04332	0.002685	0.041473	0.007227	0.00996	0.02046	46.39	(367.46)	M	
R7724	0.0373	0.04309	0.002685	0.041278	0.007991	0.01037	0.02035	47.03	(384.17)	M	
R7725	0.1062	0.04326	0.002685	0.041423	0.009220	0.00971	0.02105	123.43	537.91	U	x

	Stable curve only	All
Mean value of G_f :	448.90	397.50
Standard Deviation:	55.75	62.97

Table B.2: Test results and calculated fracture energy, G_f, for acetylated test specimen.

Specimen ID	W [J]	m_{tot} [kg]	m_{prism} [kg]	m [kg]	u_0 [m]	h_c [m]	b_c [m]	Max Load [N]	G_f [J/m^2]	Notch geometry	Stable curve
A7611	0.0156	0.04017	0.002685	0.038843	0.004243	0.01017	0.02061	30.32	164.28	M	x
A7612	0.0150	0.03969	0.002685	0.038443	0.004520	0.01056	0.02064	20.16	153.28	M	x
A7613	0.0344	0.03927	0.002685	0.038091	0.004426	0.01055	0.02060	75.10	(165.90)	U	
A7614	0.0336	0.03968	0.002685	0.038435	0.005689	0.00949	0.02065	73.16	(182.40)	U	
A7615	0.0314	0.03962	0.002685	0.038388	0.003568	0.01016	0.02061	86.09	(156.37)	U	
A7621	0.0120	0.04147	0.002685	0.039925	0.004576	0.00906	0.01862	22.52	(163.51)	M	
A7622	0.0150	0.04206	0.002685	0.040419	0.004471	0.01025	0.02031	29.54	161.14	M	x
A7623	0.0137	0.04212	0.002685	0.040468	0.003696	0.01025	0.01972	26.49	150.07	M	x
A7624	0.0155	0.04186	0.002685	0.040250	0.004484	0.00973	0.01998	25.18	177.67	M	x
A7625	0.0375	0.04182	0.002685	0.040223	0.005898	0.00940	0.02063	74.06	(205.38)	U	
A7711	0.0221	0.05063	0.002685	0.047564	0.005210	0.00997	0.01997	32.42	(246.42)	M	
A7712	0.0264	0.05064	0.002685	0.047573	0.007016	0.01007	0.02031	32.98	290.18	M	x
A7713	0.0196	0.05112	0.002685	0.047973	0.004513	0.00985	0.01978	26.39	223.00	M	x
A7714	0.0179	0.05089	0.002685	0.047779	0.005200	0.00986	0.02017	29.23	204.52	M	x
A7715	0.0639	0.05076	0.002685	0.047670	0.005735	0.01033	0.02096	126.99	(307.51)	U	
A7721	0.0165	0.04758	0.002685	0.045023	0.003566	0.01013	0.02046	31.56	(174.42)	M	
A7722	0.0216	0.04970	0.002685	0.046789	0.005855	0.01002	0.02032	33.83	238.57	M	x
A7723	0.0161	0.04928	0.002685	0.046433	0.003826	0.01002	0.02045	30.13	174.15	M	x
A7724	0.0179	0.04789	0.002685	0.045275	0.004364	0.00997	0.02032	28.87	195.85	M	x
A7725	0.0491	0.04839	0.002685	0.045693	0.006236	0.00988	0.02084	104.64	(252.04)	U	

	Stable curve only	All
Mean value of G_f :	193.88	199.33
Standard Deviation:	40.90	45.07

B.2 Load-displacement curves

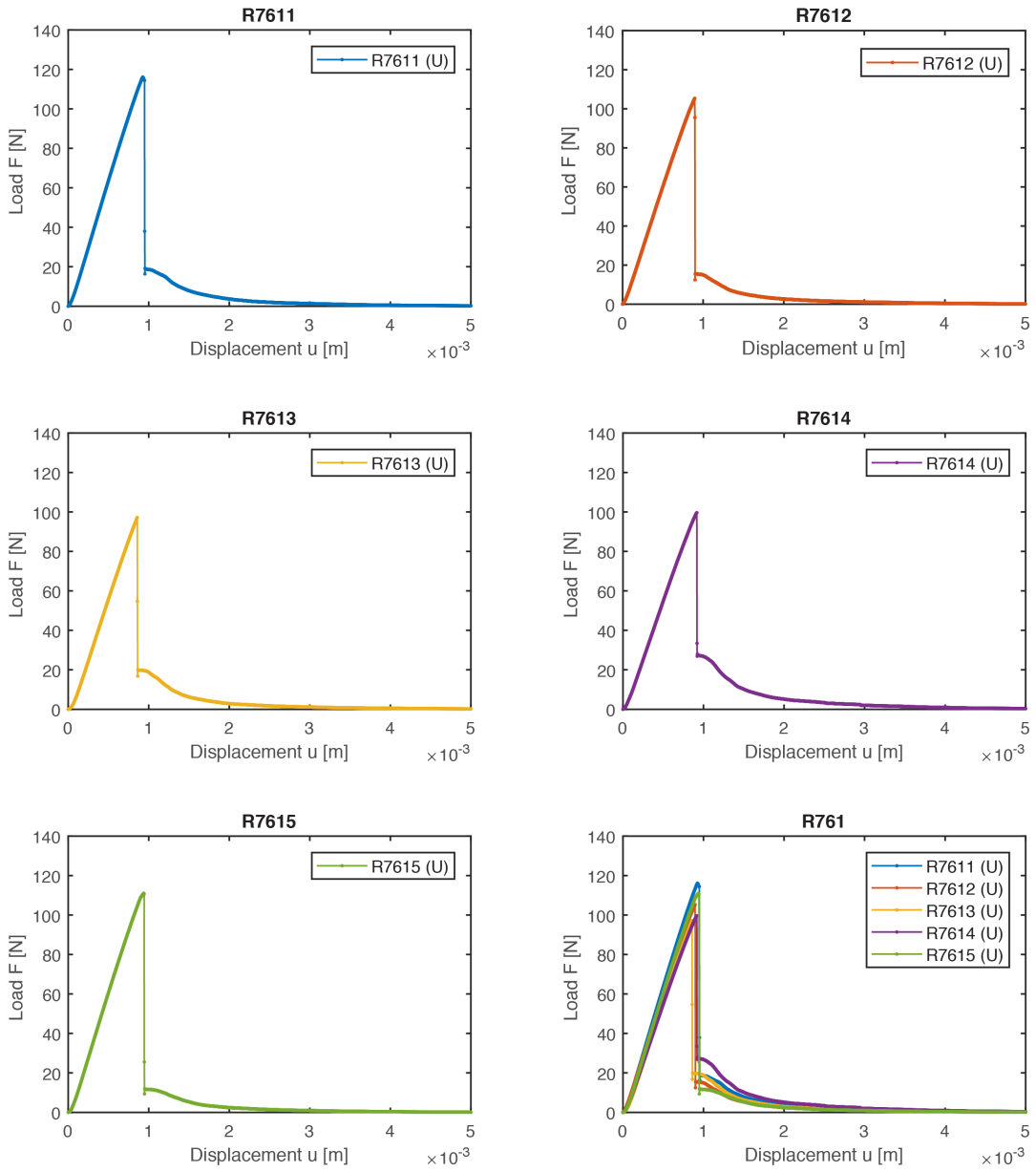

Figure B.1: Load-displacement curves of reference test specimens R7611-R7615 from plank 76.

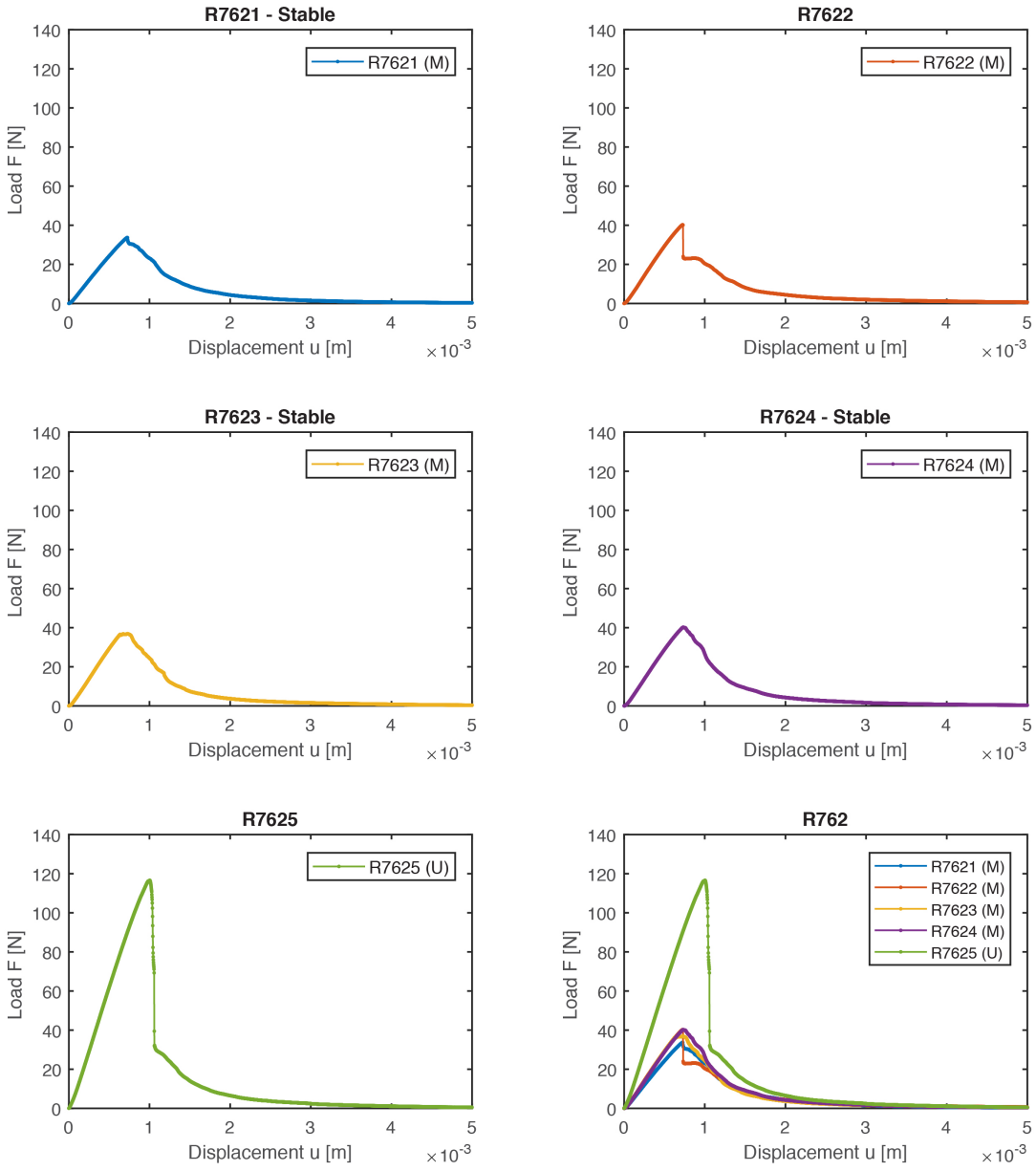

Figure B.2: Load-displacement curves of reference test specimens R7621-R7625 from plank 76.

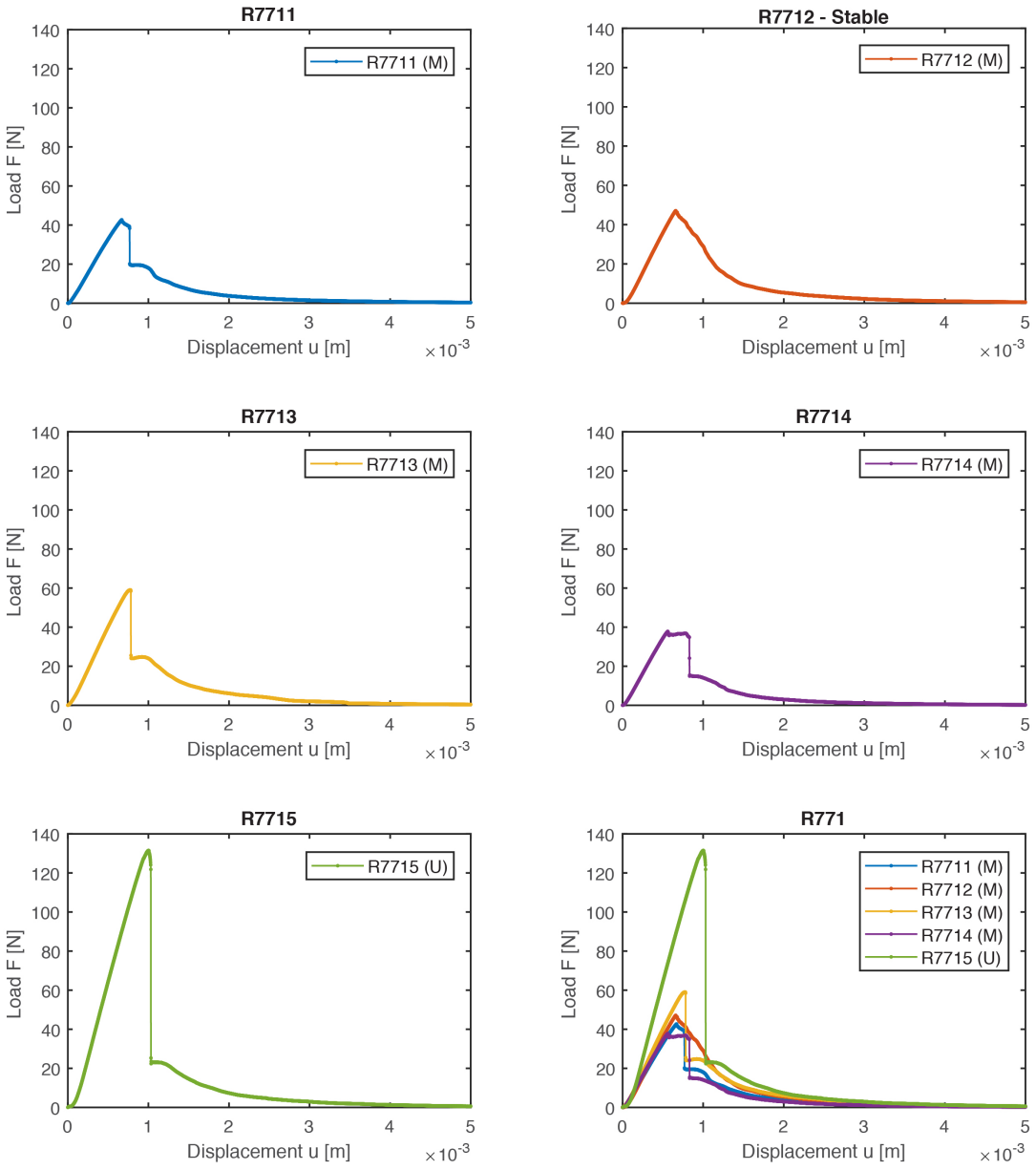

Figure B.3: Load-displacement curves of reference test specimens R7711-R7715 from plank 77.

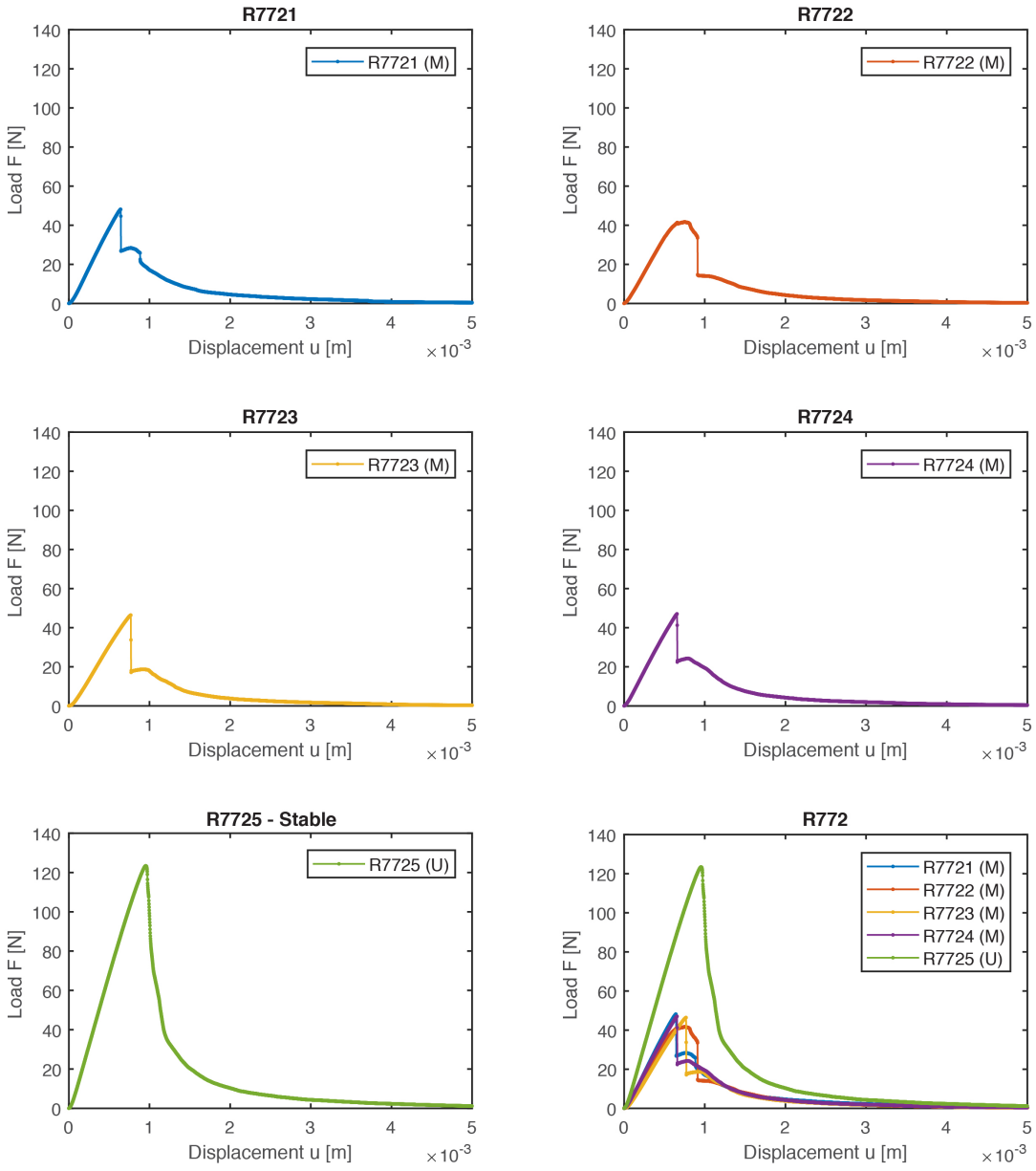

Figure B.4: Load-displacement curves of reference test specimens R7721-R7725 from plank 77.

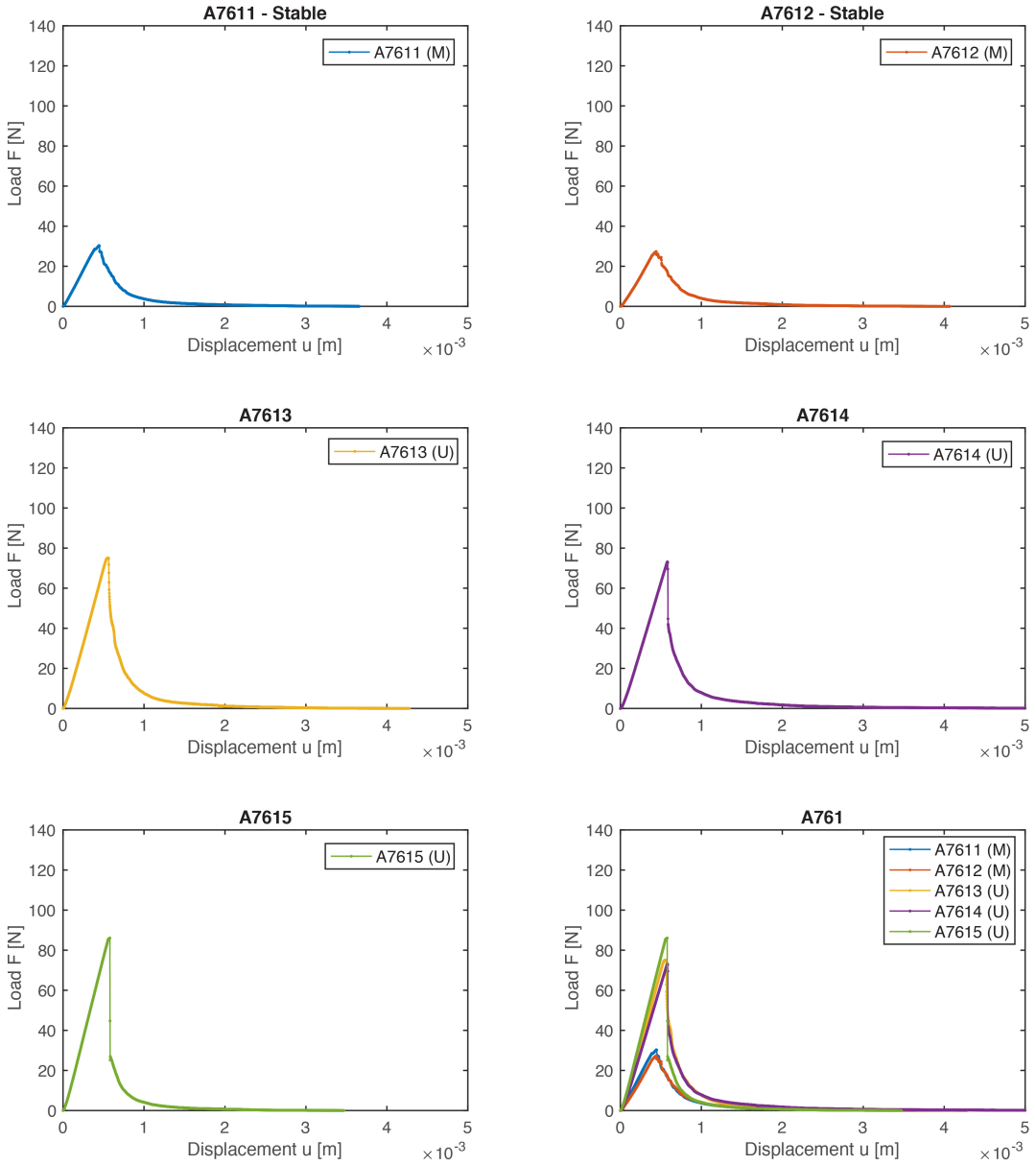

Figure B.5: Load-displacement curves of acetylated test specimens A7611-R7615 from plank 76.

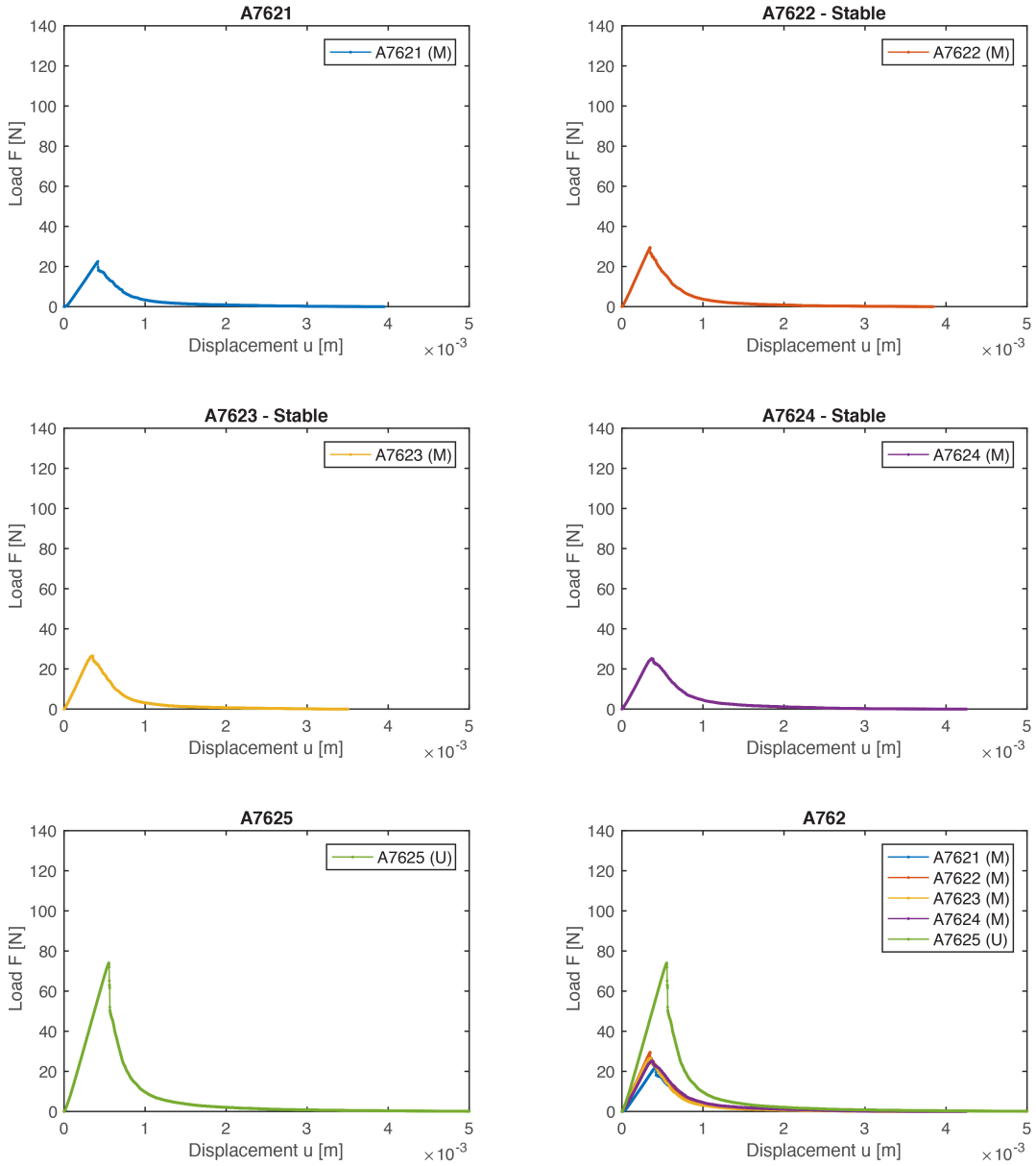

Figure B.6: Load-displacement curves of acetylated test specimens A7621-R7625 from plank 76.

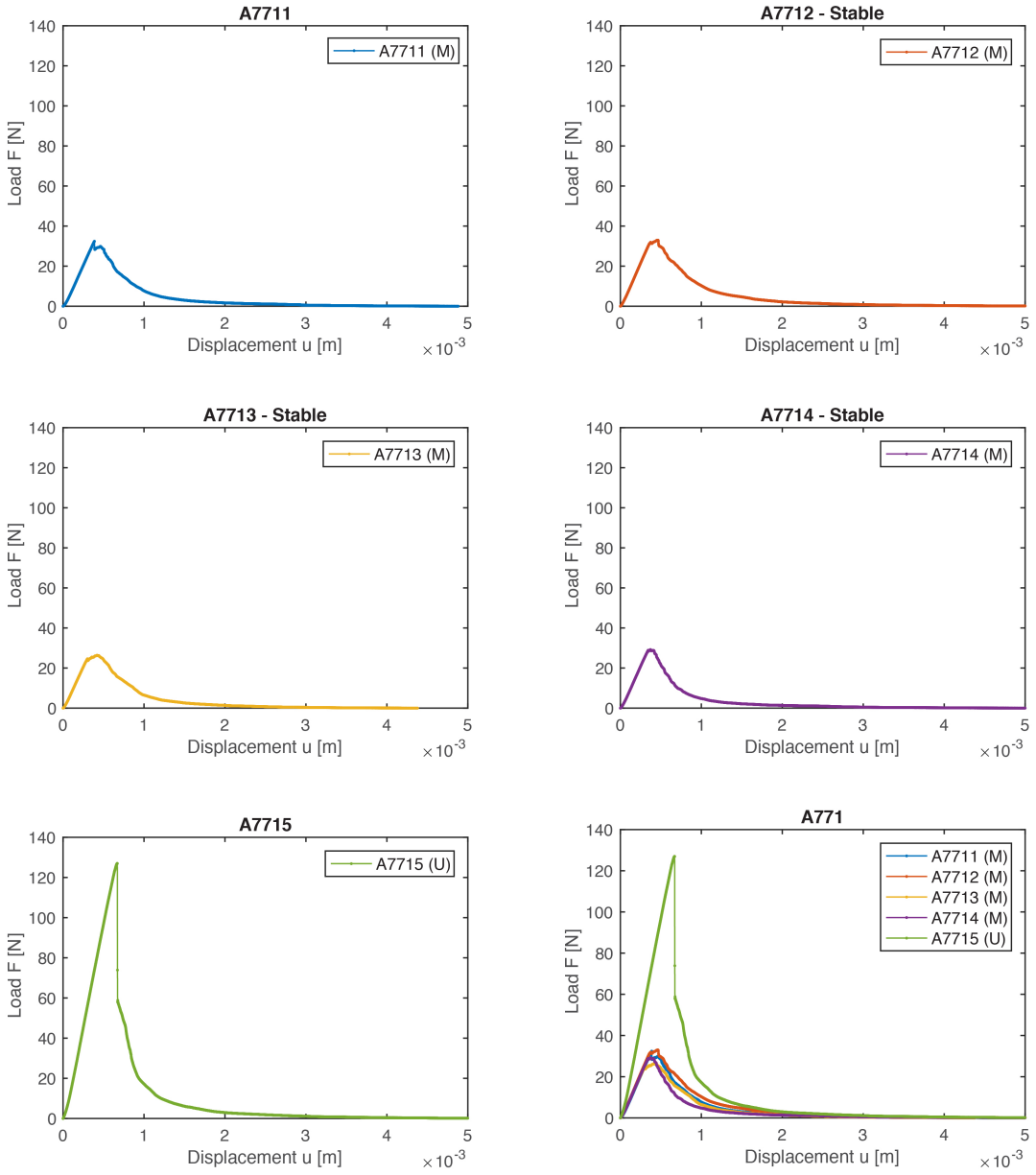

Figure B.7: Load-displacement curves of acetylated test specimens A7711-R7715 from plank 77.

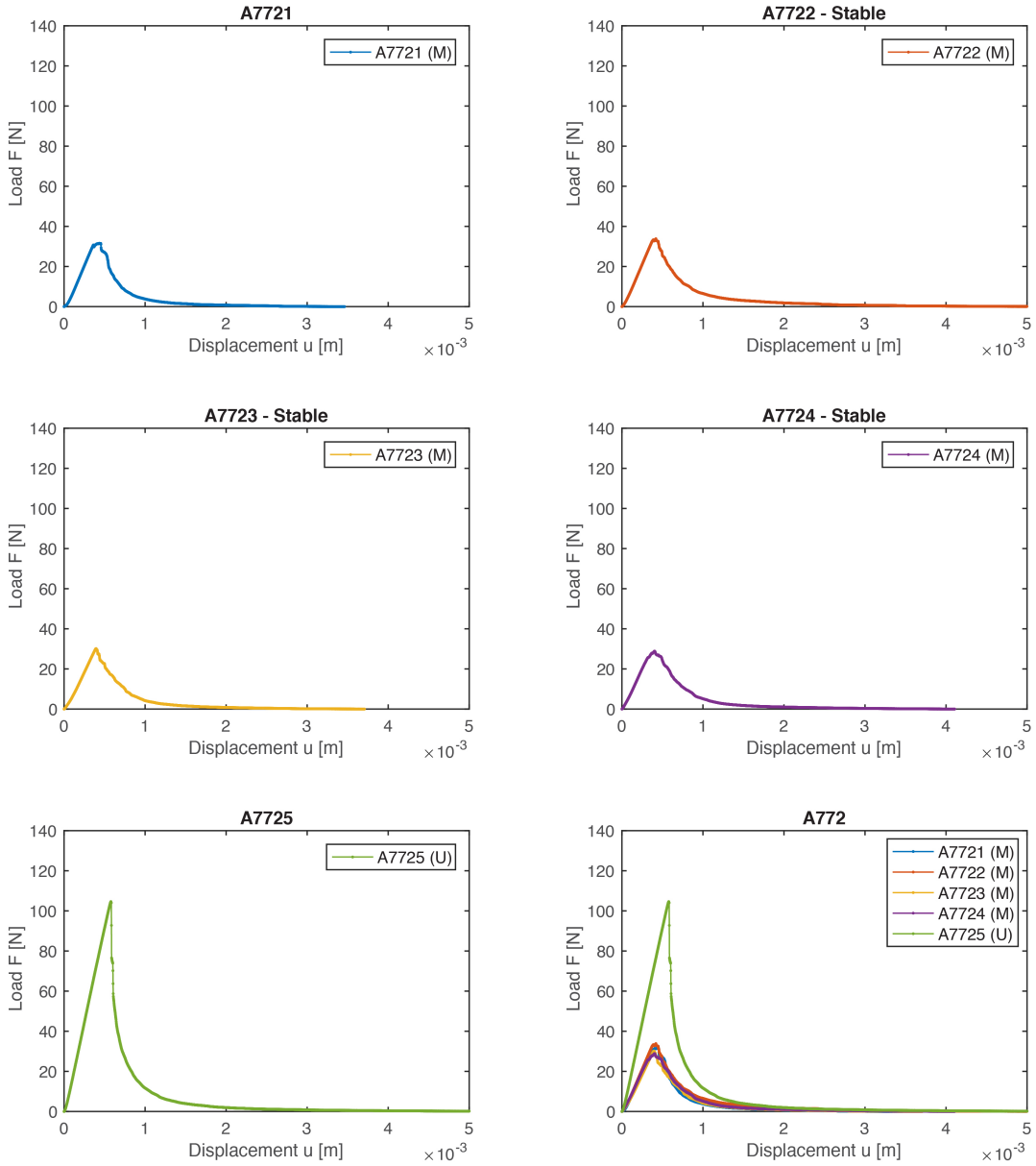

Figure B.8: Load-displacement curves of acetylated test specimens A7721-R7725 from plank 77.